UNIVERSITY OF CALIFORNIA
RIVERSIDE

Explore Spin Dependent Phenomenon in Topological Insulator and Magnetic Insulator

A Dissertation submitted in partial satisfaction
of the requirements for the degree of

Doctor of Philosophy

in

Physics

by

Zilong Jiang

December 2015

Dissertation Committee:
Dr. Jing Shi, Chairperson
Dr. Ward Beyermann
Dr. Jeanie Lau

The Dissertation of Zilong Jiang is approved:

_____

_____

_____

Committee Chairperson

University of California, Riverside

Acknowledgment

Accomplishment of Ph.D. study is the most meaningful and proud moment for me. The life at University of California, Riverside endows me so much memory, capability, painful experience, happy time, active mind and strong work ethics, which will add significant value to my future. Writing this dissertation is not only an essential requirement for pursuing a Ph.D. degree, also a very good chance to take a look back at what I have achieved and who I should appreciate in the past five years.

First and foremost I want to make a sincere acknowledgment to my supervisor, Prof. Jing Shi who gives me extensive research opportunities and professional academic advices. I joined the Shi's group since the second year of Ph.D. study. Dr. Shi helps me build up a long term research proposal focusing on the emergent material topological insulator and related heterostructures. Dr.Shi encourages me to have the aggressive attitude towards the research work with great passion. He teaches me the scientific thinking and working mode and enjoys discussing about insightful ideas and challenging problems with me. With his support and delicate supervision, I also set up a successful collaboration with people inside and outside campus. I can not imagine that my Ph.D. work could be done without his teaching, support and encouragement. Thank you very much for mentoring me.

I'm also very grateful to Prof. Jeanie Lau and Prof. Ward Beyermann, who are my committee members and also give significant help for my research work. I would like to thank you to allow me to use the PPMS and Oxford fridge for transport measurements. I

want to express my appreciation to Prof. Vivek Aji for useful discussion and suggestion on magnetic topological insulator theory.

At this moment, I would like to acknowledge my colleagues in the lab for their assistance in research and dear friends in UCR for the friendship and life happiness. They are Peng Wei, Deqi Wang, Xinfei Liu, Tao Lin, Ray Sachs, Zhiyong Wang, Hamad Alyahyaei, Chi Tang, Yadong Xu, Zhisheng Lin, Mohammed Aldosary, Bowen Yang, Junxue Li, Victor Ortiz, Yawen Liu, Mark Lohmann, Benjamin Madon, Dong Gui, Lei Guo, Wei Han, Hang Zhang, Xiaoxiao He, Fenglin Wang, Bin Cheng, Peng Wang, Qian Cai, Tengfei Miao, Hua Wen, Cheng Pan, Yong Wu, Jun Xu, Jenru Chen, Ying Wang, Siyu Zhou, Xu Xu, Yanmeng Shi, Yi Wu, Shi Che, Shaolong Chen, Jian Huang, Lingli Wang, Zhongguang Xu and so many people who I can not list here. I enjoy the moment together with you and wish our friendship forever.

I also want to thanks my collaborators from different universities who contribute a lot to my academic work and share their brilliant ideas with me. They are Cuizu Chang, Ferhat Katmis, Peng Wei, Jagadeesh.S. Moodera from Francis Bitter Magnetic Lab at MIT, Massoud Ramezani Masir, Allan H. MacDonald from UT Austin, Jianguo Zheng, Dexter Humphrey from UC Irvine, Bo Zhou, Yulin Chen, Biao Lian from Stanford, Yabin Fan, Murong Lang from UCLA, and Dong Yan, Nissim Amos from UCR.

Last but not least, I want to express my deep love and gratitude to my parents and Ms. Renjing Zheng for their support, trust, encouraging, genuine love, criticism and especially the challenge and life choice we pass through together. Although you stay

behind my academic study in the Ph.D. period, you are really the most precious and valuable present that I have in my life. Also please accept my best wishes to Renjing's success in the accomplishment of Ph.D. degree during the following year and I can not wait for building up our small family in the near future.

ABSTRACT OF THE DISSERTATION

Explore Spin Dependent Phenomenon in Topological Insulator and Magnetic Insulator

by

Zilong Jiang

Doctor of Philosophy, Graduate Program in Physics
University of California, Riverside, December 2015
Dr. Jing Shi, Chairperson

The dissertation summarizes my work in past four years on the study of topological insulators and magnetic insulators, especially in the field of electronic and spin transport properties. There are mainly three parts in this dissertation. The first part is about our research on topological insulator compounds $Bi_{2-x}Sb_xTe_{3-y}Se_y$ (BSTS). In our research, the successful growth and synthesis of BSTS single crystal is achieved. The bulk thin film resistance exhibits an insulating temperature dependence with a high resistivity up to 5 Ω·cm in the low temperature limit. A cusp-like low field magneto-resistance is observed in both bulk samples and nano devices which is an indication of strong spin-orbit coupling. To further suppress the trivial bulk conductance, we develop an e-beam irradiation approach to localize bulk states by introducing disorder. The experiment results show that the bulk conduction can be effectively reduced by a factor of 3 with introducing disorder and the transport of topological insulator devices can be modified.

The second part of this dissertation is focused on the interface magnetism study of topological insulator and magnetic insulator yttrium iron garnet ($Y_3Fe_5O_{12}$, YIG). We

carefully optimize the conditions and obtain the layer-by-layer growth mode of single crystal YIG films. By growing topological insulator on a magnetic insulator YIG, we find that the topological insulator surface in contact with YIG becomes ferromagnetic via magnetic proximity effect which is revealed by anomalous Hall effect and anisotropic magneto-resistance. The Curie temperature of magnetized surface ranges from 20 K to 300 K (room temperature) and is uncorrelated with the doping level in the topological insulator. In contrast, as the Fermi level is tuned by doping or electrostatic gating, both the longitudinal and anomalous Hall resistances can be varied accordingly. In this heterostructure approach, we successfully decouple the electrical properties from ferromagnetism in topological insulator, so that each can be tuned independently. This discovery will shed light on the realization of quantum anomalous Hall effect at higher temperature.

The third part is a spin Seebeck effect study on the topological insulator-magnetic insulator heterostructure. We design and fabricate a well-aligned current heating device for thermoelectric and magneto-thermoelectric study. Under a vertical temperature gradient, magnons in the magnetic insulator diffuse and carry a pure spin current which continues in the topological insulator layer via magnon-electron scattering at the interface. We observe a greatly enhanced spin Seebeck signal as the Fermi level is tuned near the Dirac point. Such a phenomenon indicates that the unique surface band structure of topological insulator is responsible for the highly efficient spin-charge conversion.

Contents

Table of Figures

Chapter 1 Introduction to Topological Insulators and the Relevance to Spintronics Research

An important theme in the condensed matter physics is the discovery and classification of novel phase of matter and materials. The researches on novel materials or structures not only deeply affect people's understanding of basic science, also drive the progress of wide technological applications, such as microelectronic system, low power memory and logic devices, quantum computation and information storage.

In recent years, the two dimensional layered structural materials (such as topological insulators[1,2], graphene[3,4], and transition metal dichalcogenides[5,6]) attract a great deal of attention and interest in both theoretical and experimental research owing to their unique band structure and properties. In this dissertation, I mainly discuss my work on topological insulators, especially their electrical and spin transport properties.

Chapter 1 consists of three parts: 1.1, introduction to topological insulators history, electronic band structure and material family; 1.2, introduction for anomalous Hall effect and quantum anomalous Hall effect in magnetic topological insulators by transition metal doping or magnetic proximity effect; 1.3, the spintronics study in topological insulators.

1.1 Topological Insulators

When the spin-orbit coupling is strong enough to invert the conduction and valence bands in the material, it creates a new state of matter, known as the time-reversal-invariant Z_2 topological insulators[7-9]. Ever since Z_2 topological order was proposed in 2005, enormous efforts have been dedicated to the observation, optimization and utilization of the time-reversal-symmetry protected topological non-trivial surface states.

According to dimensionality, topological insulators can be categorized as two-dimensional topological insulators (2D TIs) and three-dimensional topological insulators (3D TIs). A 2D TI is topologically characterized by a single Z_2 number and have the quantum spin Hall (QSH) state[10,11] in which a pair of spin-polarized edge states counter-propagates at each edge. As shown in Fig.1.1 (a), forward and backward moving channels for both spin up and spin down electrons give rise to four channels respectively. At each edge (top or bottom), the channel with opposite current flow consists of electrons with opposite spin directions and electron spin is directly locked to its momentum, thus maintains the time reversal (TR) symmetry. A system with such edge states is called in a QSH state, because it has a net transport of spin forward along the top edge and backward along the bottom edge, just like separated transport of electrons in the quantum Hall (QH) state which is demonstrated in Fig.1.1 (b). Although QSH state shares some similarities with QH state, it differs in important ways. The QH state requires an external large magnetic field which breaks the TR symmetry. Such a prerequisite is not easy to be achieved in microelectronic applications. In contrast, the QSH state exists in a TR invariant form and does not require an external magnetic field. The QSHE was theoretically proposed by Charles Kane & Eugene Mele and Andrei Bernevig & Shoucheng Zhang independently in 2005 and 2006. Later it was experimentally realized in HgTe/CdTe[12] and InAs/GaSb//AlSb[13] quantum wells, which are now recognized as 2D TIs.

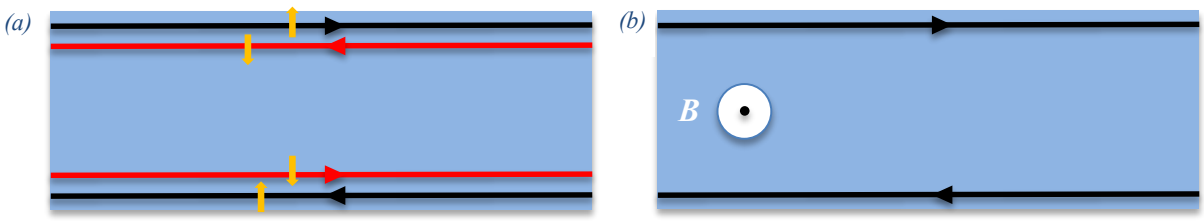

Fig. 1.1 (a) The helical edge states in QSHE. The upper (lower) edge has a forward moving channel with up (down) spin and a backward moving channel with down (up) spin. There is no magnetic field required. The time reversal symmetry is protected. (b) The chiral edge state in QHE. It has an external magnetic field and broken time reversal symmetry.

If the electron spin is scattered by a non-magnetic impurity, there will be two time reversal symmetry paths for scattering[14]. As shown in Fig. 1.2, a forward moving electron with up spin can make either a clockwise or counter clockwise scattering around the non-magnetic impurity. The possibility of each path is equal. The two paths differ by a phase difference of 2π, therefore two backscattering paths related by TR always interfere destructively and lead to a restriction of backscattering. As a result, the edge state of a topological insulator is immune to non-magnetic impurity and has strong prospect for applications (perfect transmission). However, for magnetic impurity, the time reversal symmetry is broken. The two scattering paths do not cancel each other. In a word, the robust QSH state is protected by time reversal symmetry[15,16].

Besides 2D topological insulator HgTe/CdTe and InAs/GaSb//AlSb quantum wells, 3D topological insulator materials are also predicted to exist. The alloy $Bi_{1-x}Sb_x$ was first proposed[8] as a 3D topological insulator at a special range of x and was confirmed by angle-resolved photoemission spectroscopy (ARPES) to host the topological surface states in the

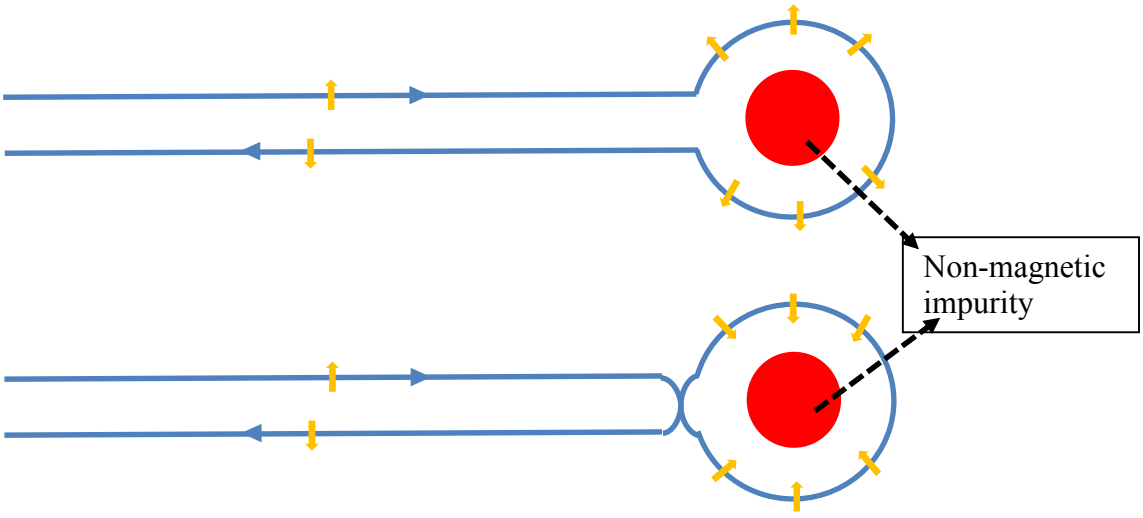

Fig.1.2 There are two paths for non-magnetic impurity scattering in a QSH edge state. The yellow arrows denote the spin direction and red solid circles stand for non-magnetic impurity scattering center.

System[1,2,17]. However, the band gap is very small and surface states turn out to be extremely complicated, making it difficult to be characterized in a transport geometry. Later in 2009, similar versions of 3D topological insulators were theoretically proposed in Bi_2Te_3, Bi_2Se_3 and Sb_2Te_3 compounds with a large bulk band gap and a gapless surface state consisting of single Dirac cone[18]. ARPES experiments confirmed the linear dispersion relations of surface states[19]. The single Dirac cone has one Kramer's pair, which is protected by time reversal symmetry and crucial for robustness of surface states. Fig. 1.3 demonstrates the calculated band structure of 3D topological insulators Bi_2Te_3, Bi_2Se_3, Sb_2Te_3 and Sb_2Se_3 from Zhang's work[18]. It clearly shows that three of them (Bi_2Te_3, Bi_2Se_3 and Sb_2Te_3) with layered structure maintaining robust surface states are 3D topological insulators, whereas another material Sb_2Se_3 is not.

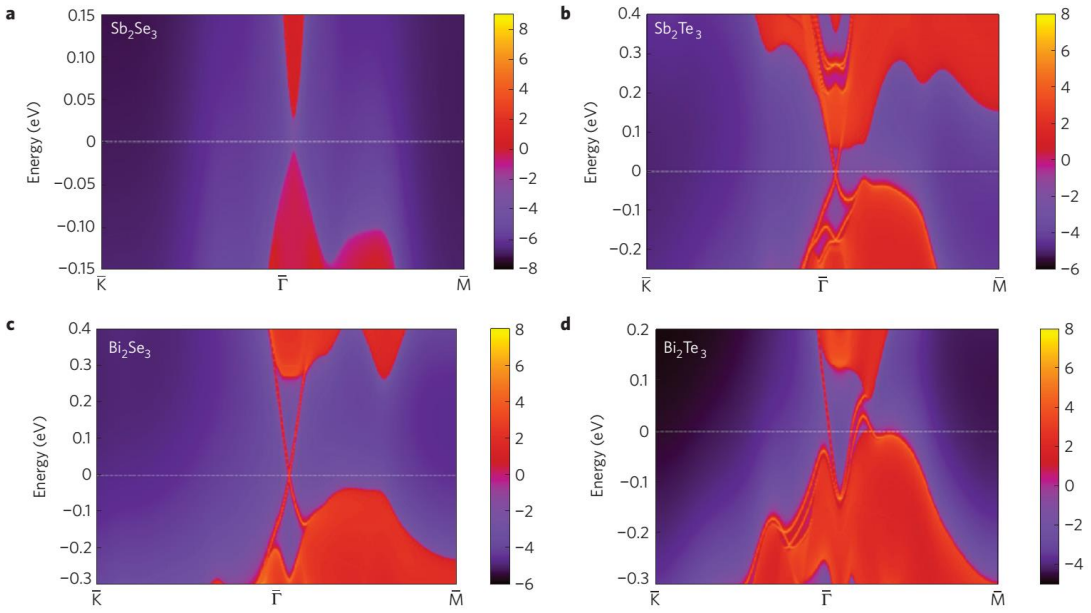

Fig.1.3 The calculated bulk and surface band structure of Sb_2Se_3 (a), Sb_2Te_3 (b), Bi_2Se_3 (c) and Bi_2Te_3 (d). The red region denotes bulk energy bands and the blue region denotes bulk band gap. The two crossed red lines indicate the surface states existing in Sb_2Te_3, Bi_2Se_3 and Bi_2Te_3, which are situated inside the gap of bulk energy band. No surface states exist for Sb_2Se_3. Adapted from Zhang, et al. Nat. Phys. ***5****, 438-442.*

Materials Challenge by far, the Bi_2Se_3 family TIs are the most popular and widely used TI materials due to stoichiometric chemical composition, relatively large bulk band gap (~0.3 eV for Bi_2Se_3) and simple surface Dirac cone structure. However, the as-grown Bi_2Se_3 is always n type with a lot of defects owing to a large number of Se vacancies. An isostructural material Bi_2Te_3 is also highly metallic, due to antisite defects between Bi and Te. Significantly efforts have been made to achieve bulk insulating behavior in topological insulator materials. One effective approach is doping holes to compensate for the residual electrons[20-24]. This was done by low-level substitution of Ca^{2+}, Sb^{2+} or Cd^{2+} for Bi^{3+}. With this defect-engineering strategy, people can optimize the transport properties of topological insulator Bi_2Se_3 to show a high bulk resistivity and successfully observe the n- to p- type crossover. Another approach is introducing the new topological insulator materials, for

example, the ternary compound Bi_2Te_2Se[25,26] and quaternary compound $(Bi_xSb_{1-x})_2(Te_ySe_{1-y})_3$[27-29] or the $(Bi_xSb_{1-x})_2Te_3$[30,31]. In these compounds, the bulk resistivity usually exceeds 1 Ω·cm, together with a variable range hopping (VRH) behavior which is a hallmark of an insulator, while for most undoped TI such as Bi_2Se_3, the typical resistivity is around 50 mΩ·cm. For $(Bi_xSb_{1-x})_2Te_3$ and $(Bi_xSb_{1-x})_2(Te_ySe_{1-y})_3$ compounds, the Fermi level can also been tuned by corresponding doping fraction x or y and leads to a sign change of Dirac carriers. The discussion of $(Bi_xSb_{1-x})_2(Te_ySe_{1-y})_3$ growth and electrical properties will be the main concern in the first part of this dissertation.

In addition to traditional 3D TIs family, novel topological insulators with disorder or crystal symmetry have also been proposed and experimentally realized, such as topological Anderson insulator[32], topological crystalline insulator[33] and topological Kondo insulator[34]. One special kind of topological Anderson insulator is obtained by introducing impurities in a two (three) dimensional metal; here disorder not only causes metal-insulator transition, as anticipated, but is also fundamentally responsible for creating extended edge (surface) states[35,36]. We develop a creative electron-beam irradiation method to introduce disorder into 3D topological insulator and modify the transport property of topological insulator nano-device according to different dose levels. We will discuss about more details in the first part.

1.2 Magnetic Topological Insulator and Quantum Anomalous Hall Effect

The well known Hall effect was discovered by Mr. Hall in 1879, indicating the voltage drops across the transverse direction of applied current in an electrical conductor at a perpendicular magnetic field as shown in Fig. 1.4. In a non-magnetic material, the Hall

voltage is proportional to the external magnetic field since it results from the deflection of charge carriers by the Lorentz force. The slope of linear field dependence of Hall voltage is determined by the carrier type and density of specific charge carriers. This so-called ordinary Hall effect (OHE) serves as a probe for the important electrical properties of semiconductor materials, which has been widely used in scientific research and industry areas.

When similar experiments were performed on ferromagnetic materials, the magnetic-field-dependent Hall voltage showed an unusually large Hall effect originated from the magnetization of ferromagnetic conductors, which was called the anomalous Hall effect (AHE)[37] as depicted in Fig.1.4. Since a ferromagnetic material keeps its spontaneous magnetization when the external magnetic field is removed (also known as Remanence), the AHE can be measured at zero magnetic field.

Although it is generally believed that the spin-orbit coupling (SOC) plays a fundamental role in the AHE, its exact mechanism is a subject of research and under debate for several decades. There are several groups of mechanism for AHE's origin. One group of AHE mechanism is ascribed to impurity induced skew scattering or side jump of carriers which are referred to as extrinsic mechanism. The other group of AHE is believed to result from the property of the electronic band structures of ferromagnetic conductors, which is regarded as the intrinsic mechanism. The AHE has been observed in ferromagnetic conductors, ferromagnetic semiconductors and also a heterostructure consisting of a non-magnetic material and magnetic insulator by magnetic proximity effect.

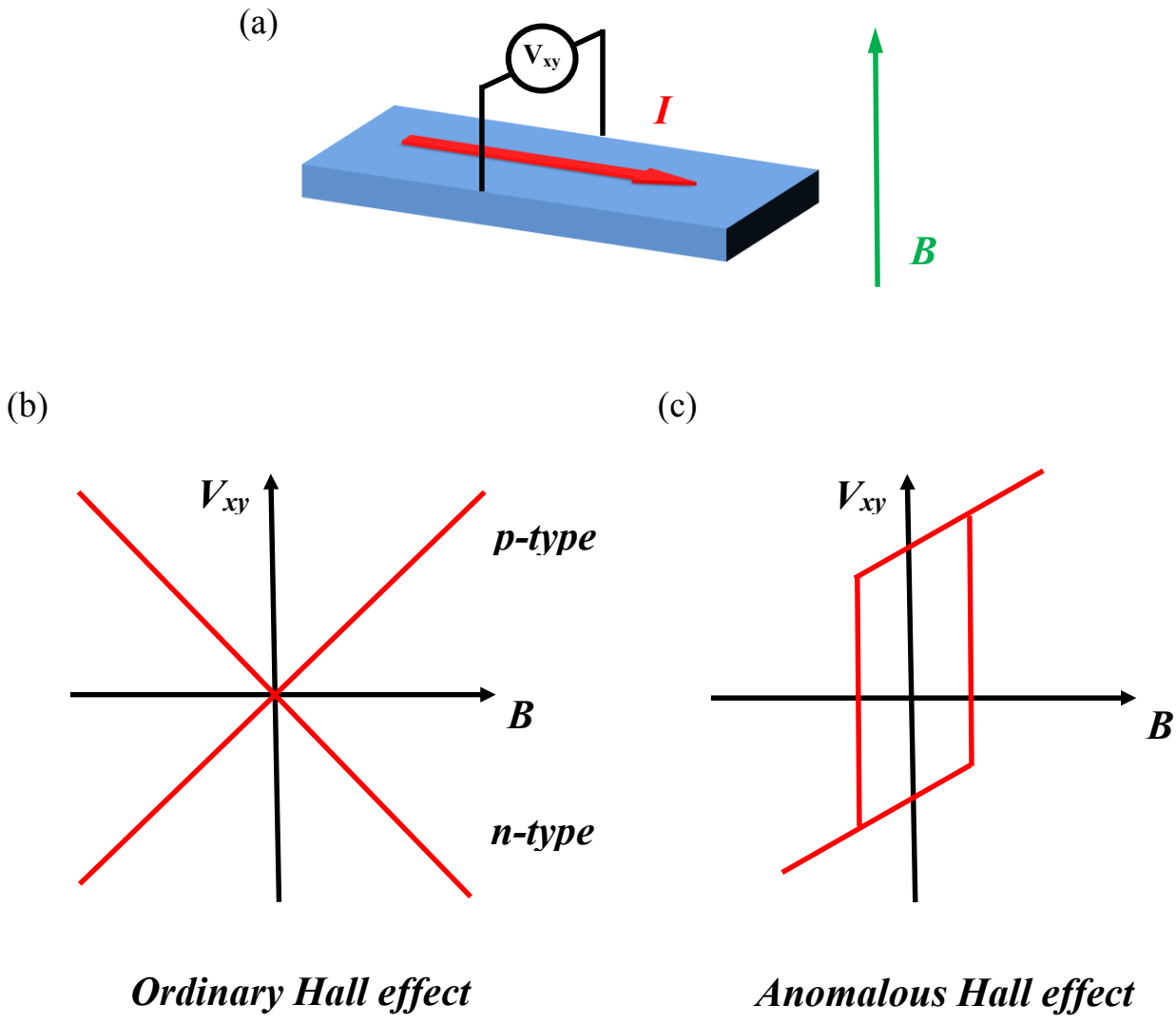

Fig.1.4 Schematics illustration of ordinary Hall effect (n-type and p-type carriers) and anomalous Hall effect.

The AHE in heterostructure by magnetic proximity effect is the main focus of the second part in this dissertation. We will discuss more details later.

Given the experimental discovery of the quantum Hall and the quantum spin Hall effects (discussed in Chapter 1.1), it is natural to ask whether the AHE could be quantized. The crucial criteria for realizing a quantum anomalous Hall (QAH) state are (1) a

ferromagnetic 2D insulator which breaks time-reversal symmetry and (2) a band inversion transition with strong SOC[38,39]. The theoretical work has shown that breaking the TRS of a topological insulator thin film with ferromagnetism via transition metal doping[40] or magnetic proximity effect[41] will lead to the QAHE. In a 2D TI, if ferromagnetically induced exchange splitting of the lowest order quantum well subbands is large enough, so that one set of spin subbands are driven back to the topologically trivial phase, there will be only one spin channel at each edge remaining topologically protected, and thus the helical edge states responsible for the QSHE will evolve into chiral edge states exhibiting QAHE. Such a theoretical model[42] is proposed for magnetically doped HgMnTe as a candidate of the QAH insulator. However, because the Mn moments do not order spontaneously in HgMnTe, an additional Zeeman field is required.

Let's switch to the 3D TI case. In a 3D TI, ferromagnetism opens a gap in the Dirac surface band of the surface perpendicular to the magnetization vector and changes it into a QH system. Chiral edge states appear at each magnetic domain wall which is also the boundary between two topologically different phases. In a uniformly perpendicular magnetized 3D TI film, the gapped surface bands at the top and bottom surfaces have different topological characters due to the opposite normal directions. The chiral edge states reside at the sample edge which acts as the topological boundary between the top and bottom gapped surface bands. The QAHE can thus be measured with electrodes at the sample edge.

When the thickness of a 3D TI is reduced to several nanometers, the hybridization between the Dirac surface states of the top and bottom surfaces induces gap-opening, which

pushes the system into a 2D TI or a 2D topologically trivial insulator phase. In both cases, the QAHE can be observed as long as the hybridization gap is smaller than the ferromagnetic exchange energy, because exchange splitting can always lead to the situation that one set of spin subbands is topologically non-trivial whereas the other is topologically trivial. This effective four-band model is shown in Fig.1.5 and proposed by researchers from Chinese Academy of Sciences and Stanford University to explain the mechanism for QAHE in magnetic TIs[40].

As illustrated in Fig. 1.5 (A) , if the four –band system is in the topologically trivial phase, the exchange field will induce a band inversion in the upper block and push the two subbands in the lower block even farther ways from each other. Thus, the 2D model with a negative mass in the upper block contributes e^2/h for the Hall conductance. On the other hand, for case (B), if the system is in topologically nontrivial phase, both blocks have inverted band structures. In such case, a sufficiently large exchange field can increase the band inversion in upper block and release it in the lower block. The negative mass in the upper block contributes e^2/h for the Hall conductance. Such a mechanism is general for the thin film TI systems with FM ordering.

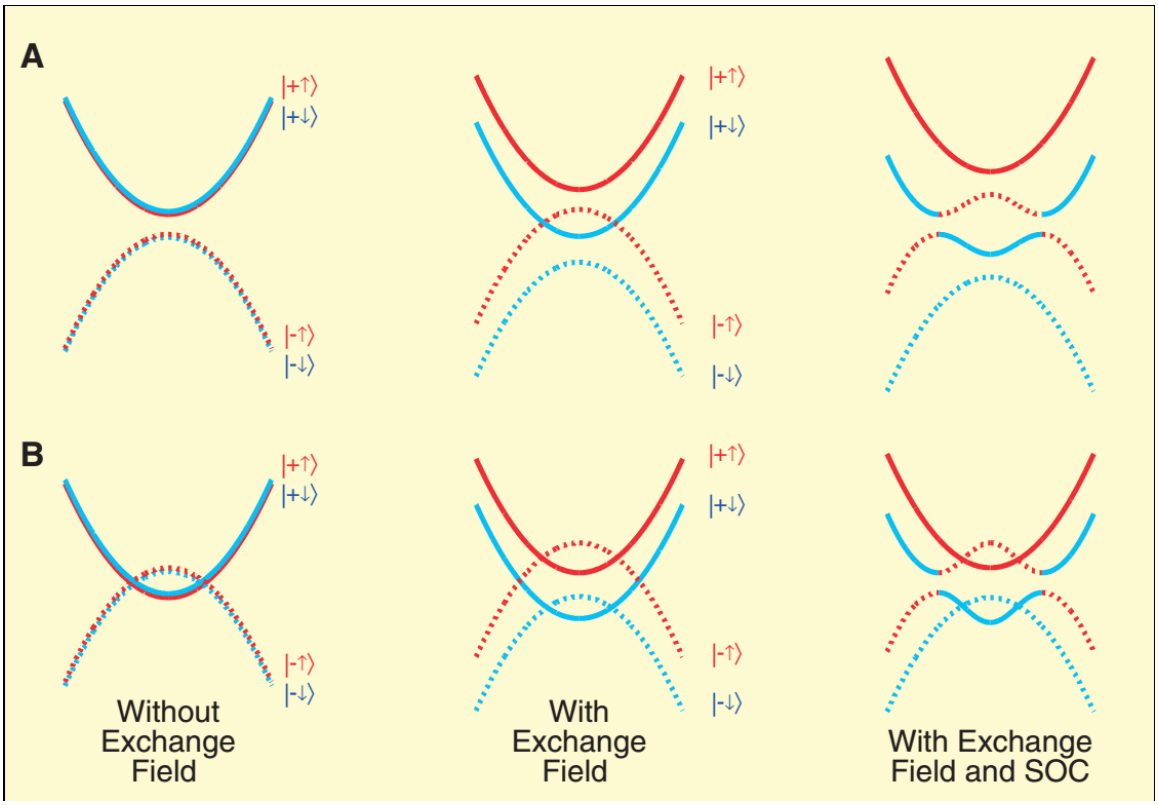

Fig.1.5 Evolution of subbands structure when increasing the exchange field and existence of spin-orbit coupling (SOC). The solid lines and dashed lines are two pairs of subbands respectively. The blue color denotes spin down electrons; red, spin up electrons. (A) The initial subbands are not inverted. (B) The initial subbands are already inverted. Adapted from Yu, R. et al. Science ***329****, 61-64 (2010).*

Doping TI with magnetic impurities is a convenient approach to bring ferromagnetism into a topological insulator. There are several challenges in material preparation to obtain a magnetically doped TI exhibiting the QAHE. First, the magnetically doped TI should have a long range ferromagnetic order that can hold even in an insulating regime; the easy magnetization axis should be perpendicular to the film plane. Second, the ferromagnetic TI film should have uniform and well-controlled thickness; to localize the dissipative conduction electrons, the film should be as thin as possible, but should be thick enough to keep hybridization gap larger than the ferromagnetic exchange energy. Third,

the Fermi level should be able to be finely tuned into the gap of the magnetically doped TI thin film. The QAHE was first realized in Cr-doped $(Bi_xSb_{1-x})_2Te_3$ thin films by Xue's group in Tsinghua University[43] and later was confirmed by two other groups independently[44,45].

Although transition metal doping in TI is a convenient and very common method to introduce ferromagnetism order, it is hard to separate the surface and the bulk phases. Moreover, the doping of magnetic elements inevitably introduces point defects, magnetic scattering centers and impurity states in the insulating gap, which are detrimental to mobility and transport of spin-momentum locked surface electrons in TIs. Therefore, it is natural and essential to propose TI/MI heterostructure to create cleaner ferromagnetic TI systems without structurally disturbing the TI. In such a heterostructure as shown in Fig. 1.6, the short-range nature of magnetic proximity coupling with a magnetic insulator allows the TI surface states to experience the exchange interaction, where the symmetry breaking happens right at the interface, rather than affecting the majority bulk states or introducing defects. Besides, the proximity induced symmetry breaking approach possibly creates a larger surface exchange gap than transition metal doping method, since we can choose to couple the TI with a high T_C magnetic insulator. Such interface symmetry breaking can be local and therefore can be used to nanopattern various TI heterostructures with broken time-reversal symmetry in designated regions.

In the chapter 3, we will present our result based on TI-YIG and EuS-TI-YIG heterostructure. The proximity induced ferromagnetism is revealed by both anomalous

Hall effect and anisotropy magneto-resistance. This system could serve as a clean and tunable platform to realize the QAHE in higher temperature.

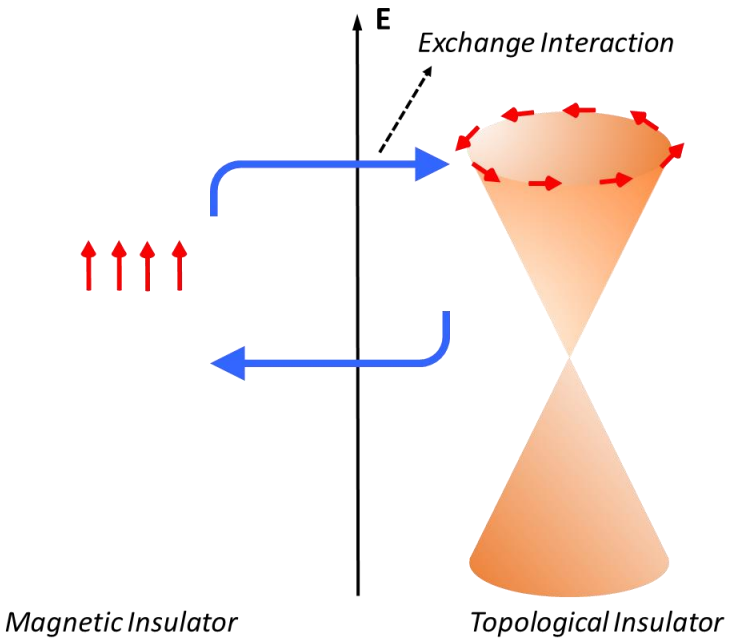

Fig.1.6 Schematic illustration of the ferromagnetic interaction between topological insulator and magnetic insulator.

1.3 Topological Insulator for Spintronics

Topological insulators form a new quantum phase of matter which is clearly distinct from the classic dichotomy of metals and semi-conductors. Whereas the bulk states form a bandgap, the surface states form a Dirac cone similar to graphene electronic structure and are topologically protected against disorder scattering. In marked contrast with the spin-degenerate bands of graphene, TI surface states are spin polarized. This metallic surface states are populated by massless Dirac fermions with spin-momentum locking, where the carrier spin lies in-plane, locked at right angles to the carrier

momentum[15,16]. Topological insulators are expected to produce new functionalities and enable insights into complex phenomena in many interesting areas such as spintronics, quantum information technology, highly correlated electron systems, magnetic monopoles and quantized magneto-electric coupling.

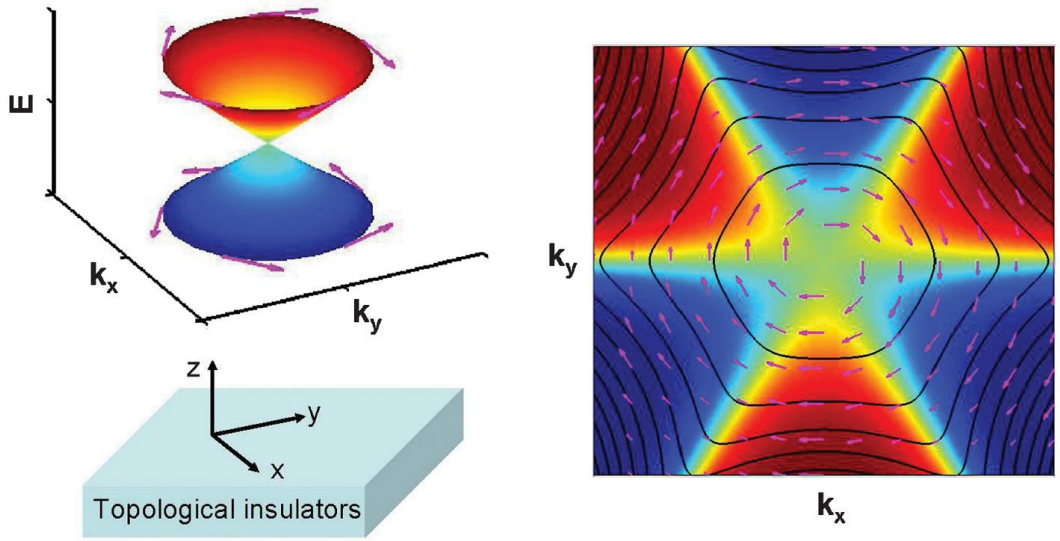

Fig. 1.7 Schematic illustration of topological surface states spin-momentum locking. See description in the main text. Adapted from ref 46.

Fig. 1.7 describes the spin polarization of surface states on the top surface. The z direction (Fig. 1.7, left panel) is the surface normal, pointing outward. The right panel is a top view of the surface state spin texture, with the arrows representing the x-y planar spin polarization and the color indicates the z component of the spin polarization. In the Bi_2Se_3 family of materials, the upper Dirac cone has a left-handed helicity when looking from above the surface. And the observed chirality inversion of the surface spin texture indicates a 180 ° turnaround of the spin momentum locking profile in moving chemical potential

across the Dirac node. Above the Dirac node, a quasi-particle moving in the +x direction is locked with –y spin polarization state, whereas below the node, the +x moving quasi-particle state is locked to +y spin. Therefore, these spin polarization states locked to specific momentum states open up many new possibilities for electrical manipulation of spin in a topological device. For example, by electrical gating or band structure engineering of both top and bottom surfaces of topological insulator thin film, one can achieve the direct observation of the consequences of chirality inversion, i.e. the transition between the left-handed chirality (LHC) electron-like Fermi surface and the right handed chirality (RHC) hole-like Fermi surface in topological insulator.

Theoretically, Raghu et al. pointed out[47] the helical spin texture described by the single Dirac cone equation leads to a general relation between charge current density **j(x)** and spin density **S(x)** on the surface of the topological insulator:

$$j(x) = \nu[\psi^{\dagger}(x)\sigma\psi(x) \times \hat{z}] = \nu S(x) \times \hat{z}$$

Such a simple relation leads many intrinsic correspondences between spin and charge dynamics in the topological system. However, not only in TI, the Rashba spin-splitting in 2D electron gas system also gives the same polarization, except that there is a cancellation between two spin directions. In Rashba, there are two spin-momentum locked circles: clockwise and counterclockwise. Rashba mechanism offers less efficient spin-charge conversion than spin-momentum locking and usually dominates near the conduction/valence band region.

This remarkable property of spin-momentum locking in topological surface states are not only anticipated by theory, but also inspires interest in spin-resolved photoemission,

polarized optical spectroscopic techniques and transport experiment. An unpolarized charge current flowing on the topological surface should create a net spin polarization, the amplitude and orientation of which are controlled by the charge current. C.H. Li et al. from Naval Lab first reported[48] direct electrical detection of the bias current-induced spin polarization as a voltage measured on the transport geometry consisting of topological insulator thin film and ferromagnetic metal tunnel barrier surface contacts.

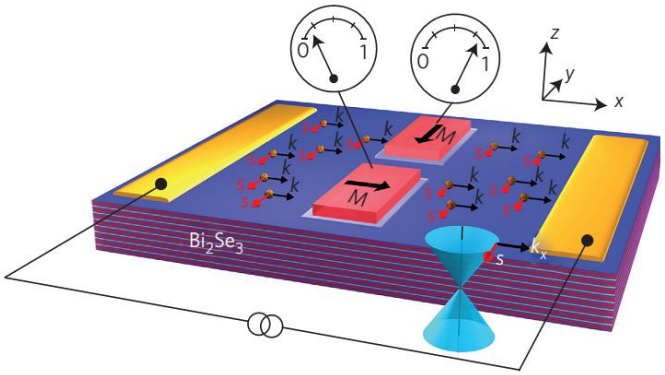

Fig. 1.8 Concept drawing of transport experiment on TI spin valve device.

In their experiment (Fig. 1.8), the magnetization of the contact determines the spin detection axis and the voltage measured at this contact is proportional to the projection of the TI spin polarization onto this axis. The dependency on experimental parameters can be most straightforwardly explained by spin momentum locking in surface states. When the charge current is orthogonal to the magnetization of ferromagnetic detector contact, the TI spin is parallel (or antiparallel) to the magnetization, as shown in Fig. 1.8, and a spin-related signal is detected at the ferromagnetic contact proportional to the magnitude of the charge current. When the direction of the charge current is reversed, the measured voltage changes

sign. On the other hand, when the contact magnetization is reversed by applying in-plane magnetic field, the measured spin voltage mirrors the hysteresis loop of the contact.

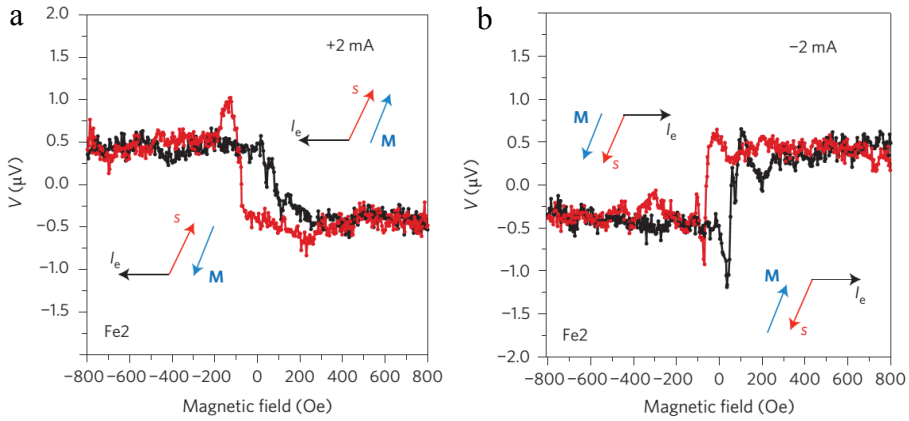

Fig. 1.9 TI spin polarization detected as a voltage with Fe/Al_2O_3 contacts. The Bi_2Se_3 film is 45 nm thick.

However, one critical problem in the experiment is that Bi_2Se_3 TI film has a high bulk carrier densities (over 10^{19} cm^{-3}) with Fermi level located in the bulk conduction band. The high bulk carrier densities will allow a parallel bulk conduction channel which strongly suppress the contribution of topological surface states. Therefore, engineering electronic band structure of TI will lead to significantly increase the spin voltage from spin polarization in surface states. Moreover, the deposition of ferromagnet (Fe, NiFe, CoFeB, etc.) is proven to cause the bend banding or defects absorption in topological surface states[49]. Given careful consideration, we design the spin Seebeck experiment on Topological insulator-magnetic insulator heterostructure to explore intrinsic spin-momentum locking property of topological surface states. The topological insulator material is $(Bi_2Sb_{1-x})_2Te_3$, the Fermi level of which can be tuned by varying Bi:Sb composition; the magnetic insulator material is YIG, which has a Curie temperature much higher than 300 K. This is the main topic in last part of the thesis.

Chapter 2 Electrical Transport Study of Topological Insulators

2.1 Growth, Synthesis and Device Measurements of Topological Insulator Compounds $Bi_{2-x}Sb_xTe_{3-y}Se_y$ (BSTS)

2.1.1 Bi_2Se_3, Bi_2Te_2Se and $Bi_{2-x}Sb_xTe_{3-y}Se_y$

Bi_2Se_3 is regarded as a model TI. It exhibits a single Dirac cone and largest bandgap (~0.3 eV) of known TIs, and its topological surface states have been shown to be robust at room temperature in various experimental observations.

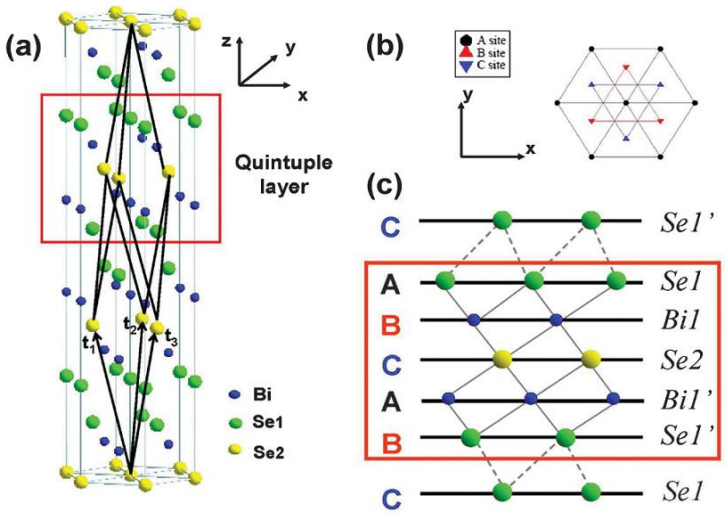

Fig. 2.1 Crystal structure of Bi_2Se_3. Adapted from ref 15.

The crystal structure of Bi_2Se_3 is shown in Fig. 2.1 and consists of a layered structure where individual layers form a hexagonal lattice. The material consists of five-atom layers stacked along the z direction, known as quintuple layers (QL). Each quintuple layer consists of five-atom layers per unit cell with two equivalent Se atom denoted by Se1 and Se1', two equivalent Bi atoms denoted by Bi1 and Bi1', and a third Se atom denoted by Se2 in Fig. 2.1 (c). The coupling between two atomic layers within a quintuple layer is

strong, while that between quintuple layers is much weaker and predominantly of the van der Waals type.

Although Bi_2Se_3 stands out as an excellent prototypical material among 3D topological insulators and its massless Dirac fermion surface states have been confirmed by surface-sensitive spectroscopic techniques, the distinct transport property of surface states can-not be clearly demonstrated due to the overwhelmingly high density of the bulk states that coexist with the surface states. At the exact stoichiometry, Bi_2Se_3 does not exhibit the expected insulating behavior due to excess charge carriers caused by selenium vacancies. By introducing p-type dopants such as calcium (Ca), it was shown by ARPES that the Fermi level could be moved to the bulk band gap. An insulating behavior was also observed in electrical resistivity measurements of Ca-doped Bi_2Se_3 bulk materials. Furthermore, by systematically varying the Ca-concentration, Wang et al. successfully tune the carrier density and the carrier type in high-quality Bi_2Se_3 single crystals[20] as shown in Fig. 2.2.

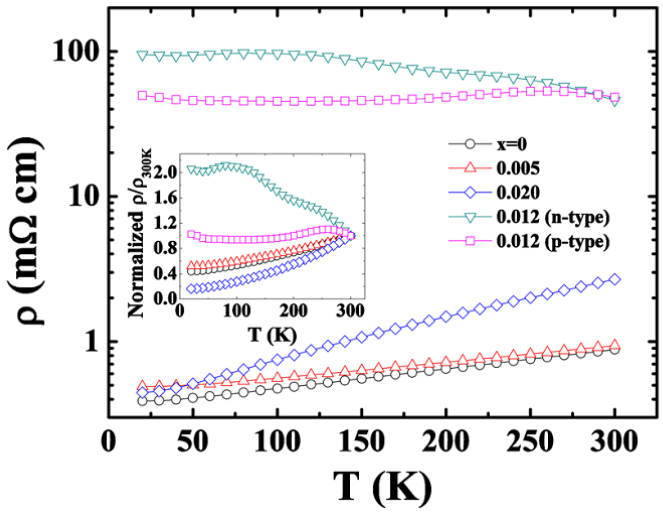

Fig. 2.2 Temperature dependent resistivity curve for both doped and undoped Bi_2Se_3 samples. One n-type x=0.012 samples shows the insulating behavior. Its resistivity is two orders of magnitude greater than that of the metallic samples. Adapted from ref 20.

Among the recently discovered TIs, Bi_2Se_3 has been most attractive and widely used in different experiments and theoretical calculations owing to its simple surface-state structure. Unfortunately, as discussed above, near-stoichiometric Bi_2Se_3 is always n-type material due to the large amount of Se vacancies. Another common TI material Bi_2Te_3 can be grown as n type, but usually it is also highly metallic with low bulk resistivity, most likely due to antisite defects which are promoted by close electronegativities of Bi and Te. Significant efforts have been made to achieve bulk insulating behavior in Bi_2Se_3 and Bi_2Te_3; however, the bulk remains to be essentially a metal with Fermi level across the bulk conduction (valence) band due to large carrier densities. A clear insulating temperature dependence in disordered semiconductors, such as the variable range hopping (VRH) behavior, is also missing in transport measurement data of Bi_2Se_3 and Bi_2Te_3.

Given this difficulty, searching for a TI material better suited for achieving the bulk insulating state is obviously important. Y. Ando group from Osaka University first reported[25] that TI material Bi_2Te_2Se, which has an ordered tetradymite structure (Fig. 2.3-a) with basic quintuple-layer unit of Te-Bi-Se-Bi-Te, has desirable characteristics for topological surface state dominated transport studies. They found that high quality single crystals of ordered Bi_2Te_2Se show a very large resistivity exceeding 1 Ω cm (Fig. 2.3-c) and insulating behavior as temperature is cooling from 300 K. The Arrhenius plot (Fig. 2.3-d) of longitudinal resistivity for Bi_2Te_2Se sample indicates an activated temperature dependence in the range from 300 K to 150 K with an excitation energy $\Delta \sim 23$ meV. Below 100 K, the transport result can be explained by an insulating bulk channel characterized by 3D VRH behavior and a metallic channel which saturates below 20 K.

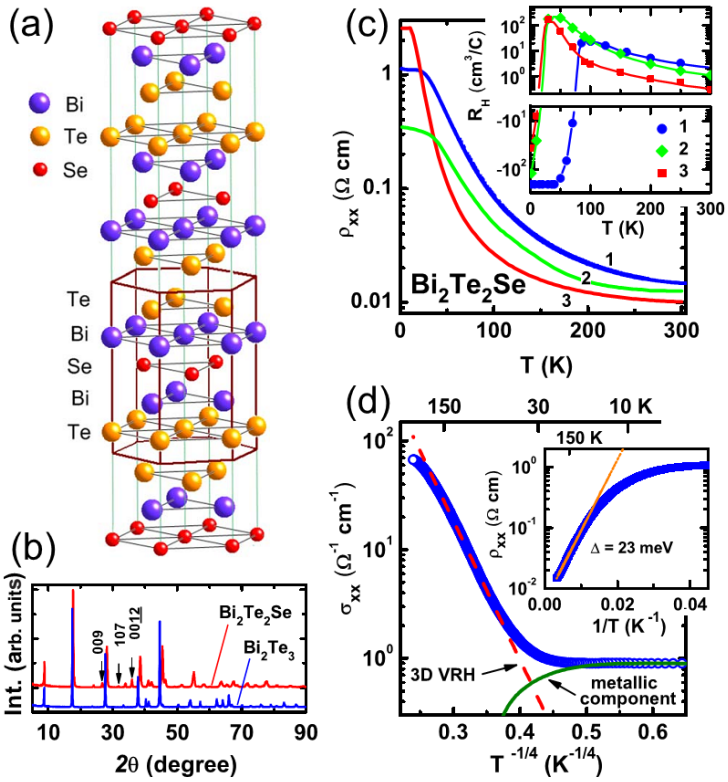

Fig. 2.3 Layered crystal structure and transport result of Bi_2Te_2Se sample. Adapted from ref 25.

The clarification of bulk and surface transport channels in Bi_2Te_2Se sample shows the possibility of achieving surface dominated transport result in low temperature, together with the high bulk resistivity larger than 1 Ω cm. Clearly, Bi_2Te_2Se is the better material than Bi_2Se_3 or Bi_2Te_3 (binary compounds) to investigate the surface quantum transport phenomenon in a topological insulator.

The high bulk resistivity of Bi_2Te_2Se is understood by its chemical characteristics suitable for reducing defect formations. In this regard, the tetradymite $Bi_{2-x}Sb_xTe_{3-y}Se_y$ (BSTS), which has the same crystal structure as Bi_2Te_2Se (can be regarded as a member of BSTS family with x=0 and y=1), is very interesting because a series of special combination of x and y have been known to yield a high resistivity.

Fig. 2.4 shows that simultaneously tuning of the Sb and Se contents in the BSTS crystals makes it possible to control the energy location of the Dirac cone in the bulk band gap and the sign of Dirac carriers, while keeping the bulk insulating property[29]. Four ARPES images correspond to different insulating compositions: (x,y)=(0,1), (0.25, 1.1), (0.5, 1.3) and (1,2). This kind of control of material properties is an advantage of BSTS system and makes the BSTS an interesting platform for investigating the Dirac electronic band structure. Note that the Dirac point is buried in the bulk valence band at x=0, which means the putative transport property near the Dirac point will be strongly affected by the bulk-surface interband scattering. As the x value increases, the Dirac point (surface states) will shift upwards to be isolated from the bulk accompanied by the decreasing of carrier density, creating a more ideal situation for topological insulator device applications. Another important aspect is the Fermi level position in BSTS samples is located above the Dirac point in $0 \leq x \leq 0.5$ and below it in x=1.0, which suggests that carrier type switches from electron to hole.

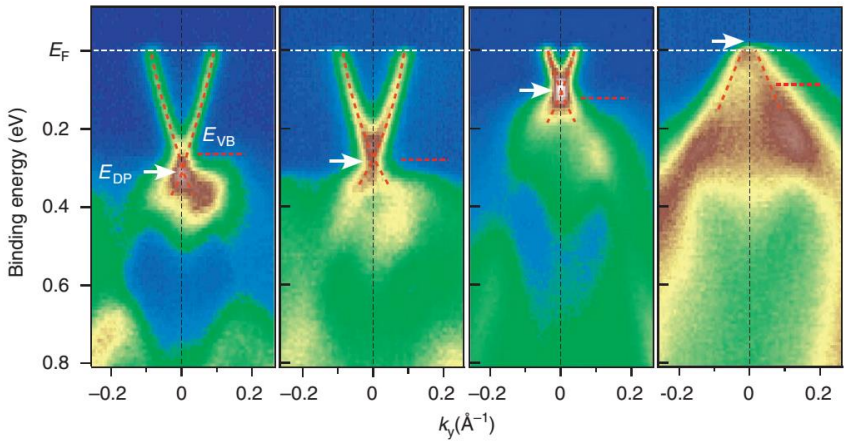

Fig. 2.4 ARPES image for BSTS samples in 4 different compositions: (left to right) (x,y)=(0,1), (0.25, 1.1), (0.5, 1.3) and (1,2). Adapted from ref 29.

The experimental realization of both Dirac holes and electrons in the BSTS system demonstrated here points to the high potential of this material for studying the various topological phenomenon requiring the access to the Dirac point. This family has much higher bulk resistivity at particular Bi and Te doping value. Therefore, by varying the Bi and Te composition during the growth procedure, we can easily achieve the surface dominated transport contribution. Furthermore, in the device with high bulk resistivity, utilization a dual gate configuration leads to the electric field control of the Fermi level position at Dirac band structure of topological insulator[50].

In the following part of this section, I will show the growth procedure of high quality BSTS TI crystals by furnace method. We fabricate the TI bulk device by exfoliation from single crystal pieces. We present the very large bulk resistivity of BSTS device measured in the Van der Pauw geometry. Finally, we also systematically study the localization effect on TI nano device via e-beam irradiation approach.

2.1.2 Single Crystal $Bi_{2-x}Sb_xTe_{3-y}Se_y$ Growth

Single crystals of $Bi_{2-x}Sb_xTe_{3-y}Se_y$ (BSTS) are grown by a multistep heating procedure in a programmable furnace. Stoichiometric amounts of high purity elements Bi (99.999%, Alfa Aesar), Sb (99.999%, Alfa Aesar), Te (99.999%, Alfa Aesar), Se (99.999%, Alfa Aesar) are sealed in evacuated quartz tubes by oxyhydrogen melting technique. The tube is then loaded into a programmable furnace (Fig. 2.5) and slowly heated up to 850 °C and kept for 4 days with intermittent shaking to ensure a homogeneity of the melt. In the following step, it is cooled slowly to 550 °C and annealing at that temperature for another 4 days. The sample is finally cooled down to room temperature very slowly.

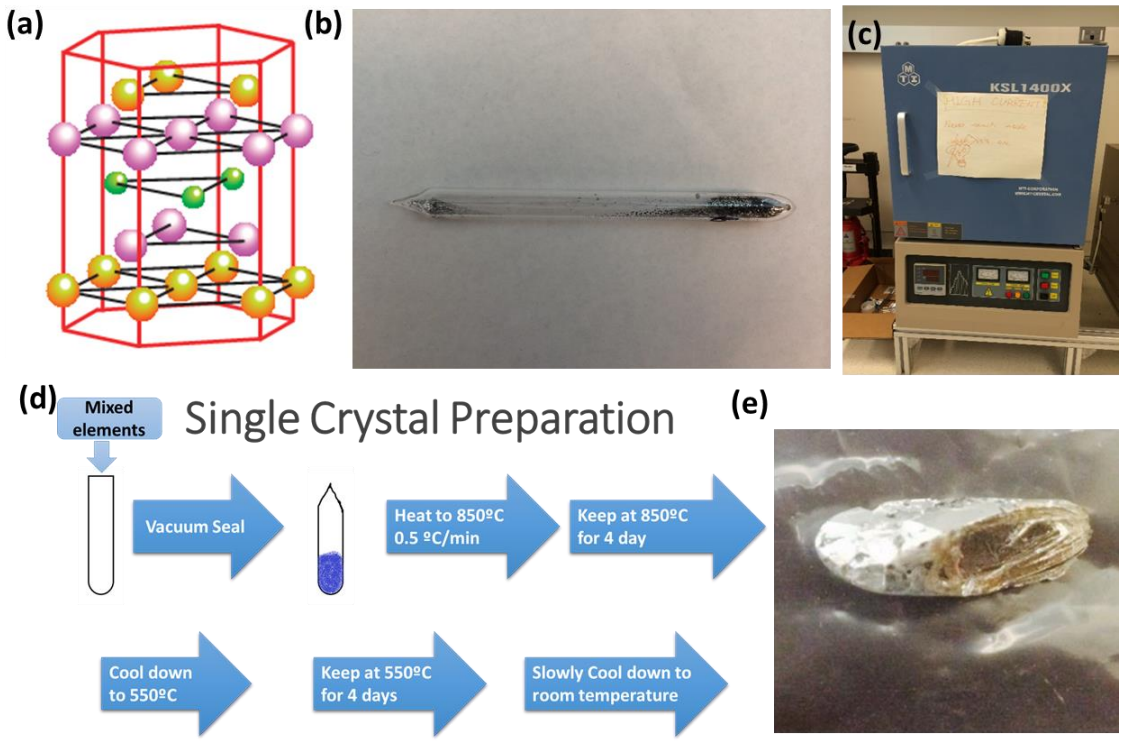

Fig. 2.5 Single crystal BSTS preparation. (a) Crystal structure of BSTS. (b) Mixed stoichiometric elements are sealed in quartz tube. (c) Furnace used for sample growth. (d) Growth program. (e) BSTS crystal produced by multi-step heating procedure. A shiny plane was found after a few times of cleavage. And thin flakes could be peeled off from shiny plane.

Fig. 2.5 shows the detail preparation procedure for BSTS single crystals. Shiny planes can be easily found after a few cleavages of the as-grown BSTS crystal (Fig. 2.5 e). Then thin flakes with a typical thickness ~20 μm are cleaved from the single crystal pieces. Fourier Transform Infrared spectroscopy (FTIR) is applied to characterize thickness of bulk samples. After characterization, the flakes will be connected by a combination of indium dots and gold wires for electrical transport measurement under a Van der Pauw configuration.

2.1.3 Fourier Transform Infrared Spectroscopy

Fourier transform infrared spectroscopy (FTIR) is a widely used technique to obtain the infrared spectrum of absorption, emission or reflection of a sample. An FTIR spectrometer simultaneously collects high spectral resolution data over a wide spectral range. This confers a significant advantage over a dispersive spectrometer which measures intensity over a narrow range of wave lengths at a time.

Rather than shining a monochromatic beam of light at the sample, this technique shines a beam containing many frequencies of light at once and measures how much of that beam is absorbed by the sample. Next, the beam is modified to contain a different combination of frequencies, giving a second data point. This process is repeated many times. Afterwards, a computer takes all the data and works backwards to infer what the absorption is at each wavelength. The information from all wavelengths is collected simultaneously, resulting in a higher signal to noise ratio in a given scan-time.

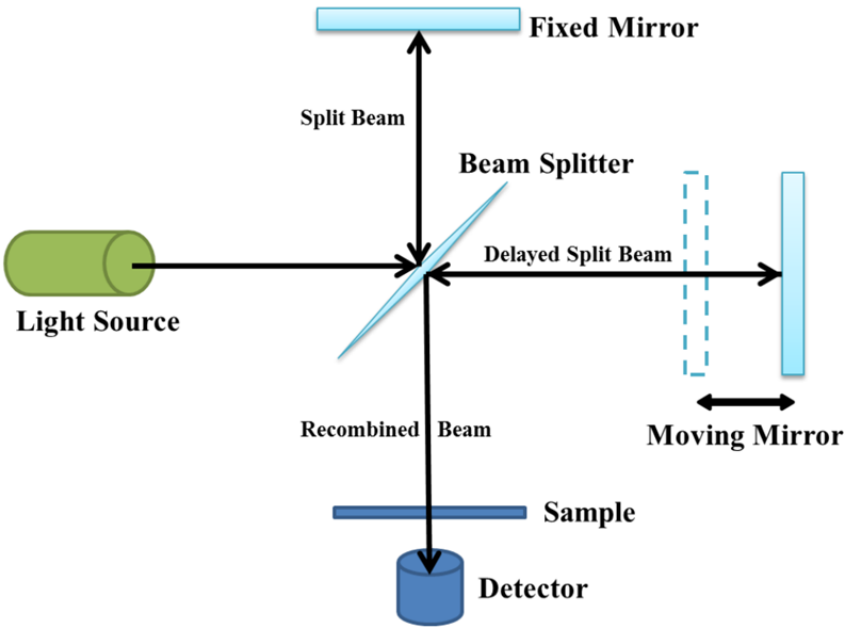

Fig. 2.6 Schematics of FTIR.

Fig. 2.6 displays the schematic illustration of FTIR set-up. The transmittance T and reflectance R are both recorded within the range of wavenumbers from 400 cm^{-1} to 7000 cm^{-1}. However, the instrument has a cut-off frequency in the lower limit of 500 cm^{-1}. A sharp decreases can be observed when the wavenumber is approaching 500 cm^{-1} in both reflectance and transmittance spectra.

A typical reflectance spectrum of BSTS thin flake is present in Fig. 2.7. In the high frequency range (> 2500 cm^{-1}), R stays a constant, which can be used to calculate the dielectric constant by the following equations,

$$R = \left(\frac{n_1 - n_2}{n_1 + n_2}\right)^2$$

The infrared light is incident from air to the flake, then n_1~1 and $n_2=\sqrt{\mu\varepsilon} \approx \sqrt{\varepsilon}$, where μ~1 in BSTS. Therefore, one can have

$$n_2 = \left(\frac{1+\sqrt{R}}{1-\sqrt{R}}\right),$$

Where R should be the reflectance with infinite frequency, but here high frequency R can be used as an approximation. The high frequency R from different flakes are extracted and averaged. One can easily get the dielectric constant for BSTS samples with reflectance R put into the equation above. The dielectric constant $\varepsilon_r = 12.25$ and the refractive index n=3.5.

On the other hand, in the intermediate range (1000-2000 cm^{-1}), there are interference fringes in R which are a result of the Fabry-Perot interference of the infrared light reflected by the two flat specular surfaces of the flake: one from top surface and the other from bottom surface. The interference fringes can be used to determine the flake's

thickness as follows and both the reflectance R and transmittance T show the consistent result of film thickness.

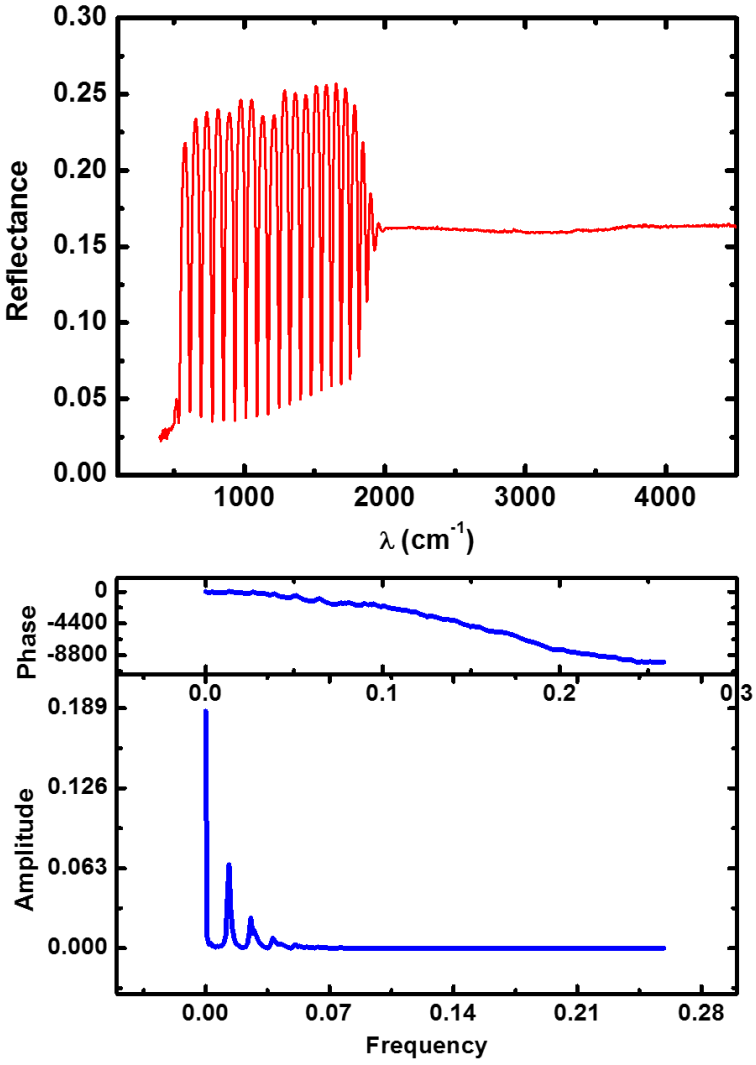

Fig. 2.7 Reflectance spectrum of BSTS thin flake (top panel) and Fourier transform analysis (bottom panel).

We perform the fast Fourier transform (FFT) on the oscillation part of reflectance spectrum. The oscillation peaks will be visible after FFT analysis. The peak position represents the optical path difference of the infrared light reflected by the top and bottom

surfaces of the sample. Thus, we can have a relationship between peak position (P), film thickness (d) and refractive index (n):

$$P = 2d \cdot n$$

Accurate thickness value will be got by averaging the multiple measurements result. For the sample shown in Fig. 2.7, the thickness is about 35 μm.

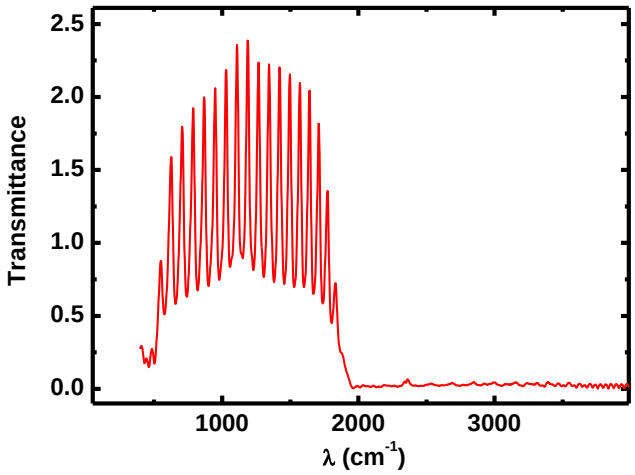

Fig. 2.8 Transmittance spectrum of BSTS thin flake.

The curve shown in Fig. 2.8 is typical transmittance spectrum of the same BSTS thin flake. T decreases to zero due to the cut-off in detector's sensitivity. And on the other side, when the wavenumber range is larger than 2000 cm^{-1}, T goes to zero as well. The infrared photon energy in the high wavenumber range is large enough for the interband transition of electrons in BSTS sample. Therefore, in large wavenumber position (high frequency, high energy), the light is all adsorbed except for the reflected part, leading to zero transmitted signals. However, in the intermediate range, the transmittance signal has oscillation, similar to reflectance behavior. The onset of finite T corresponds to the

interband transition energy related with the Fermi level position. For the same Dirac band structure, lower onset of finite T means lower carrier density and the Fermi level will be closer to the Dirac point, which is another information provided by FTIR result.

2.1.4 Transport Measurements on Bulk BSTS Device

The Van der Pauw method is a technique commonly used to measure the resistivity and Hall coefficient of a sample. It is widely used to accurately measure the properties of a sample in any arbitrary shape, as long as the sample is approximately two dimensional solid material.

There are five conditions that must be satisfied to apply this method:

1, The sample must have a flat shape of uniform thickness.

2, The sample must not have any isolated holes.

3, The sample must be homogeneous and isotropic.

4, All four contacts must be located at the edges of the sample.

5, The area of contact of any individual contact should be at least an order of magnitude smaller than the area of the entire sample.

In our experiment, we press indium dots hard to fabricate the contacts and use Au wire to connect the contact with pins on the sample holder (as shown in Fig. 2.9). The sample holder is installed in a close-cycle refrigerator which has a measurement temperature ranging from 30 K to room temperature.

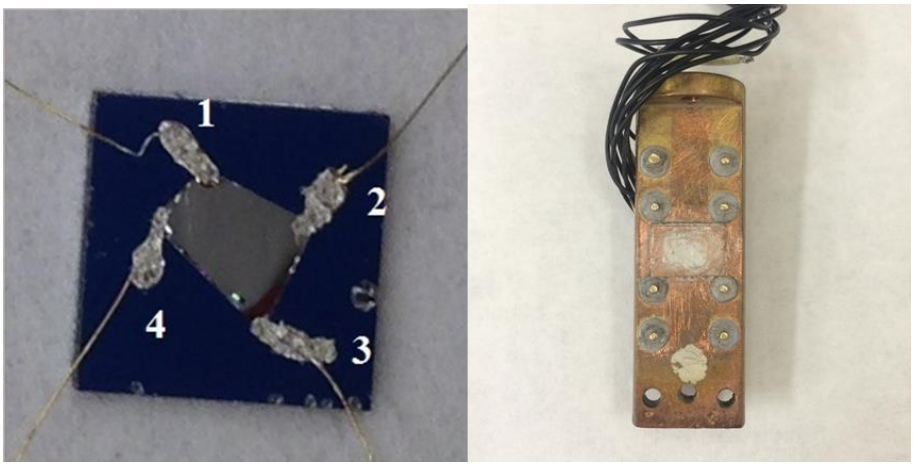

Fig. 2.9 bulk device geometry and sample holder.

The typical Van der Pauw measurement method is described as following. To obtain the sheet resistance R_{xx} of the sample, we apply a current along one edge of sample, for example current is from 1 to 2 in Fig. 2.9 and measure the voltage across 3 and 4. Therefore we get $R_{12,34}=V_{34}/I_{12}$. On the other hand, introduce the current from 2 to 3 and measure the voltage across 4 and 1. Then we get another resistance value $R_{23,41}=V_{41}/I_{23}$. Combine the two resistance value and the sheet resistance of bulk sample can be given as below:

$$e^{-\pi R_{12,34}/R_s} + e^{-\pi R_{23,41}/R_s} = 1.$$

By putting the $R_{12,34}$ and $R_{23,41}$ value into this equation, we can easily find the sheet resistance R_s of bulk sample. The 3D resistivity can be further calculated as

$$\rho_{3D} = R_s \cdot t$$

Where t is the sample thickness which is inferred by the FTIR result. For more accurate measurement, the following equation could be considered:

$$e^{-\pi R_{vertical}/R_s} + e^{-\pi R_{horizontal}/R_s} = 1,$$

Where $R_{vertical}=(R_{12,34}+R_{34,12})/2$ and $R_{horizontal}=(R_{23,41}+R_{41,23})/2$. And further improvement in the measurement can be made when applying $R_{vertical}=(R_{12,34}+R_{34,12}+R_{21,43}+R_{43,21})/2$ and $R_{horizontal}=(R_{23,41}+R_{41,23}+R_{32,14}+R_{14,32})/2$ in the equation. For the Hall measurement on the other hand, the current is flowing through two opposite contacts (e.g. contact 1 and 3 in above figure) and measure the voltage across the other two opposite ones (e.g. contact 2 and 4) when sweeping the perpendicular magnetic field. We can also check the Hall voltage by applying the current through 2 and 4 and recording the voltage across 1 and 3. Averaging the Hall voltage from these two setups will lead to a more accurate Hall behavior as a result.

We fabricate a series of $Bi_{2-x}Sb_xTe_{3-y}Se_y$ (BSTS) samples with different x:y composition. Fig. 2.10 shows temperature dependent resistance of a bulk device (~30 μm thick) cleaved from $BiSbTeSe_2$ (x=1, y=2). Clearly, its resistivity (<50 mΩ·cm) is still very low and doesn't present an insulating bulk state as the temperature is cooling down. Fig. 2.11 is the Hall measurement plot of $BiSbTeSe_2$ sample, which shows the p-type carrier density is $2\times10^{18}/cm^3$. The high carrier density indicates that the Fermi level still locates in the bulk valence band not the bulk band gap. The quality of $BiSbTeSe_2$ is not ideal as expected from band structure calculation owing to the unintentional doping during the crystal growth. We also try the different x:y compositions in the BSTS sample growth, and finally find the $Bi_{1.5}Sb_{0.5}Te_{1.7}Se_{1.3}$ (x=0.5, y=1.3) has a very high bulk resistivity over 1 Ω·cm and truly insulating resistance vs. temperature behavior.

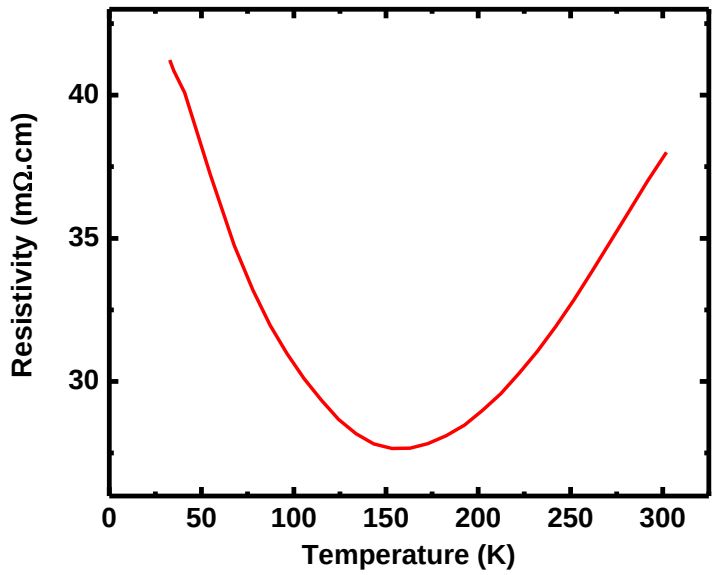

Fig. 2.10 Temperature dependent resistivity of $BiSbTeSe_2$ bulk device.

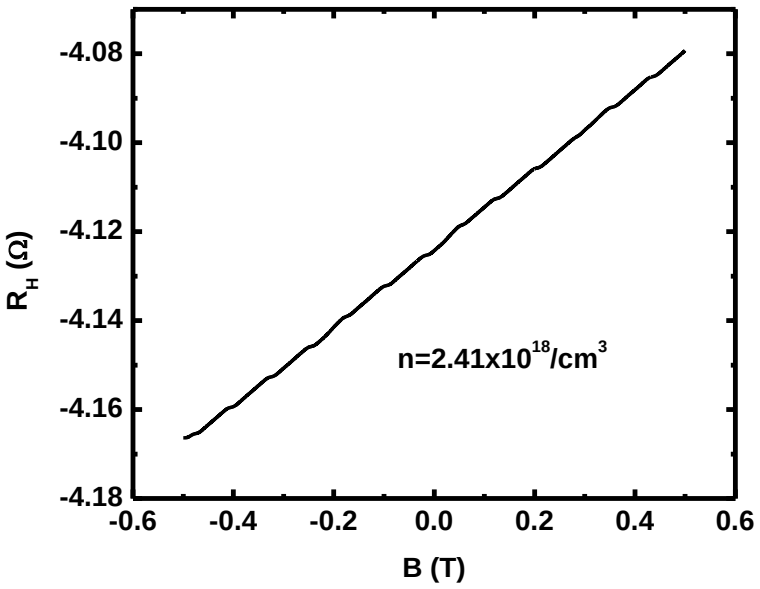

Fig. 2.11 Field dependent Hall resistance in $BiSbTeSe_2$ bulk device.

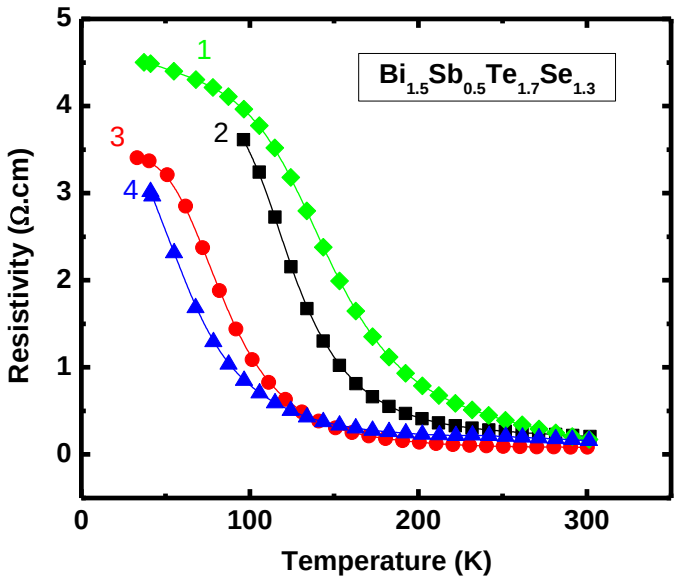

Fig. 2.12 Temperature dependent resistivity of 4 bulk devices from $Bi_{1.5}Sb_{0.5}Te_{1.7}Se_{1.3}$ single crystal.

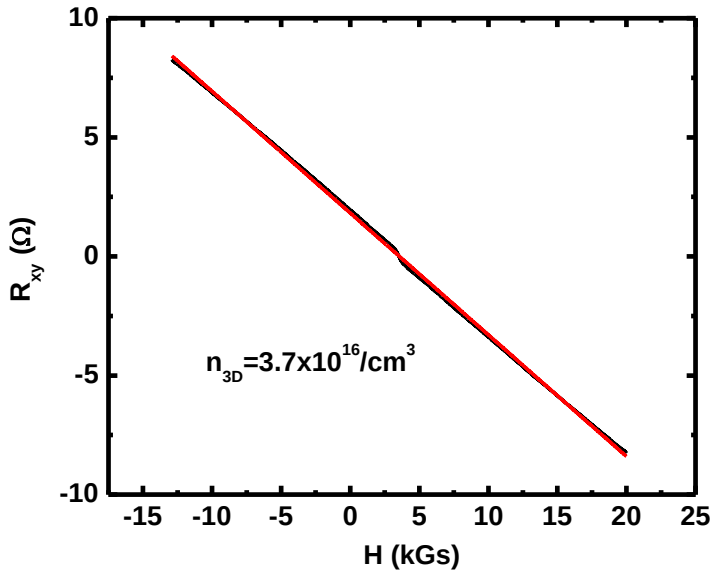

Fig. 2.13 Typical field dependent Hall resistance in $Bi_{1.5}Sb_{0.5}Te_{1.7}Se_{1.3}$ bulk device.

In Fig. 2.12 (shown above), the BSTS bulk sample at the optimized composition (x=0.5, y=1.3) presents a large bulk resistivity exceeding 1 Ω·cm at low temperatures and the insulating property over the whole temperature range. It should be noted that, although the four samples are cleaved from the same batch BSTS crystal, the resistivity value is found to be sample dependent with a variation factor of 1.5 under the same sample composition. This may be due to the different level of defect concentrations. Nevertheless, the activation behavior is reproducible for different bulk samples within the same batch and the activated regime can be clearly found by plotting (see below for detail). We need to point out here that the magnitude of 3D resistivity at low temperature is significantly larger than any other TI materials, such as Bi_2Se_3 (ref 21), $Bi_{0.9}Sb_{0.1}$ (ref 1), Ca-Bi_2Se_3 (ref 20) and Bi_2Te_2Se (ref 25). Table 2.1 shows a comparison of general bulk resistivity from different TI materials, which strongly support that BSTS at the optimized composition is an ideal candidate for surface dominated (bulk insulating) transport research.

Materials	Resistivity (mΩ·cm)	Hall carrier density (/cm^3)
Undoped Bi_2Se_3	0.5	10^{18}-10^{19}
$Bi_{0.9}Sb_{0.1}$	10	~10^{18}
Ca-Bi_2Se_3	100	10^{17}-10^{18}
Bi_2Te_2Se	~500	5x10^{17}
$Bi_{1.5}Sb_{0.5}Te_{1.7}Se_{1.3}$	up to 5000	2x10^{16}

Table 2.1 A comparison of 3D bulk resistivity and Hall carrier density among different topological insulator materials.

The resistivity of BSTS at the optimized composition has 4 orders of magnitude increase compared with undoped Bi_2Se_3 metallic sample. At the same time, the Hall measurement (Fig. 2.13) generally displays a carrier density as low as ~$10^{16}/cm^3$, 2 orders of magnitude decrease than Bi_2Se_3 sample (Table 2.1), indicating the huge amount of Se vacancies have been sufficiently compensated by the (Bi,Sb)/Te anti-site defects. The truly insulating bulk states together with the decreasing of carrier density confirm the possibility of controlling Fermi energy location in the Dirac band structure when simultaneously tuning the Sb and Se composition in BSTS system.

Since the overall temperature dependence of resistivity is similar (shown in Fig. 2.12), we use the BSTS sample 0507 curve (Fig. 2.14) to analyze how to divide the temperature dependent behavior into three regimes:

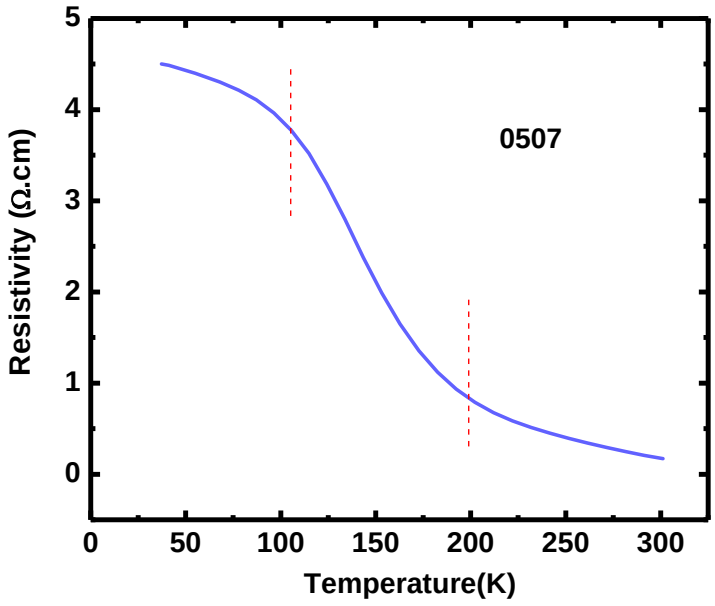

Fig. 2.14 Temperature dependent resistivity in BSTS sample 0507. The red dashed line indicates the approximated boundary of three different regimes.

(1) Activated regime: In the high temperature range above 200 K, the resistivity data can be fitted with the Arrhenius law:

$$\rho_{xx} \sim \exp(\Delta/k_B T)$$

here Δ is the activation energy and k_B is the Boltzman constant (~8.6×10^{-5} eV/K). In the Fig. 2.15, we show the Arrhenius plot of the data with the linear fitting to extract the activated gap for device BSTS 0507. The temperature range for activated regime is from 300 K to ~200 K. The obtained activation energy is about 33 meV displayed in Fig. 2.15. The activation energy is comparable with the reported values for BSTS[27] and BTS[51] bulk samples.

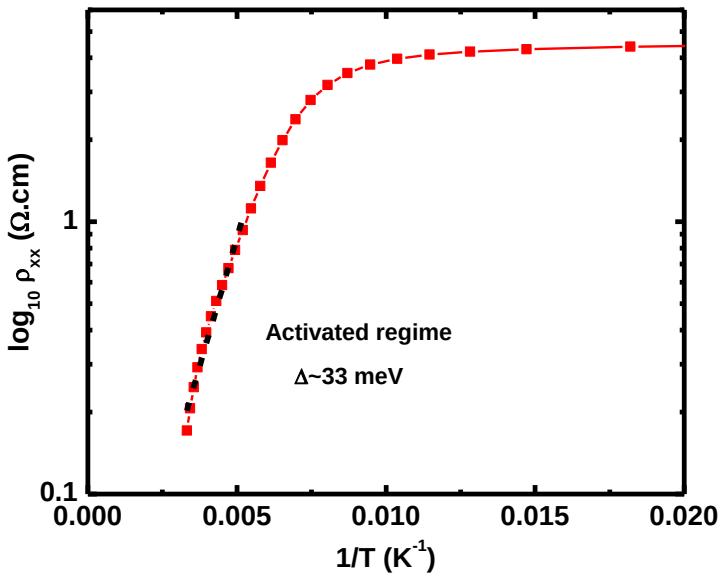

Fig. 2.15 Arrhenius plot and activation energy of BSTS sample 0507.

(2) Variable-range hopping regime: Below the temperature lower limit of the activation behavior mentioned above (~200 K), the resistivity could be described by a 3D variable-range hopping (VRH) behavior:

$$\rho_{xx} \sim \exp\left[(T/T_0)^{-1/4}\right]$$

here T_0 is a constant which depends on the density of states at the Fermi level E_F. We do the log plot for conductivity σ_{xx} vs. $T^{-1/4}$ for the same device as shown in Fig. 2.16. A reasonable linear fit displays for the temperature range from 240 K to 130 K, suggesting that the transport property is dominated by 3D VRH behavior in corresponding region. However, it is worth to note that the temperature range where 3D VRH behavior dominates appears to have an overlap with the activated one. For instance, in this device 0507, the temperature from 240 K to 190 K could be explained by both mechanisms.

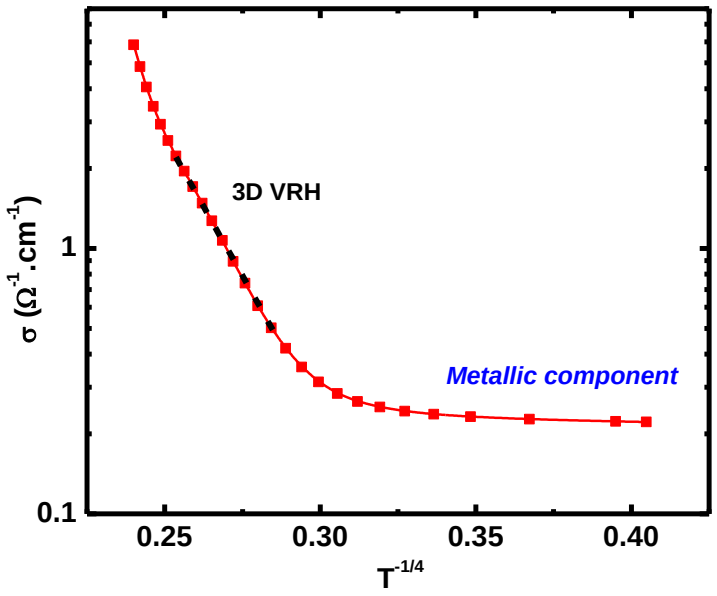

Fig. 2.16 3D VRH plot of the conductivity (T) data, which displays both VRH region and parallel metallic component.

(3) Saturation regime: At low temperature (< 100 K), the conductivity σ_{xx} tends to saturate (deviation from the fit in Fig. 2.16), implying the existence of a parallel conduction of surface states. Due to the measurement limit in the close-cycle system (minimum temperature ~ 30 K), we cannot evaluate the extended states (surface contribution) when approaching zero-temperature limit. The resistivity behavior at lower temperatures will be discussed in later transport study when a PPMS system is used. The saturation regime due to the parallel channels from bulk and surface respectively in low temperature can be further supported by the analysis of weak anti-localization (WAL) effect and 2-band fit of nonlinear Hall resistivity (see chapter 3).

In the last part of this section 2.1.4, I want to discuss how to estimate the surface contribution in BSTS samples by simply comparing thickness dependent saturation resistivity.

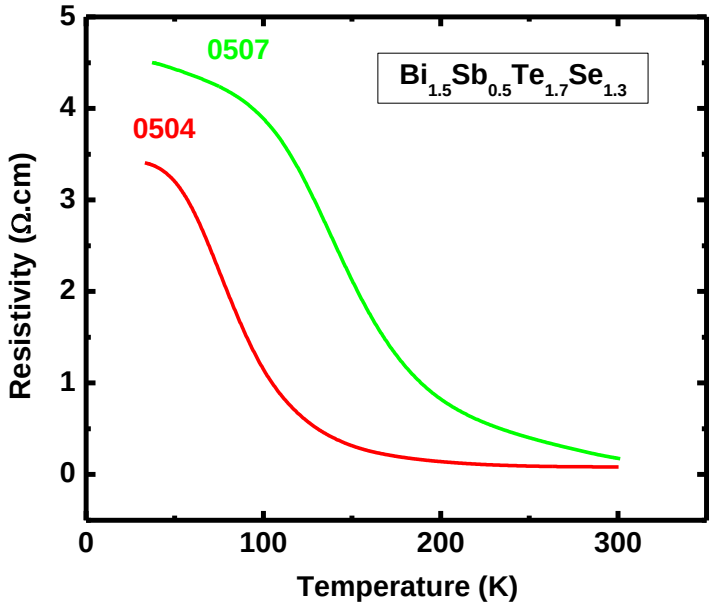

Fig. 2.17 Temperature dependent resistivity of two BSTS samples with different thickness.

Fig. 2.17 shows the resistivity data from two different samples, which are cleaved from the same crystal but have different thicknesses. The sample 0504 has a thickness of 30 μm and the sample 0507 is 60 μm thick instead. The overall behavior of ρ_{xx} (T) is similar between the two samples curves, both of which could be divided into three regimes as discussed above. Nevertheless, a striking difference lies in the low temperature region where their resistivity approaches the saturation value : ρ^{sat}= 3.4 Ω·cm for 0504 and 4.5 Ω·cm for 0507 respectively. It is lower in the thinner sample (0504), implying a larger relative surface contribution in the parallel channels mode. Note, the difference in resistivity will disappear at high temperatures when the bulk conduction dominates and the parallel transport channels quench. From the difference in saturation ρ_{xx} and thickness in two samples, we can easy calculate the total conductance $\sigma_{xx}\cdot t$ for each sample respectively. Assuming the surface conductance and bulk resistivity are constant parameter depending on the BSTS crystal quality and band structure at optimized composition, we can have:

$$\sigma_{xx}\cdot t = G_s + \sigma_b \cdot t$$

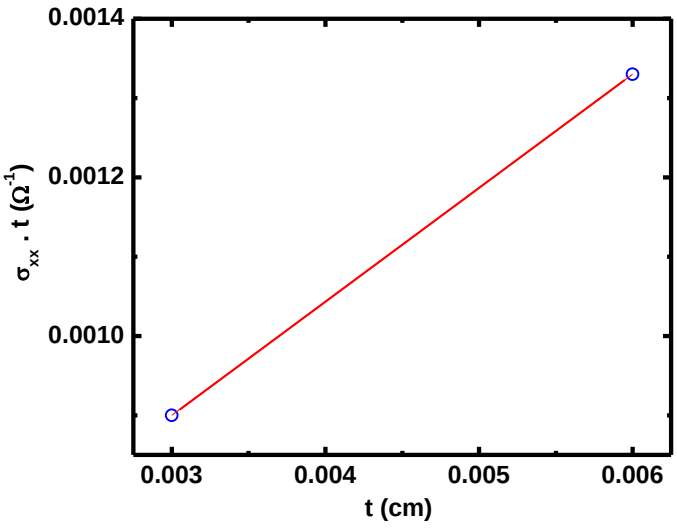

Fig. 2.18 Total conductance vs. thickness for two BSTS samples.

Here G_s is the conduction from surface channel and σ_b is the bulk conductivity. By putting the corresponding value of these two samples, we can derive the plot in Fig. 2.18 and obtain $G_s \sim 4.7 \times 10^{-4}\ \Omega^{-1}$ and $\sigma_b = 0.143\ \Omega^{-1}cm^{-1}$. More importantly, from the obtained parameters, we can infer the fraction of surface contribution to total conductance:

$$\text{Surface channel fraction} = G_s/(G_s + \sigma_{xx} \cdot t)$$

As a result, the fraction of surface conduction is 35% for 0507 sample (~60 μm thick) and 52% for 0504 sample (~30 μm thick) respectively. We can also expect that with the reduced thickness of BSTS samples the surface dominated transport could be realized in topological insulator device.

2.2 Topological Insulator Nanodevice Fabrication, Measurement and Electron Beam Irradiation

2.2.1 Nanodevice Fabrication Procedure

Nanodevices typically mean the device has a much thinner thickness than bulk samples. With scotch tape exfoliation technique, one can easily find the thin flakes with a thickness ranging from 100 nm to 10 nm. The thin nanodevice is expected to have significantly reduced bulk carrier density and enhanced surface contribution, therefore serves as a better candidate to study the topological surface states property than bulk samples. However, it is not easy to identify very thin TI nanodevice under the microscope since the color of thin flakes will become dark in light background and unclear. Therefore, it is also difficult to tell the exact thickness of nanodevice thin flake from the exfoliation step. Usually, the thin flakes used for TI nanodevice fabrication has a thickness around 50 nm, which could be confirmed by the atomic force measurement (AFM) across the device edge. In this section, we will focus the device fabrication by standard spin-coating, e-beam

lithography (EBL) and angle deposition of e-beam evaporator. To accurately locate the thin flake used for device fabrication, a typical alignment mark is necessary.

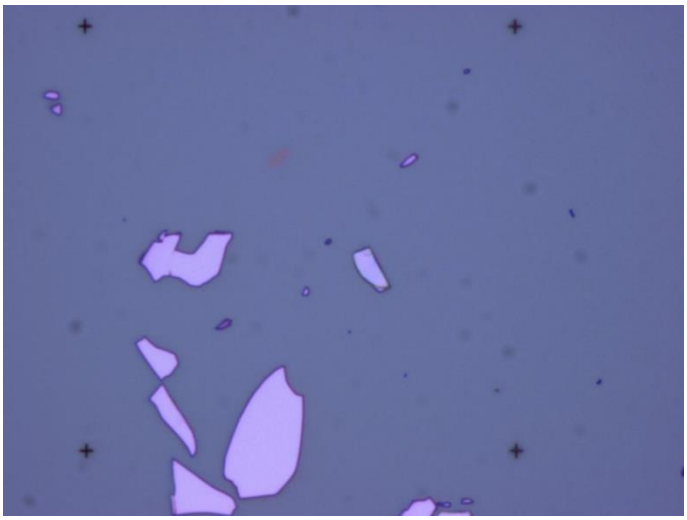

Fig. 2.19 Thin TI flakes under microscope ×500 times magnitude enlarge

The first step of TI nanodevice fabrication is always identifying the proper thin flake under the microscope after exfoliation on SiO_2/Si substrate. The thickness of TI thin flakes can be inferred by their color under the microscope. Nanoflakes with purple colors (as shown in Fig. 2.19) are the thinnest ones while the yellowish color indicates thick flakes. Pink flakes have thickness between the purple ones and yellow ones.

After the thin flake position on the substrate has been recorded, a layer of MMA and PMMA are spin coated separately at the speed of 4000 rpm for 45 second with the ramping rate of 10000 rpm/sec. The MMA and PMMA resist combination is used to create an undercut structure since the MMA resist is easier to be exposed in the same dose of electron beam current. The estimated thickness of MMA and PMMA layer is 300 nm each.

The substrate should be baked on a hot plate after spin coating of each resist. The baking temperature for MMA is around 150 ℃ and baking time is 5 min, however for PMMA the baking temperature should be slightly higher around 170-180 ℃ with same baking time. Spin coating is a critical procedure during the device fabrication, which requires the uniform resist surface and hard baking quality. It will not only affect the focus and pattern resolution in the lithography, also decide the developer and lift-off efficiency in the lateral steps.

The substrate is then loaded into a high vacuum chamber for e-beam lithography. The alignment mark covering the chosen thin flake location is first patterned (Fig. 2.20) and developed in the beaker containing the MIBK: IPA=1:3 solvent. To ensure the visible alignment mark when designing the device pattern and further lithography focus, the metal deposition of Cr (5nm)/Au (40 nm) is performed on the substrate by e-beam evaporator, followed by the acetone lift-off process.

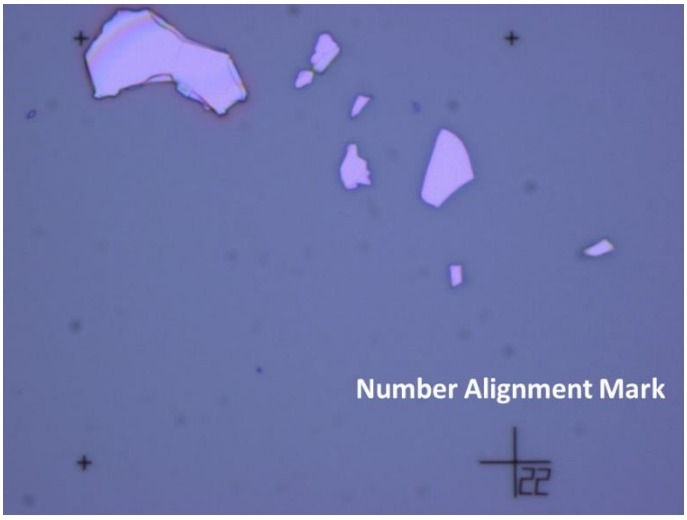

Fig. 2.20 Alignment mark number after lithography patterning.

The device contact (leads and pads) is designed by the CAD software. After that spin coating and e-beam lithography procedure is repeated to create the device pattern, typically a six-terminal Hall bar structure, with the help of alignment mark defined previously. Since the topological insulator flake is usually 50-100 nm much larger in thickness than graphene or other two-dimensional material devices, the usual perpendicular deposition with a directional electron beam does not give a good contact electrode. We design the angle deposition technique with an inclined sample holder specially for TI nanodevices as shown in Fig. 2.21. The surface contact between TI film and Au layer has been enhanced due to continuous deposition covering thin flake edge. As a result, the deposited electrodes will be kept well after lift-off process. The deposition angle is 45 °and the incident flux is perpendicular to the long edge of the device.

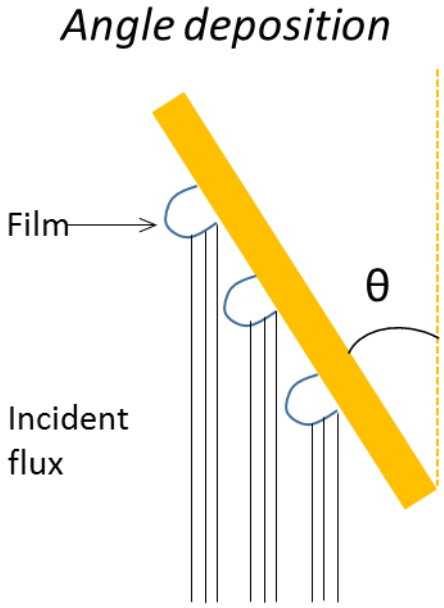

Fig. 2.21 Schematic of angle deposition technique.

Fig. 2.22 shows am optical image of TI nanodevice after fabrication. Both magneto-resistance and Hall effect measurements can be performed simultaneously under the six-terminal structure. However, we need to first point out here the topological surface states are very vulnerable when being exposed in the air. Either the oxidation or unintentional doping of defects during the fabrication process will lead to an irreversible change of sample property. The protection approach has not been taken into consideration in the device fabrication steps above and it is also hard to avoid any contamination in a complex set of procedures when there is no capping layer on the TI exfoliated film surface. We begin to notice that essential post-fabrication method must be conducted to remove the contamination on the surface or localize the trivial bulk carriers, which could lead to a non-trivial metallic surface states dominated transport property.

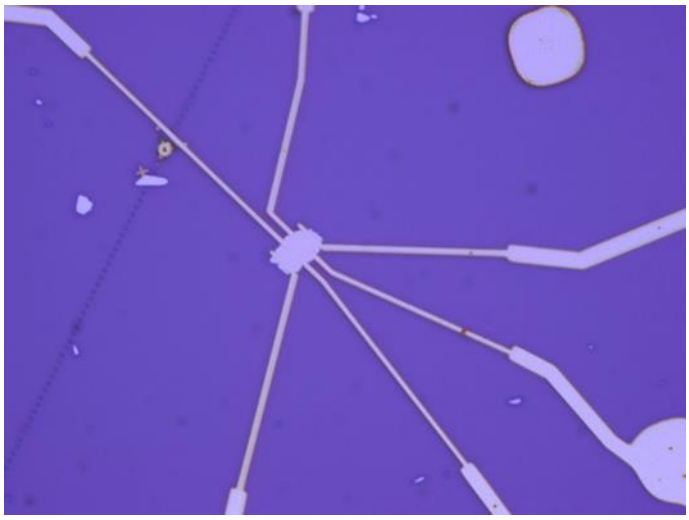

Fig. 2.22 Optical image of a TI nanodevice.

2.2.2 TI Nanodevice Measurements

BSTS nanodevice electrical characterization is performed in a Quantum Design Physical Property Measurement System (PPMS) with a base temperature down to 1.9 K and rotation sample holder. The system is equipped with a superconducting magnetic up to 14 Tesla.

Fig. 2.23 is a temperature dependent sheet resistance curve of one BSTS nanodevice (#0507-107). The resistance has very weak temperature dependence with a relative change of 10% when cooling from 300 K to 1.9 K. And meanwhile it displays the metallic behavior in most temperature range, only showing a slightly upturn below 50 K. This behavior for TI nanodevice is markedly different than insulating bulk states shown in bulk samples before exfoliation, which first indicates that excessive defects may be introduced during the device fabrication.

The field-dependent magneto-resistance (MR) measurement is also taken when sweeping a magnetic field perpendicular to the sample plane. As is displayed in Fig. 2.24, a sharp low field dip is observed, indicating the weak anti-localization effect due to the strong spin-orbit coupling exists in the TI device which is an expected feature of topological surface states. As temperature increases, the MR dip at low B is broadened and finally disappears due to the decrease of phase coherent length at higher temperature (not shown).

The weak anti-localization effect (WAL) is the characteristic of materials of which strong spin-orbit coupling suppresses backscattering due to time reversal symmetry,

resulting in a negative correction to the resistance at zero B-field. The application of a magnetic field breaks the time reversal symmetry, leading to enhanced backscattering and

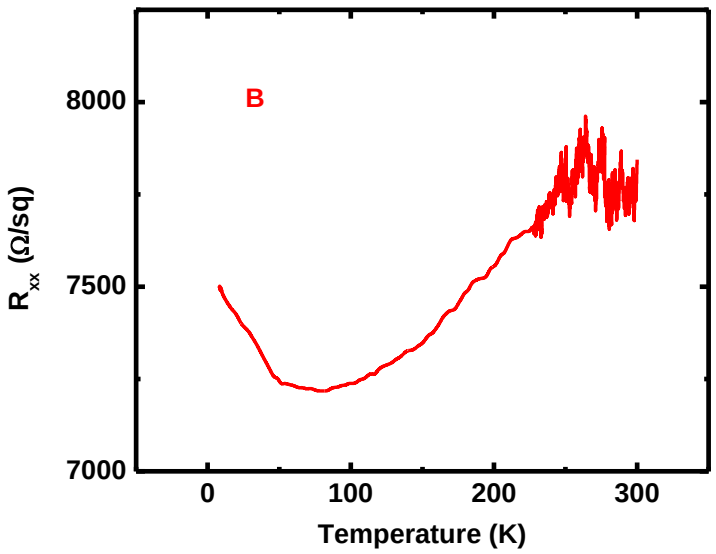

Fig. 2.23 Temperature dependent R_{xx} of a BSTS nanodevice.

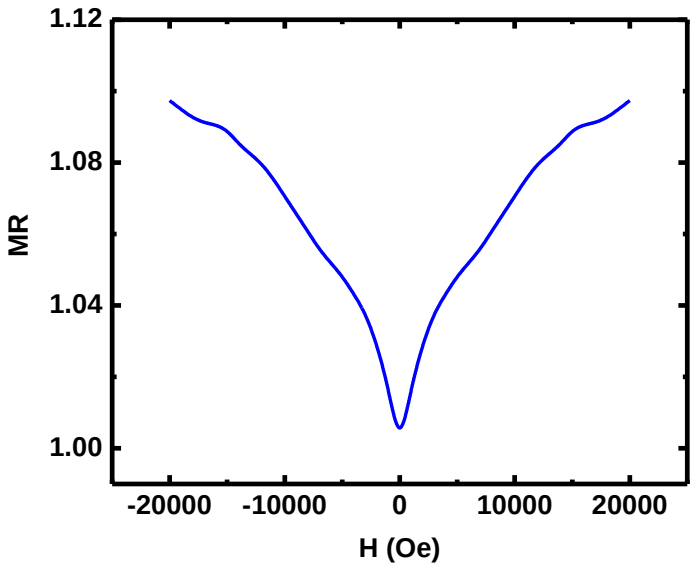

Fig. 2.24 Magneto-resistance curve measured at 1.9 K.

corresponding increase of resistance. However, this effect is not limited to 2D systems, but can also have a contribution from 3D bulk states. To investigate the proper origin of observed WAL signal in TI nanodevice, angle dependent magneto-resistance experiment is performed. The sample is mounted on a rotation holder which could be tilted in the external magnetic field. For measurement orientation, when $\theta=0°$ magnetic field is perpendicular to the sample surface, while for $\theta=90°$ magnetic field is parallel to the sample surface. When $0°<\theta<90°$, $B_z=B\cos\theta$ corresponds to the magnetic field component normal to the sample surface. Let's first take a look at Fig. 2.25 which shows the magneto-resistance as a function of magnetic field B at different angles. Except $\theta=90°$ case (pink line), the WAL phenomenon is present in all directions with a clear cusp in low fields. However, for $\theta=90°$ when B is in the film plane, MR dip feature disappears completely and is replaced by a parabolic field dependence instead. The classical B^2 dependence results from the Lorentz deflection of carriers. We also plot the MR vs. $B\cos\theta$ for different angles excluding 90 ° in Fig. 2.26, which is more interesting. All MR curves coincide with each other at low magnetic fields. This behavior indicates that the observed WAL feature results from the orbital motion of carriers in cylindrical Fermi surface which only depends on the normal component of magnetic field[52]. Therefore, the angular dependent MR data confirm the 2D nature of WAL observed, suggesting this effect comes from the topological protected 2D surface states.

We also investigate the MR behavior in much higher magnetic fields where the Shubnikov-de Haas effect (SdH) appears. At sufficiently low temperatures and high

magnetic fields, the free electrons in the conduction band of a metal, semimetal or narrow band gap semiconductor will behave like simple harmonic oscillators. When the magnetic

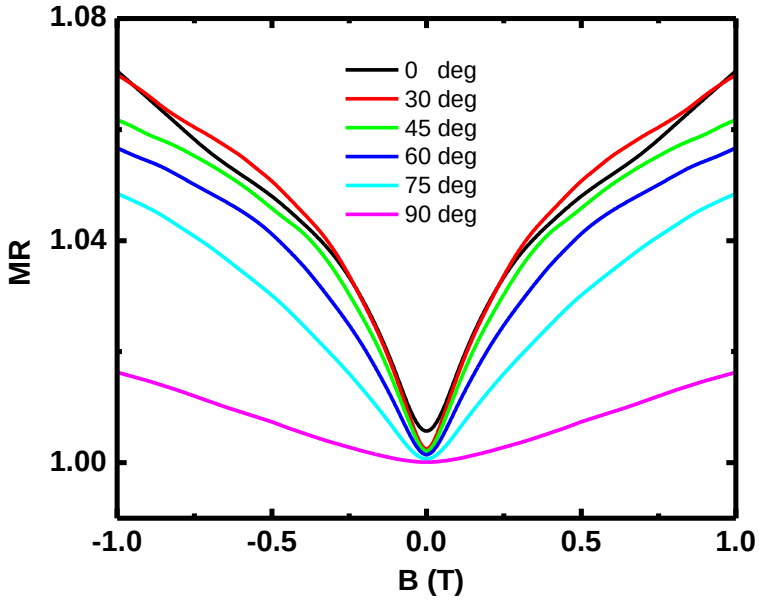

Fig. 2.25 Angle dependent magneto-resistance curves.

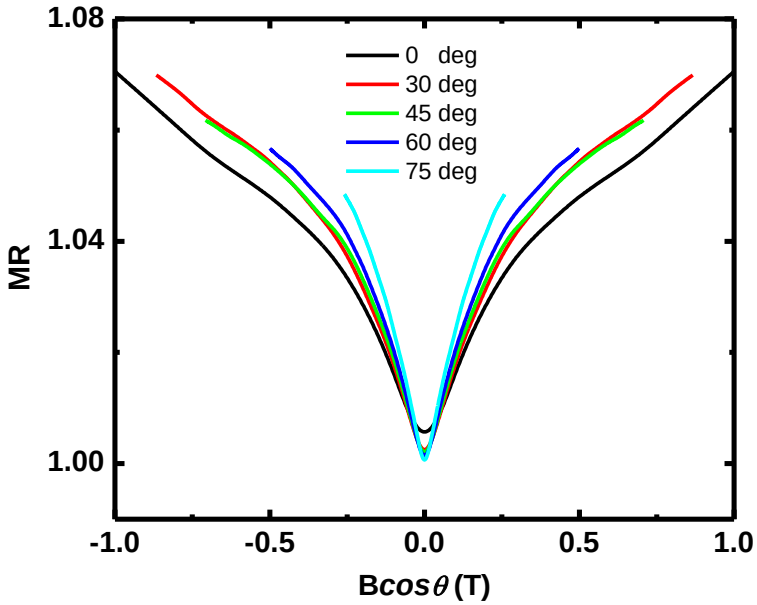

Fig. 2.26 Magneto-resistance vs. Bcosθ at different angles.

field strength is changed, the oscillation period of the simple harmonic oscillators changes proportionally. De Haas-van Alphen effect was first observed for the magnetic susceptibility and people later found similar SdH effect for resistivity, which Landau referred to a direct consequence of the quantization of closed electronic orbits in a magnetic field, and thus as a direct experimental manifestation of purely quantum phenomenon.

The topological surface states are predicted to have high carrier mobility while the bulk only has relatively low carrier mobility due to the strong spin-orbit coupling and time reversal symmetry protection. Hence, the Shubnikov-de Haas effect measurement could be an efficient technique to detect the high mobility surface channels even with the presence of bulk carriers[25,26,53,54].

Under a high magnetic field, the electron states are split into discrete Landau levels which are degenerate with the number of electrons directly proportional to the magnetic field. Considering that there is no spin degeneracy in topological insulator surface states due to the strong spin-orbit coupling, the carrier density required to fully fill each Landau level at a specific perpendicular magnetic field B is $n_{L.L.}=eB/h$. On the other hand, the total 2D carrier density in the k space is $n_{2D}=\pi k_F^2/(2\pi)^2=A/4\pi^2$, where A is the cross-section of the Fermi surface perpendicular to the magnetic field. Hence, the number of fully-filled Landau levels is $N_{L.L.}= n_{2D}/ n_{L.L.}=B_0/B$, where $B_0=\hbar A/(2\pi e)$. Under a changing magnetic field, the Landau level at the Fermi surface will be changed from empty to fully filled, resulting the oscillation of resistance observed. For the change between two neighboring Landau level like N+1 and N, the magnetic field will change from $B_0/(N+1)$ to B_0/N.

Therefore we can achieve the following famous Onsager relation describing the oscillation period in magneto-resistance:

$$\Delta\left(\frac{1}{B}\right) = \frac{2\pi e}{\hbar}\frac{1}{A}$$

If substituting the $A=4\pi^2 n$ into above equation, we can reach a simple relation between the MR oscillation period and 2D carrier density for a spin-filtered surface states:

$$\Delta\left(\frac{1}{B}\right) = \frac{2\pi e}{\hbar}\frac{1}{A} = \frac{e}{h}\frac{1}{n} = \frac{2.42\times 10^{10}}{n\ (cm^{-2})}[T^{-1}]$$

Therefore, the frequency in 1/B is:

$$B = \frac{1}{\Delta\left(\frac{1}{B}\right)} = 4.13\times 10^{-11} n(cm^{-2})[T]$$

To find the surface carrier density from SdH effect, the fast Fourier transform (FFT) should be done for MR periodic oscillation part as a function of 1/B. The given frequency then is proportional to 2D carrier density according to above analysis.

Fig. 2.27 is the magneto-resistance data of BSTS nanodevice at 5 K under high magnetic field. The resistance oscillations are clearly visible starting from 8 T. As the magnetic field increases, the SdH oscillation amplitude increases as well. We can calculate the residual MR or ΔR_{xx} by subtracting a polynomial fit to the background. After the background is removed (shown in Fig. 2.28), the fast Fourier transform processing could be performed on ΔR_{xx} vs. 1/B plot. The single peak position from FFT corresponds to the oscillation frequency with a unit in Tesla. For this device, the oscillation frequency B=110 T. Hence, we can obtain 2D carrier density $n_{2D}=2.7\times 10^{12}/cm^2$ for a spin-filtered surface state, which is much smaller than the carrier density (usually $\sim 10^{14}/cm^2$) extracted from

ordinary Hall measurements. This is the first evidence confirming that SdH oscillation originates from TI surface states. We can also do a simple estimation about the electron

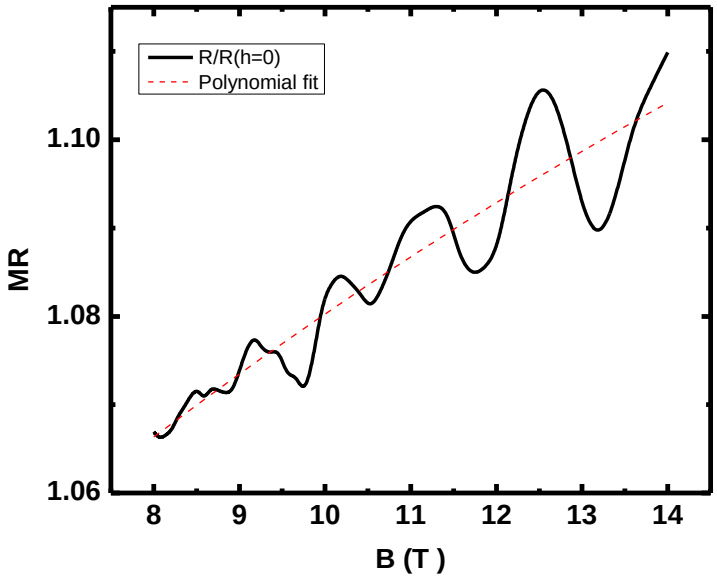

Fig. 2.27 MR presents oscillation part in high field.

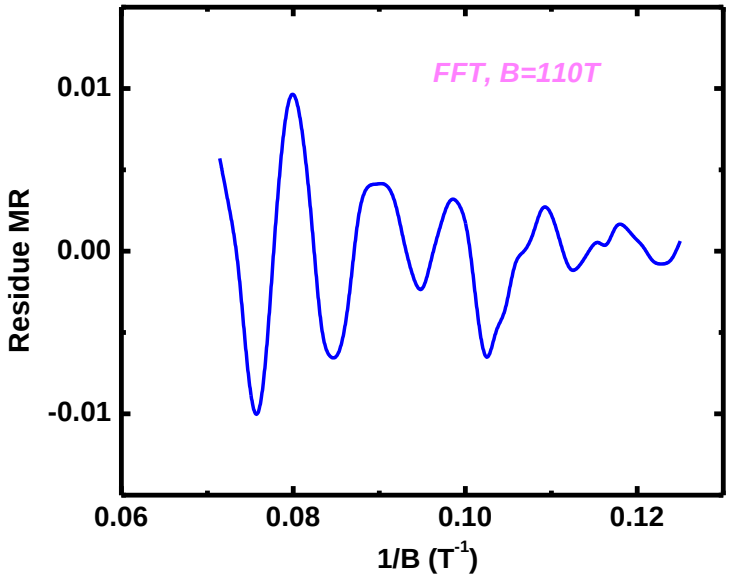

Fig. 2.28 Residue MR vs. 1/B after normal magneto-resistance background is removed.

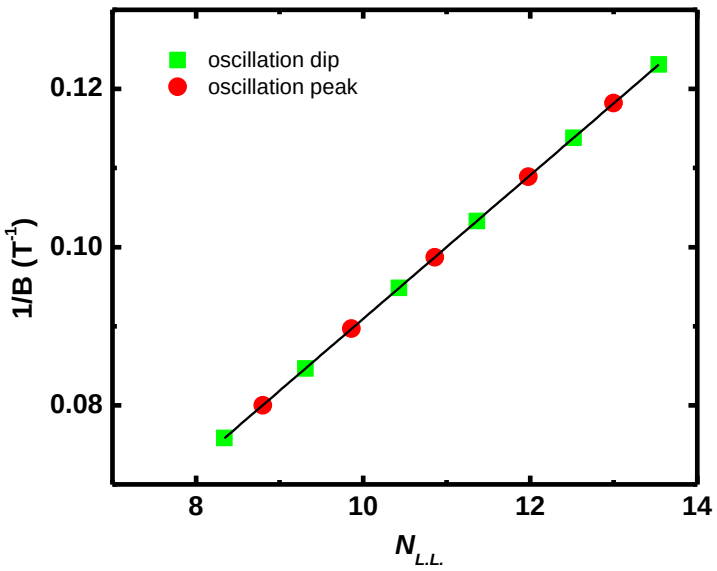

Fig. 2.29 Landau level fan diagram of oscillations. Green square corresponds to the oscillation dip position while red circle corresponds to the oscillation peak position. See main text for detail.

mobility of nanodevice from the onset magnetic field of SdH oscillation. For the first peak in Fig. 2.28 around 8 T to appear, the mobility needs to be μ>1250 cm^2/Vs since $\omega\tau_c = \mu B \gg 1$. Such a high mobility μ does not support the contribution from bulk states which should have carriers with much lower mobility. Our analysis confirms that SdH effect observation is from surface states.

Another interesting plot is shown in Fig. 2.29. The Landau level index is $N_{L.L.}=B_0/B$ where B_0 is the oscillation frequency (~110 T). The dip and peak oscillation position (1/B) is plotted as a function of Landau level number. The data can be fitted to a straight line with slope 1/110 and intercept ~0. The n=1 SdH oscillation thus could be observed under

110 T out of plane magnetic field. This diagram also indicates the SdH oscillation is owing to the formation of Landau levels in high magnetic field.

2.2.3 Topological Anderson Insulator

Probing the topological surface state properties is a research focus of topological insulator community. As we mentioned before, the TI transport could be understood as the surface conducting channel parallel to that of the bulk states. Hence, the total conductance is written as:

$$G = G^s + G^b$$

To reveal the property of topological surface state in 3D TIs, the contribution from bulk conductance needs to be eliminated, which is not as easy as it seems yet. Even for the devices made from high resistivity insulating bulk materials, the resistance is far below the expected value of sample with reduced thickness. Moreover, the resistivity of devices usually has metallic temperature dependence, indicating excessive carriers or defects are introduced during the fabrication. Since the uncertainty in the device fabrication is inevitable, the electrical transport result of 3D TI device is most often dominated by the trivial bulk states, making it difficult to observe the topological phenomenon from surface Dirac fermions.

A surprising discovery of topological Anderson insulator (TAI) was made by Shen group[32] in Hong Kong University and M. Franz group[36] from University of British Columbia. TAI is a new topological phase of quantum matter in three dimensions characterized by disordered insulating bulk and topologically protected conducting surface

states. It is considered a promising solution to make the topological insulator devices truly bulk insulating[35].

Disorder is known to play an important role in low-dimensional physics, leading to electron localization and consequent insulating behavior in the time-reversal invariant systems. By disordering a clean system which is initially in a topological trivial phase, the topologically protected surface states are robust against nonmagnetic disorder while the bulk carriers are remarkably suppressed by localization, leading to the formation of strong TI. This disorder induced topological phase transition is unique and crucial for realizing surface dominated phenomenon in a TI device.

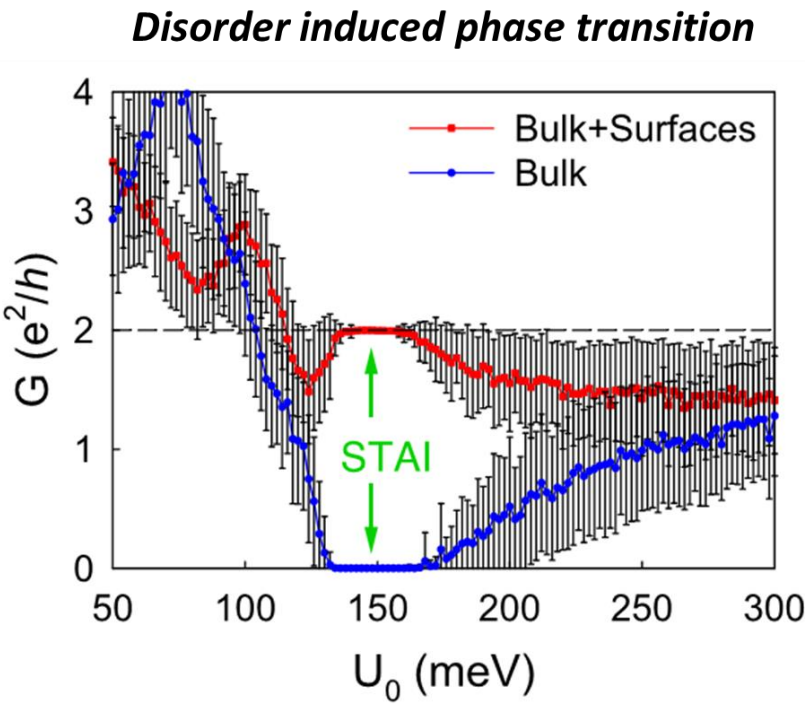

Fig. 2.30 Conductance as a function of disorder strength by theoretical calculation. Adapted from ref 36.

As shown in Fig. 2.30, the bulk states coexist with surfaces when the disorder is absent or very weak, so there is no localization here. When the disorder strength is reaching the critical value U_0~130 meV, the bulk conductance drops to zero, indicating the disorder induced insulating behavior in bulk and persists up to U_0~170 meV. For the disorder strength in the range, the bulk carriers are completely localized and the conductance is attributed to the pure transport of topological surface states. The current will only flow near the surface.

In the following, we will discuss introducing disorder in a controllable fashion and study the effect of disorder on 3D TI transport.

It is known that the e-beam exposure causes the electron density to increase (e.g. HgTe[12]), which needs to be treated with extra care in the nano-fabrication of sensitive devices. However, compared with other process uncertainties in the fabrication, e-beam irradiation (EBI) is a well-controlled technique with easy manipulation of dosage and acceleration energy of electrons. Therefore, EBI could generate disorder into the TI device step by step to localize the bulk carriers and reveal the surface transport. Similar experiment has been reported by our group previously[55]. But in Peng's work, they start with the p-type metallic device (Ca-Bi_2Se_3) and utilize the electron beam exposure to compensate for the hole carriers in p-type device. The experiment result confirms that EBI generates excess electrons which shift Fermi level upward. The mechanism proposed is clearly different than the carrier localization applied in this work. Also, in their experiment, the electron has a low kinetic energy during irradiation. But in this work, the electrons are accelerated at a

higher energy to ensure the disorder electrons are penetrated into the bulk states, forming the localization.

Fig. 2.31 shows the device fabrication procedure in the EBI experiment. The electrodes could be damaged under e-beam exposure. Hence, we only open a small window exposed to the electron beam while most of device electrodes and pads will be covered by the thin PMMA resist layer. After the window is created, the Ar plasma is also applied to gently sputter the oxidation layer or contamination on the exposed TI surface. The sample is then immediately loaded into the EBI chamber for experiment. The schematic of electron beam irradiation on device is demonstrated in Fig. 2.32. The electron

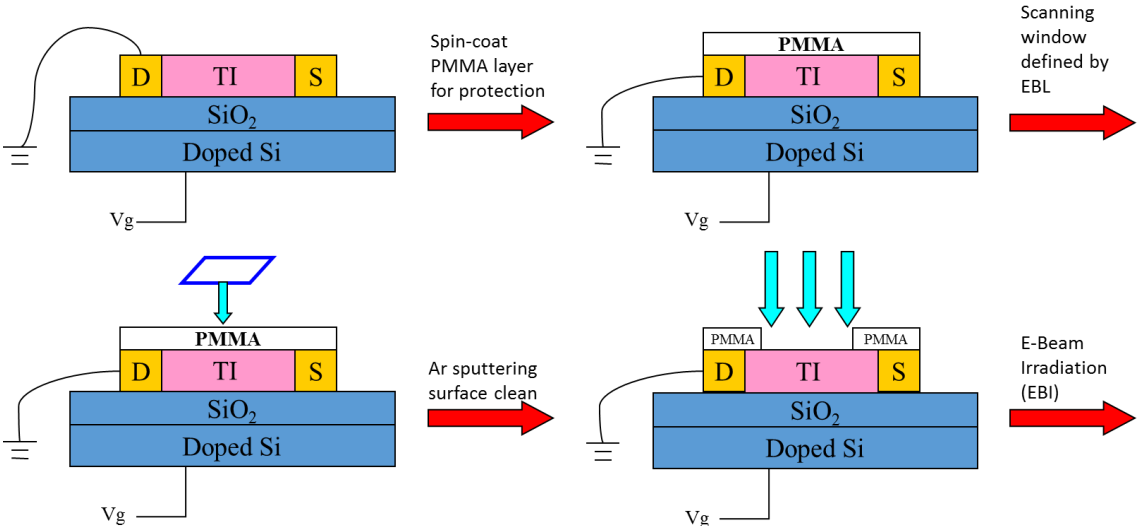

Fig. 2.31 Device fabrication procedure for EBI experiment.

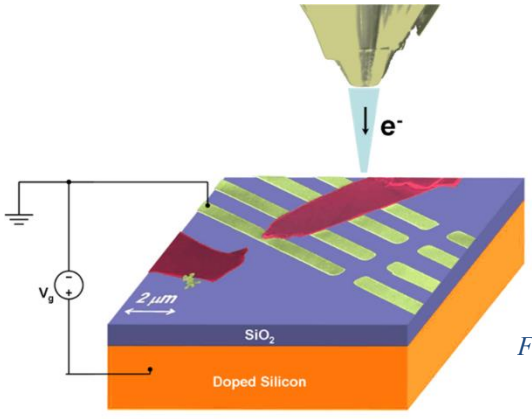

Fig. 2.32 Schematic illustration of EBI.

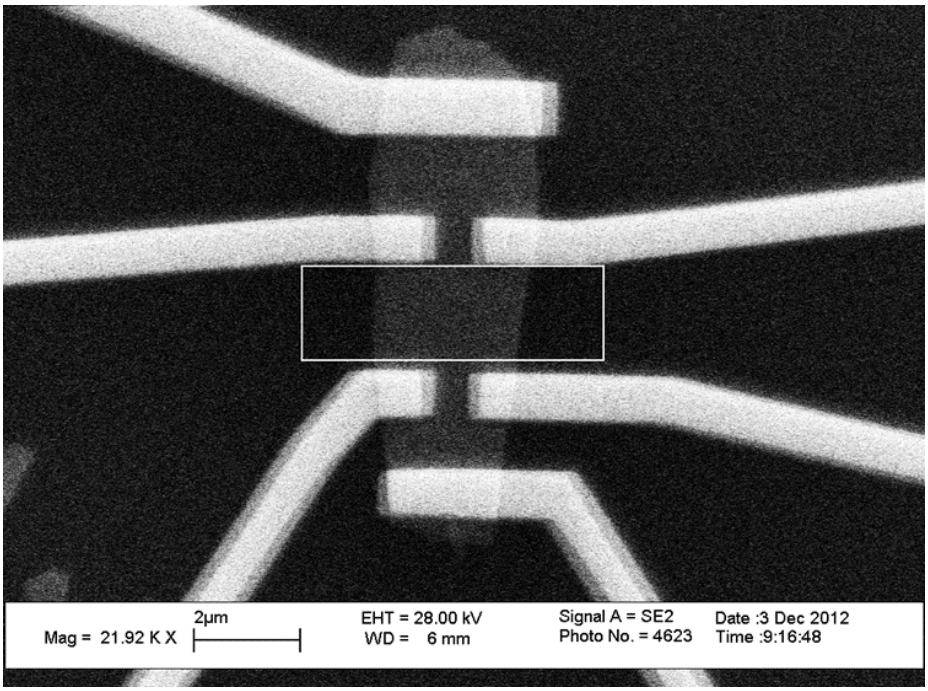

Fig. 2.33 SEM image of TI device taken under EBI experiment.

acceleration energy used is from 20 kV to 30 kV, which is the maximum limit of e-beam source. In each scan, the exposure time is fixed and all the pins of sample will be grounded to avoid the charge accumulation on the device surface. Fig. 2.33 shows a TI device image when performing the EBI experiment. The white rectangular box indicates the scanning area, which is located between four-terminal leads. We increase the exposure time gradually and conduct the electrical transport measurement right after each scan.

Fig. 2.34 displays the temperature dependent R_{xx} after a few e-beam irradiation tests. The sample is a BSTS device with n-type carriers. It is cooled from 300 K to 2 K in a PPMS system. The resistance exhibits a slight drop in both high and low temperature

regions after EBI tests. However, compared with the original curve before EBI (black color), the shape of resistance behavior does not vary significantly, indicating the current

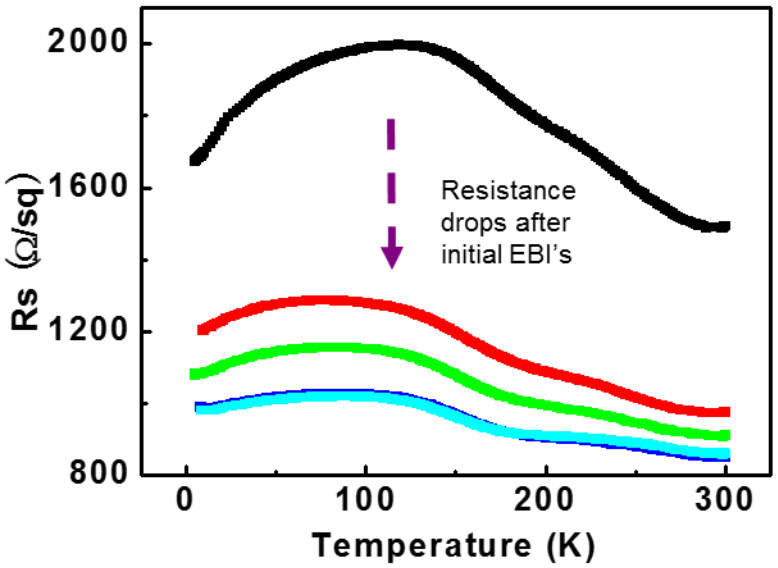

Fig. 2.34 Resistance vs, temperature curve after initial EBI test.

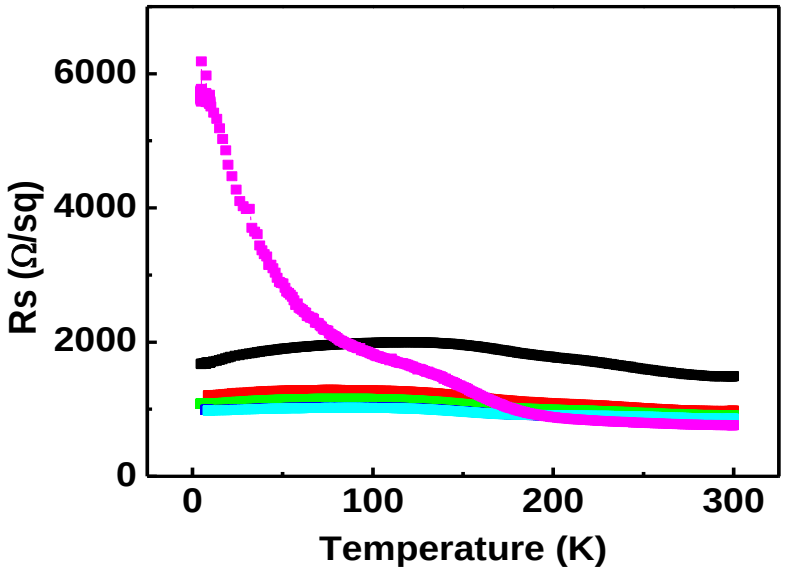

Fig. 2.35 Resistance vs. temperature curve when further EBI dosage is added.

EBI dosage only introduces a few electron carriers into the system, but there is no significant additional scattering impurities introduced by EBI procedure and the device does not have degradation during the experiment. The resistance becomes saturation (not change) after initial EBI scans. Nevertheless, when more EBI dosage is applied, a distinct phenomenon is present as shown in Fig. 2.35. The resistance behavior changes from weak temperature dependence to pure insulating with much higher resistance value in low temperature (pink curve in Fig. 2.35). More importantly, such localization effect only happens in low temperature and the resistance in high temperatures almost stays the same, which also reveals the difference between these two mechanisms. Fig. 2.36 summarizes the relationship between resistance in low temperature (2K) and corresponding dose applied in each EBI scan.

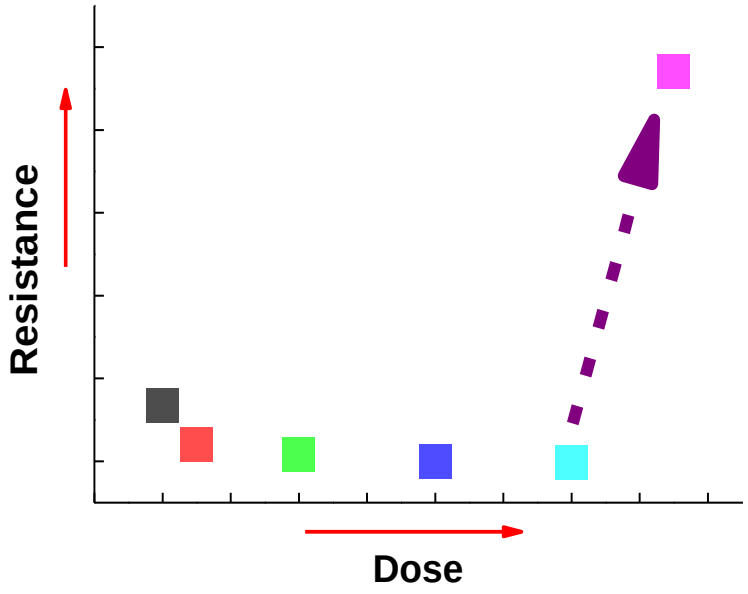

Fig. 2.36 Resistance at 2K vs. dose of each EBI scan.

Hence, our e-beam irradiation experiment results suggest two competing mechanism coexisting in the system. When small dosage of disorder is introduced, the electron carrier density is increased. Upon irradiation, the resistance of n-type device drops with a constant value and then approaches a saturation value (near 1000 Ω in Fig. 2.35) after first several EBIs. The EBI induced effect on carrier density is similar to the observation in Peng's work on the p-type Bi_2Se_3 devices. The second mechanism takes place after the carrier density saturation as more disorders are introduced in the system. More electrons or defects introduced work as disorder to localize the bulk carriers, leading to the reduced bulk conduction contribution and increased resistance in low temperatures. The observed truly insulating bulk states is an expected consequence of disorder induced topological transition.

It is also noticed that the EBI induced disorder is a reversible process. If the device after EBI scan is not put into the cryogenic system but stays at room temperature, it will go back to the previous state. The disorder induced insulating behavior relaxes and becomes less insulating in low temperature. The possible mechanism of each situation during EBI process is shown in Fig. 2.37. A careful dose control and avoidance of localization relaxation should be taken into consideration for successful observation of surface contribution enhancement.

In section 2.2.2, we have shown the weak anti-localization effect observed in BSTS device is originated from the TI surface states by angle dependent magneto-resistance experiment. Fig. 2.37 exhibits the WAL data obtained after different EBI scans. With the increase of EBI dose, the cusp-like WAL phenomenon with surface origin is enhanced.

This indicates the topological surface state is robust against the non-magnetic disorder from irradiation, and more importantly the reinforcement of surface-related transport signal is a

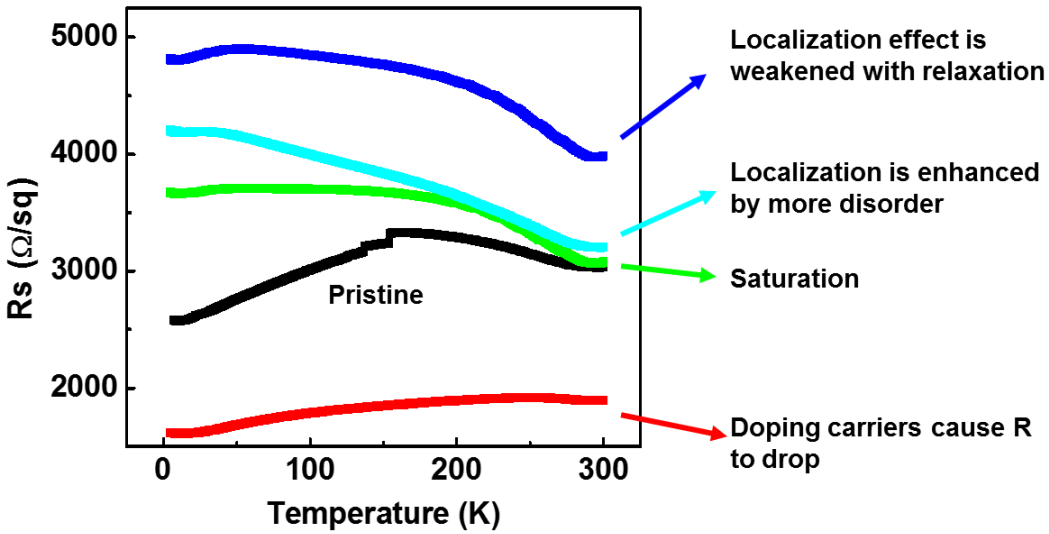

Fig. 2.37 Summary of different states and corresponding mechanisms after continuous EBI scan.

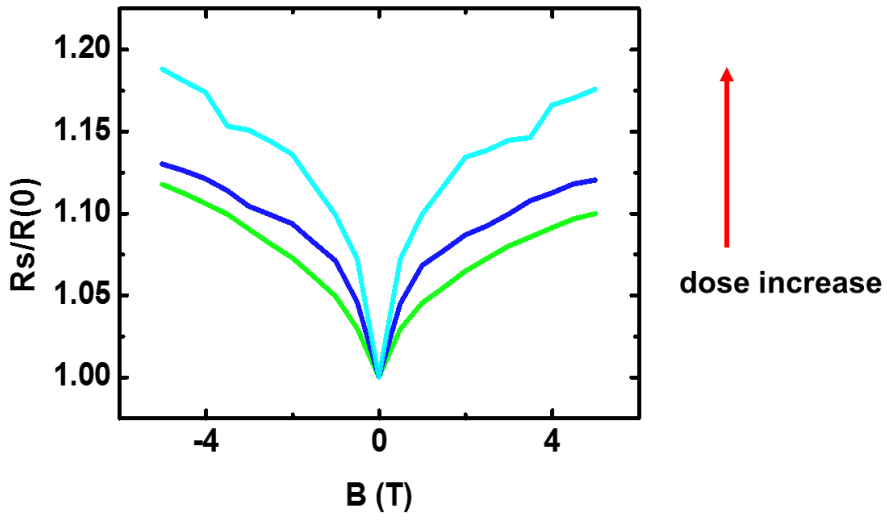

Fig. 2.37 Field dependent MR after different doses.

direct evidence of disorder-driven insulating bulk states in topological insulator device.

We also check the surface transport property by gate dependence as shown in Fig. 2.38. The sample is one BSTS device which originally has metallic resistivity behavior in low temperature (upper panel, black curve). After several EBI scan, the bulk carriers in the device are gradually localized and the metallic temperature dependence has been replaced by the insulator behavior of resistance. The low temperature resistance increases twice after irradiation. The sample has a back gate of 300 nm SiO_2 with a relative dielectric constant of 3.9. By applying the gate voltage on the back side, we can investigate the surface electrical property when Fermi level moves towards the Dirac point under a continuous varying electric field. The lower panel of Fig. 2.38 displays the V_g dependence of R_{xx} for different EBI doses. Clearly, the initial EBIs or pristine states have a very weak electric field dependence, indicating the large amount of bulk carriers in the device. After strong EBI disorder is introduced, the resistance exhibits an obvious increase as the gate voltage sweeps. This occurs since the disorder localizes the electron carriers from bulk conduction channel and Fermi level shifts to charge neutral point as well. With more EBIs, the gate response becomes stronger, which is another direct observation of enhanced surface transport by disorder in TI device.

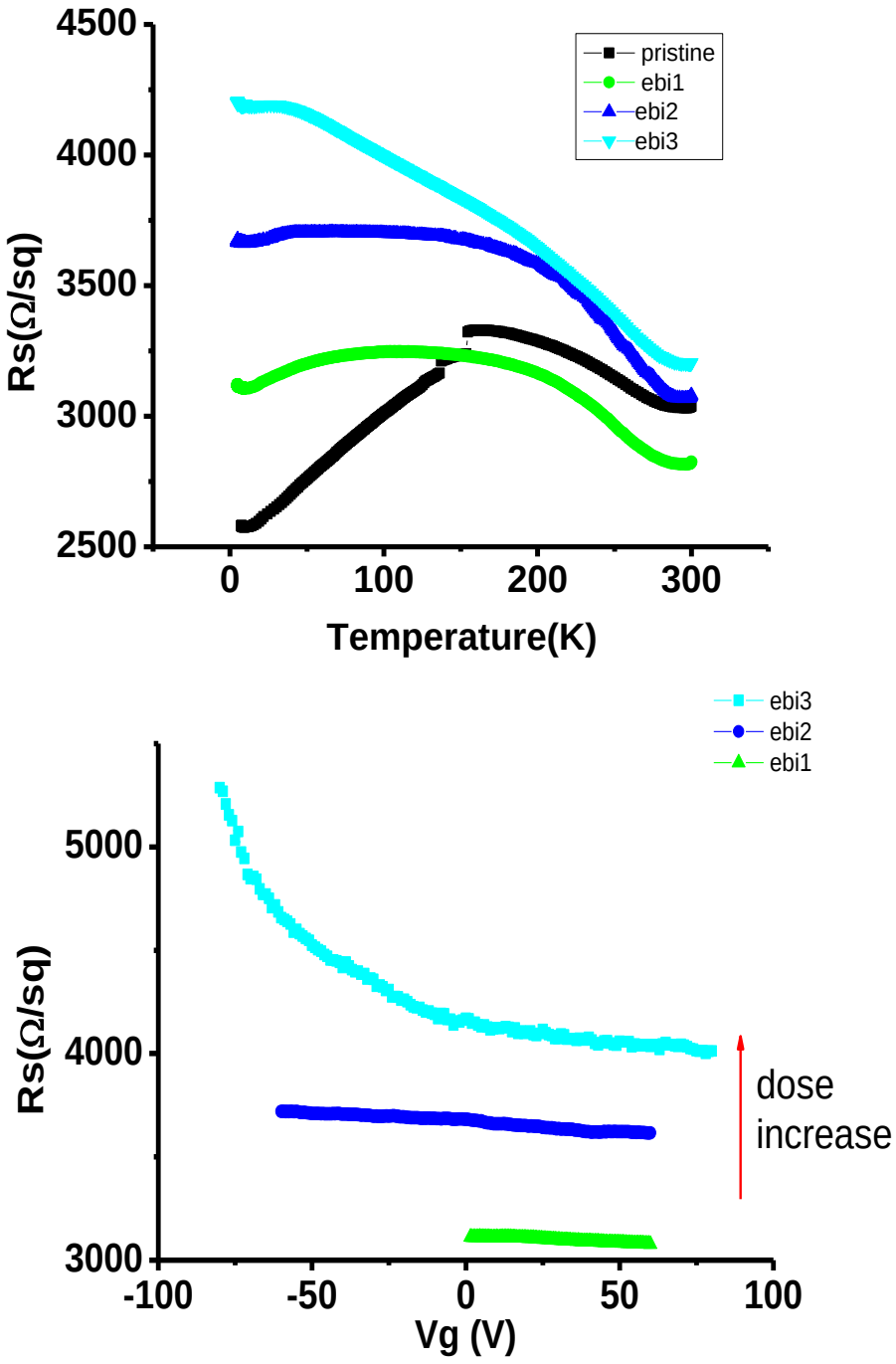

Fig. 2.38 Upper panel: temperature dependent resistance after each EBI scan for one BSTS device. Lower panel: corresponding gate dependence for each EBI at low temperature.

2.3 Conclusion

In this chapter, we review our progress on topological insulator crystal growth, bulk sample calibration and measurement, nano-device fabrication, electrical transport experiment on TI nanodevices, and topological Anderson insulator realized by EBI induced disorder.

We have grown the topological insulator compound $Bi_{2-x}Sb_xTe_{3-y}Se_y$ (BSTS) of high crystalline quality, determined the bulk flake thickness by the FTIR technique, and studied the electrical transport properties in the van der Pauw geometry. The low-temperature bulk resistivity of BSTS sample was near 5 Ω·cm, much higher than most discovered topological insulator materials. The bulk samples also presented a highly insulating behavior as temperature was varied. We analyzed the temperature dependent resistivity curve in different regimes: activated temperature range, 3D VRH region and saturation metallic components. The measured resistivity curve was consistent with the proposed models and the saturation of conductivity at low temperatures implied the existence of a parallel conduction of surface states. Last, from thickness dependent resistivity curve, we have also done an estimation on the fraction of surface contribution in BSTS bulk sample.

Next, we briefly introduced the nano-fabrication process of TI devices. The electrical transport results of BSTS nanodevices in the pristine state have been discussed. However, the resistivity did not keep an insulating behavior as the bulk sample. It showed a metallic temperature dependence with relative low resistance in nanodevices instead, which was considered as a consequence of unintentional defect doping during the

fabrication. We also investigated the field dependent magnetoresistance in low temperatures. The cusp-like weak anti-localization indicated the presence of strong spin-orbit coupling. To reveal the origin of WAL, the angle dependent MR experiment was performed. All MR curves of different angles coincided with each other at low magnetic fields when resistance was plotted as a function of $B\cos\theta$, the normal component of magnetic field. The angular dependent MR data confirmed the 2D nature of WAL observed, suggesting this effect came from the topological protected 2D surface states. SdH oscillation of magneto-resistance in large magnetic field was also studied to estimate the surface mobility, surface carrier density and Landau level index.

In the last part of this chapter, we have studied the surface contribution in TI nanodevices by disorder induced topological transition (topological Anderson insulator). We designed the e-beam irradiation experiment to systematically add the disorder into TI system. We found as the disorder strength increased (monitored by the doses of electron beam), the bulk carriers was localized revealed by the temperature dependent resistivity changing from metallic to insulating behavior. We also investigated the different device states and mechanisms when various disorder strengths were introduced. Moreover, the enhancement of weak anti-localization and gate voltage response also strongly supported the hypothesis that the surface contribution was increased with an insulating bulk states due to disorder. Therefore, topological Anderson insulator would be an ideal technique to study the surface states phenomenon even in an original trivial topological device.

Chapter 3 Interface Magnetism Study in Topological Insulator-YIG Heterostructures

The historic discovery of topological insulator materials begun in 2006 makes the search for a FM insulator with non-zero Chern number, called the quantum anomalous Hall (QAH) insulator become practical. Through careful sample optimization and investigation, the QAHE has been experimentally realized in Cr-doped[43] and V-doped[56] TI system independently. In this chapter, we will review our initial and pioneering effort on exploring the proximity induced ferromagnetism in topological surface states by coupling a TI with magnetic insulator (MI).

This chapter is organized as following: In section 3.1, we will briefly review the theoretical prediction and experimental discovery of QAHE. We will give a detailed statement for the advantage and uniqueness of TI-MI heterostructure in magnetic topological insulator research. In section 3.2, we will discuss the development of heterostructure growth: the deposition of YIG films in pulsed laser deposition system and growth of TI films on top in molecular beam epitaxy chamber afterwards. Standard thin film material characterization techniques have been applied to confirm the highly crystalline quality of TI-MI heterostructure and smooth interface, which is believed to be important for observing the ferromagnetism from proximity effect. Next in section 3.3, we will present the transport study of 20 QL TI film grown on YIG (110). Both the Hall data and WAL signal analysis indicate the additional magnetic scattering on the topological surface states owing to the contact with YIG layer. A control sample of 20 QL TI on Si is also made to show the contrast with the TI-YIG magnetic heterojunction. Last in section 3.4, a more clear picture will be presented when only 5 QL tunable TI film is put on the

surface of YIG (111) substrate. The electrical properties and ferromagnetism like anomalous Hall effect (AHE) is systematically studied as the Fermi level is tuned by varying Bi fraction in $(Bi_xSb_{1-x})_2Te_3$-YIG devices. The preliminary result of EuS-TI-YIG trilayer structure will also be discussed in this section. Our complete investigation of TI-MI heterostructure concludes that the topological surface states could feel the exchange coupling induced symmetry breaking when directly in contact with magnetic insulator material.

3.1 Quantum Anomalous Hall Effect

Breaking time reversal symmetry (TRS) of a TI through either magnetic doping or magnetic overlayer can open up a mini-gap of the Dirac surface states (Fig. 3.1) and lead to many exotic phenomena, such as QAHE, topological magnetoelectric effects and image magnetic monopole. The spontaneously broken TRS states could be experimentally introduced into a material by ferromagnetic ordering. This is usually now achieved by two main methods: (1) conventionally by doping with some magnetic element (Fe, Mn, Cr, V), like diluted magnetic semiconductor (DMS) and (2) by ferromagnetic proximity effect (the direct Heisenberg exchange coupling). In both cases, it is expected that an exchange gap opens up in the Dirac surface states. In this section, we will discuss the mechanism of two methods first, followed by related experiment findings.

Theoretically, Yu et al. proposed[40] that ferromagnetic order in TI can be induced by van Vleck mechanism, which is a second order perturbation effect. In other words, the ferromagnetic order in TI surface can be realized in an insulating state without mediating via free carriers as the Ruderman-Kittle-Kasuya-Yosida (RKKY) case. In their article, it is

claimed that when the thickness of magnetic TI is reduced into a 2D hybridization regime, the QAHE can be realized as long as the hybridization gap is smaller than the ferromagnetic exchange energy.

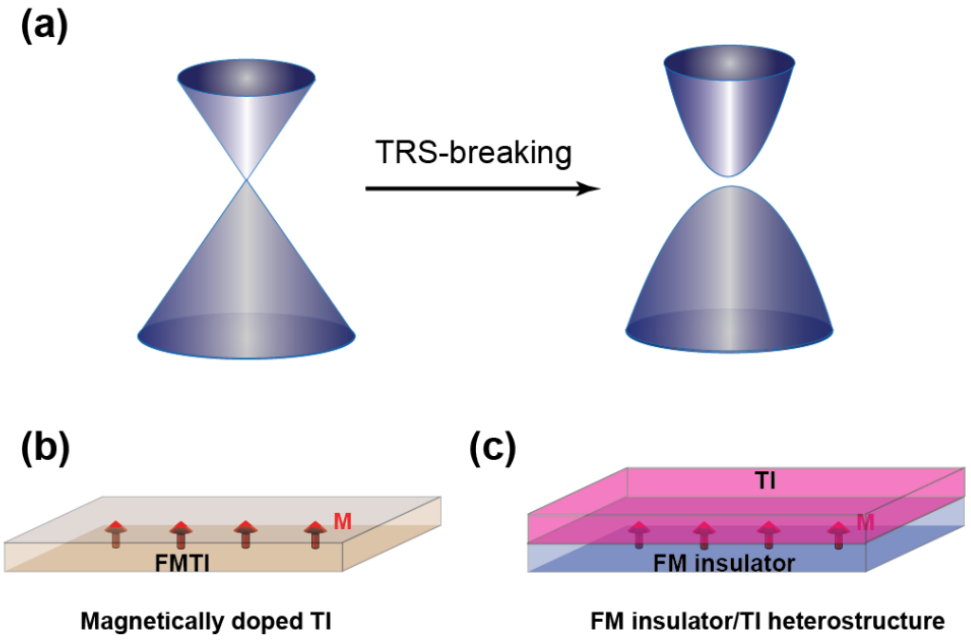

Fig. 3.1 Time reversal symmetry breaking of topological surface states. Adapted from ref 57.

QAHE in TI/ferromagnetic insulator heterostructure was proposed by Qi et al. even earlier[58]. As shown in Fig. 3.2, in a MI/TI/MI sandwiched heterostructure, the parallel magnetization between the two FM insulator layers can lead to a quantized Hall conductance, which vanishes when the magnetization becomes antiparallel. The QAHE here has the same chiral edge states as the QHE. However, all the known FM insulators (e.g. YIG, EuS, GdN, and EuO) have the in-plane easy magnetization anisotropy, hindering the observation of QAHE in the trilayer structure. Although Liu et al. pointed out[59] the

QAHE can be still induced by in-plane magnetization, less evidence has been found till now.

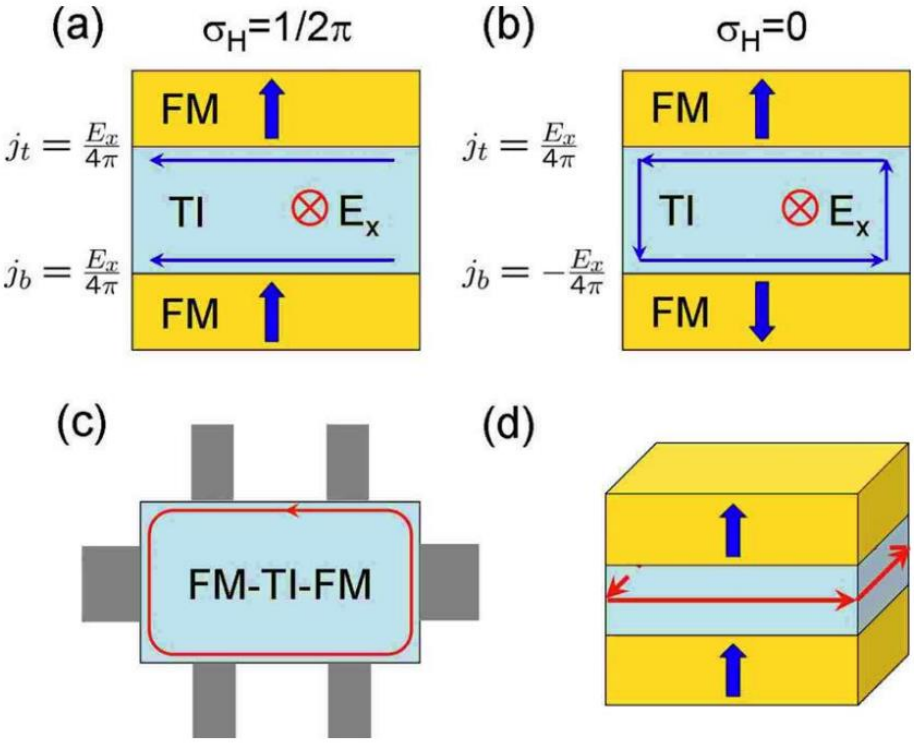

Fig. 3.2 The proposed QAHE in FM-TI-FM heterostructure. Adapted from ref 58.

After settling a complex optimization of the growth of thin films, Chang et al. reported the observation of quantum anomalous Hall effect in 5 QL Cr-doped $(Bi_xSb_{1-x})_2Te_3$ sample for the first time. Ultralow temperature (~30 mK) yields exactly quantized Hall resistance shown in Fig. 3.3. The shape and coercivity of the hysteresis loops are nearly independent of V_g, suggesting a carrier independent FM order. At the saturated magnetization state, Hall resistance is nearly independent of the magnetic field, implying a uniform ferromagnetic order and charge neutrality of the sample, whereas the AH

resistance is changed dramatically with V_g, with a maximum value of h/e^2. The corresponding MR curve exhibits the typical hysteretic shape as in FM metals. Note, the nonzero $R_{xx}(0)$ can be attributed to residual dissipative channels, which is expected to vanish completely at zero temperature or strong magnetic field.

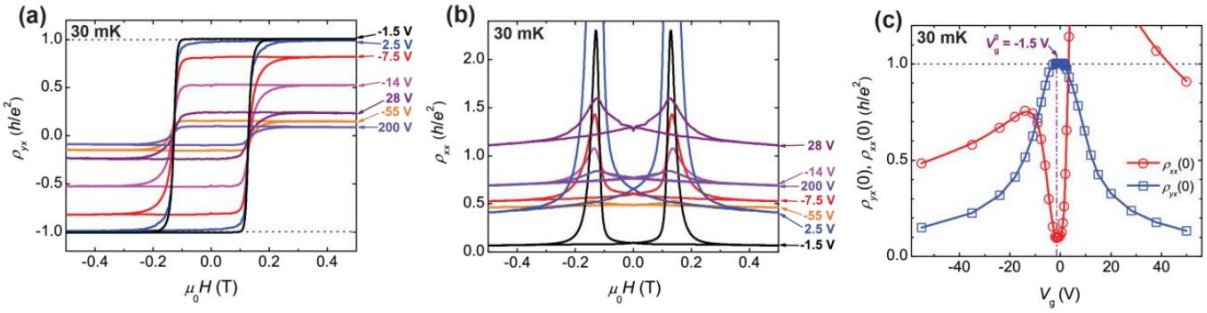

Fig. 3.3 First observation of QAHE in TI at 30 mK. Adapted from ref 43.

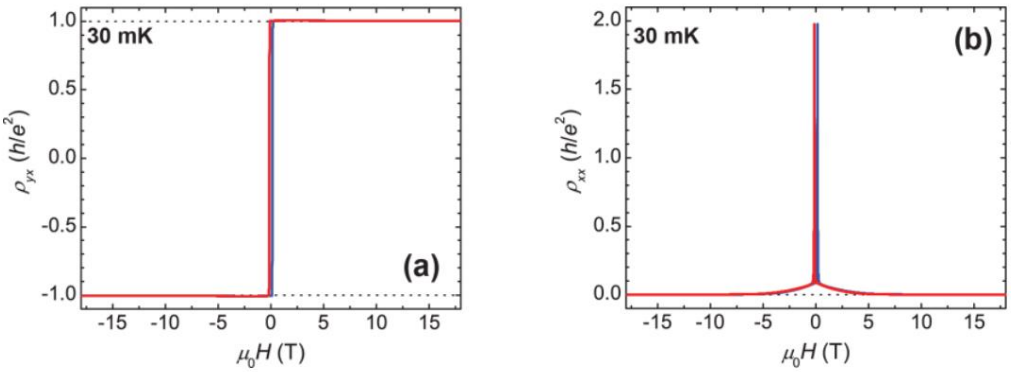

Fig. 3.4 QAHE at higher magnetic field. Adapted from ref 43.

`Fig. 3.4 displays their results after strong magnetic field is applied. The Hall resistance reaches the exact quantized value without fluctuation in high magnetic field, meanwhile the R_{xx} vanishes completely corresponding to a perfect QH state, indicating that all dissipative channels in the sample have been localized.

The QAHE has been reported by various groups in recent two years[44,45,56,60,61] and attract huge experimental interest in the realization of precise QAHE phenomena, increasing the occurance temperature and exploring the more potential candiate materials.

Considering current achievements and challenges in QAHE research, a heterostructure consisting of a 3D TI and MI is of great interest. Several phenomena, predicted for broken TRS TIs, exist only at the interface. For example, one of the excellent properties by coupling the MI to a superconducting TI layer is that the local exchange field experienced by the TI is able to lift spin degeneracy without destroying the superconducting pairing, in complete contrast to magnetic impurity doping. This opens up new possibility for functional ferromagnetic superconducting TI device. More importantly, choosing a magnetic insulator with high Curie temperature like YIG (~550 K), EuS (~16.5 K) or EuO (~77K) coupled with TI film will be obviously advantageous for realizing the QAHE at high temperatures.

Peng et al. demonstrated the proximity induced interface magnetism in EuS/Bi_2Se_3[62]. They successfully observed the hysteresis-like magnetoresistance with in-plane magnetic field. The hysteretic MR shape and ferromagnetic coercive field are independent of the angle between the applied in-plane field and electric current. This

unconventional behavior is attributed to the isotropic distribution of domains and hence the observed isotropic planar MR. A few independent studies on various TI/MI heterostructures have been reported in recent years[63-67]. However, the relationship between proximity induced ferromagnetism and electrical transport properties of surface states is still unclear due to strong bulk conduction of metallic TI samples (Bi_2Se_3 or Bi_2Te_3) used in the heterostructure research.

Last but not least, two challenging issues in the proximity approach should be mentioned. First, interfacial control of the TI/MI system requires that they are not only closely interacting magnetically, also maintains a contamination free interface. This "ideal" interface condition asks for a lot of delicate efforts on calibrating the growth recipe, surface treatment and annealing procedure, especially for the heterostructure grown in two separate chambers. Second, strong perpendicular magnetic anisotropy (PMA) materials should be preferred for QAHE in TI/MI heterostructure, although canted magnetization of current MI has been reported. A recent finding of Tm-IG with strong PMA can be taken into consideration to form the quantum anomalous Hall insulator with TI.

3.2 Growth and Characterization of YIG-TI Heterostructures.

3.2.1 Pulsed Laser Deposition

Pulsed laser deposition (PLD) is a well-known excellent physical vapor deposition technique for oxide film growth. In a PLD system (in Fig. 3.5), a high power pulsed laser beam is focused by a set of optical components into a vacuum chamber and strikes the target material. The target material is then vaporized as a plasma plume and deposited on the substrate to form thin film. The substrate is equipped with a backside heater used to

adjust the temperature during the growth or for annealing. Depending on the material grown, the chamber can be in the ultra-high vacuum (UHV) state or in the presence of background gas. The schematics of PLD system is shown in Fig. 3.5 and the real image of our home-built PLD chamber is shown in Fig. 3.6. Note, a reflection high-energy electron diffraction (RHEED) system is installed to monitor the real time growth crystal pattern and

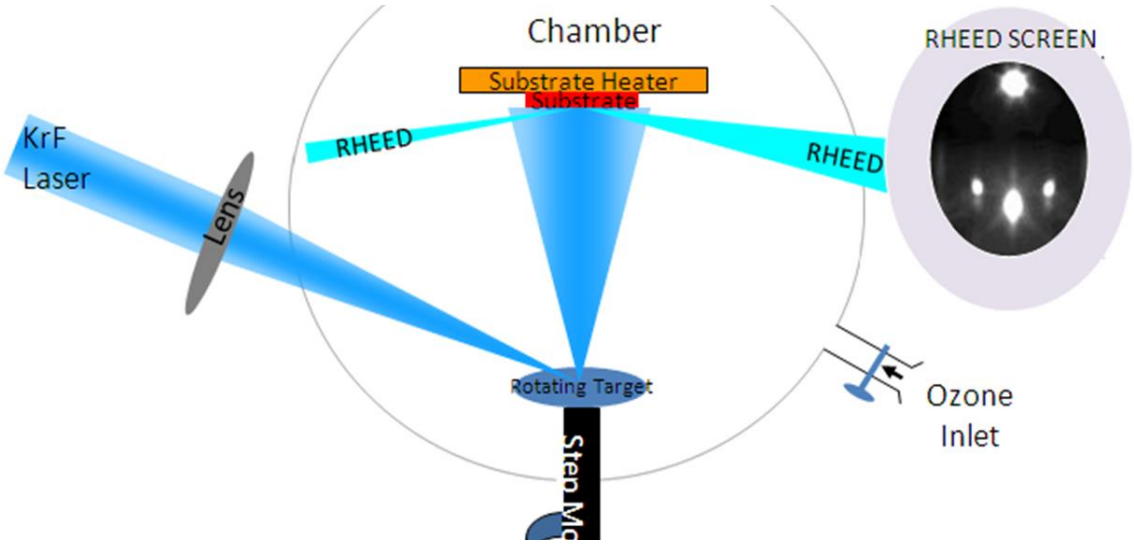

Fig. 3.5 Schematics of PLD system.

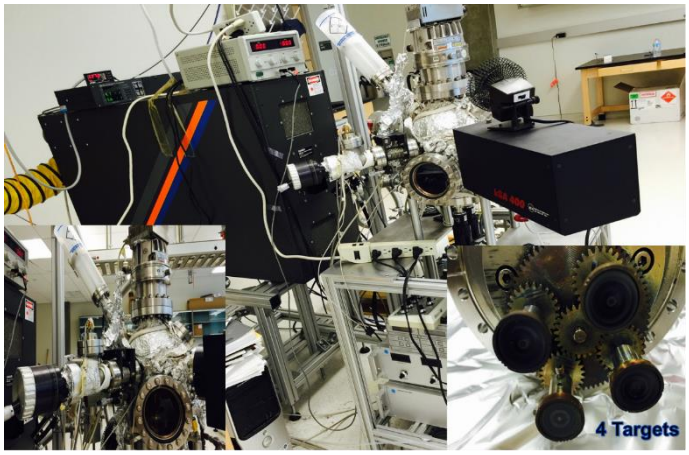

Fig. 3.6 Real image of home-built PLD set-up.

As shown in Fig. 3.6, our home-built PLD system has ozone capability which provides the backfilled rich oxygen background for complex oxide material growth. The UHV chamber with four rotating target could reach a base pressure up to 1×10^{-7} Torr. A KrF excimer laser (Coherent COMPexPro 102F) with 248 nm wavelength is used as the laser source. The laser pulse length is 10-50 ns, the maximum pulse power is 200 mJ per pulse and the maximum repetition rate is 20 Hz.

3.2.2 YIG Film Growth

Yttrium iron garnet ($Y_3Fe_5O_{12}$, YIG) is a ferrimagnetic insulator material with a high T_C~550 K. A ferrimagnetic material has atoms with opposing spin orientations but with a net spin in each unit cell below the T_C. Fig. 3.7 is a unit cell of YIG crystal, which could be written as $(Y_3Fe_2Fe_3O_{12})_8$. The five Fe atoms belongs to two different sites: octahedral sits of 2 iron atoms and tetrahedral site of 3 iron atoms respectively. In YIG, the Fe^{3+} ions on two sites are antiferromagnetically coupled to each other due to super-exchange interaction, resulting in a ferrimagnetic state with net magnetic moment equivalent to one Fe^{3+} per formula unit.

YIG is widely used in spintronics research recently owing to following advantageous properties: (1) the bulk crystal has a very small intrinsic damping constant about 3×10^{-5}, which is important in spin-torque and spin-wave based devices[68]; (2) it is an electrical insulating material but can transmit pure spin currents without Joule heating associated with charge current in spintronics devices. The recent works of spin Seebeck effect, magnetic proximity effect, spin Hall magnetoresistance and spin pumping based on

YIG heterostructure show the great importance of a magnetic insulator material with T_C above room temperature.

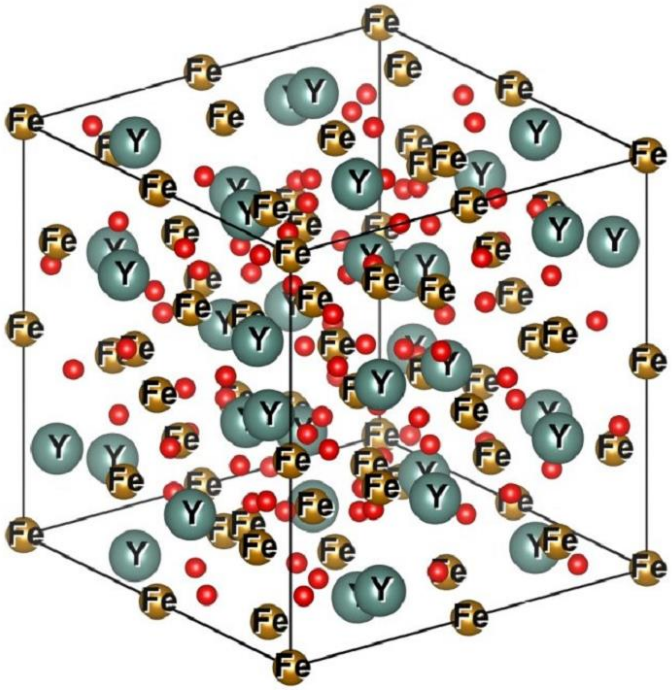

Fig. 3.7 Schematics of YIG crystal unit cell.

The commercial (110)- and (111)-oriented GGG (gadolinium gallium garnet) substrates from MTI corporation are used for epitaxial YIG film growth, since the lattice match between YIG (12.376 Å) and GGG (12.383 Å) is almost perfect (lattice mismatch~5×10^{-4}) for epitaxial growth. The GGG substrate is first cleaned by acetone, IPA and de-ion water for half an hour each, and then loaded into a furnace with oxygen flow for annealing. The annealing temperature is 1000 ℃ and duration is 6 hours, which helps increase the uniformity of substrate surface. Prior to growth, the substrate is baked in the PLD chamber overnight at around 200 ℃ with the base pressure of 1×10^{-7} Torr. This

substrate treatment procedure before the growth is carefully developed to ensure excellent surface condition and epitaxial growth environment.

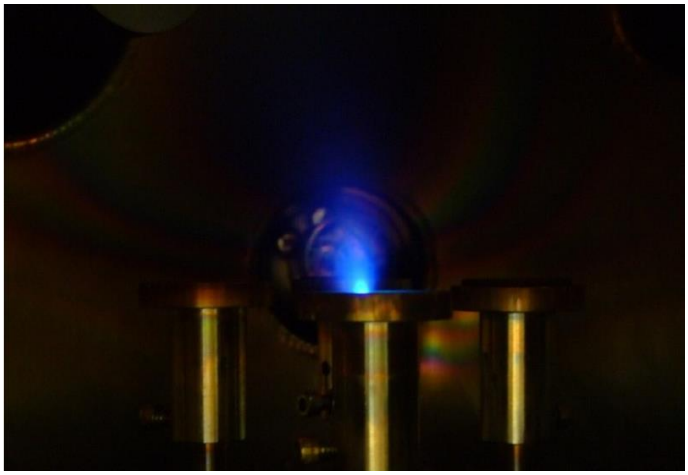

Fig. 3.8 Plasma plume generated by the bombardment of YIG target during the deposition.

During the deposition, the substrate is heated to 650 ℃ to 750 ℃. We also try lower growth temperatures or even room temperature growth of YIG films, however, the films tend to be unmagnetized or have much smaller magnetization measured with VSM. The chamber is filled with ambient oxygen pressure of 2.2×10^{-3} Torr with ozone flow. The power of KrF lase is set around 150-160 mJ with the repetition rate of 1 Hz. Large repetition rate is found to increase the surface roughness of YIG film although the growth is faster. The Fig. 3.8 is the plasma plume released by the bombardment on YIG target by pulsed laser. The clear diffraction pattern appears throughout the growth, accompanied by the intensity oscillation monitoring the layer by layer growth mode (see detail below). After the growth, the sample is cooled down slowly to room temperature while keeping the oxygen pressure to avoid off stoichiometry. After venting the chamber, the sample is taken out and cleaned again following similar procedure as of GGG substrate. The post-annealing

process is performed in a separate furnace with rich oxygen flow at 850 ℃, which is found to be good for making the surface more smooth and enhancing the magnetization.

The layer by layer growth mode is achieved under a certain condition in substrate treatment and growth parameter. RHEED pattern as displayed in Fig. 3.10 is taken before and after the YIG (110) growth. The crystal structure is consistent during the deposition, strongly suggesting the epitaxial growth of YIG film on GGG (110) substrate. Meanwhile, the layer by layer growth mode is monitored by the RHEED intensity oscillation, as shown in FIG. 3.9. Each oscillation peak corresponds to the formation of one mono-layer, which is equal to ¼ of the unit cell length. With the help of RHEED oscillations, we can estimate the thickness of YIG film produced each time. For instance, in a one hundred oscillations case, the layer by layer grown YIG film is 100×sqrt(2)×a/4=44 nm.

YIG (111) is also grown on GGG substrate under the layer by layer growth mode. The RHEED pattern will be shown later when describing the TI/YIG heterostructure property.

With the capability of epitaxial layer by layer growth and atomically flat GGG (110) substrate, it is natural to observe the atomically flat terraces on the surface of YIG (110) film, as an indication of high crystalline quality. The AFM image of a typical YIG (110) film is present in Fig. 3.11. Similar to the calculation above, each mono-layer corresponds to ¼ of unit cell face diagonal length, resulting in the height of each mono-layer of 4.4 Å. The step height at the edge of the terrace is measured by AFM and the result agrees well with the calculated mono-layer thickness. The root-mean-square (rms) roughness of YIG

(110) is 0.6 Å, implying extremely smooth surface which makes the YIG an ideal component forming the heterojunction with TI.

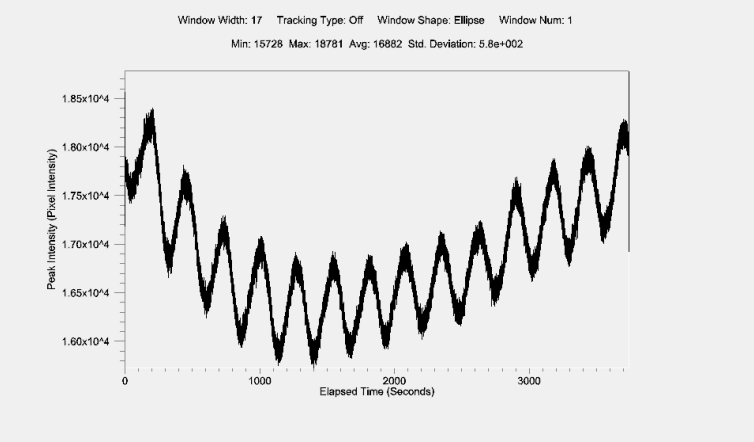

Fig. 3.9 RHEED intensity oscillation of layer by layer growth of YIG film.

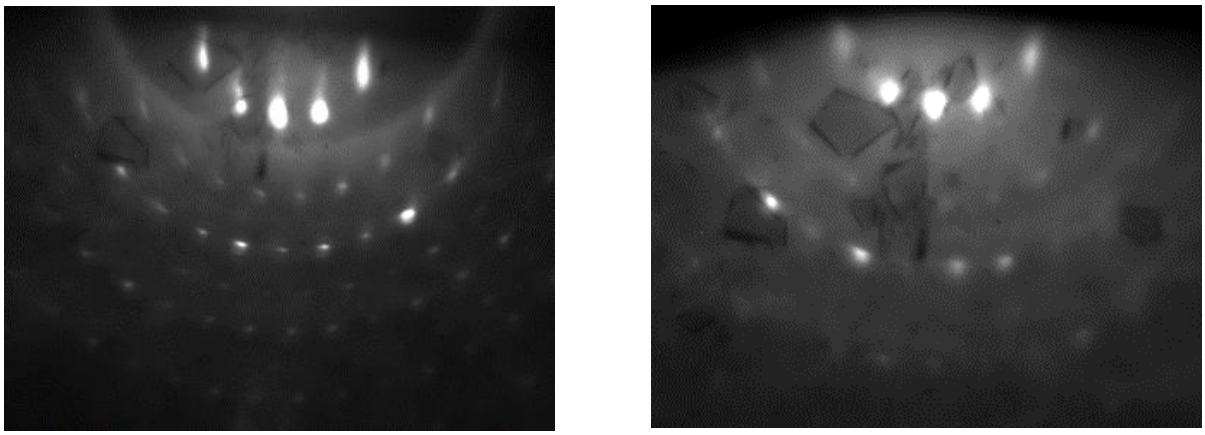

Fig. 3.10 RHEED pattern before YIG growth (left) and after YIG growth (right).

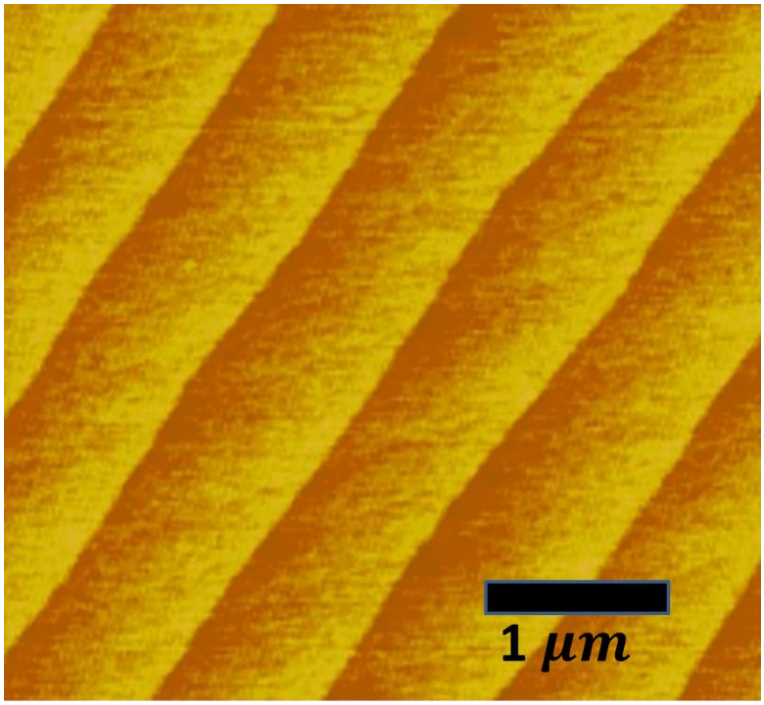

Fig. 3.11 AFM image of YIG (110) surface with atomic terraces.

The magnetic property of YIG (110) film is measured by vibrating sample magnetometer (VSM) at room temperature. Both in-plane and out-of-plane magnetic fields are applied. As shown in Fig. 3.12, the magnetization of YIG film has clear in-plane anisotropy. The out-of-plane saturation field is varying from 2000 to 2500 Oe, which should be mainly determined by the shape anisotropy of YIG sample. The in-plane coercive field of YIG film could vary from less than 1 Oe to 20 Oe. YIG (110) has magnetic uniaxial anisotropy in the film plane (see Fig. 3.13).

YIG (111) film magnetic property is also checked by VSM under same environment. The magnetic property of YIG (111) is similar to that of YIG (110), however

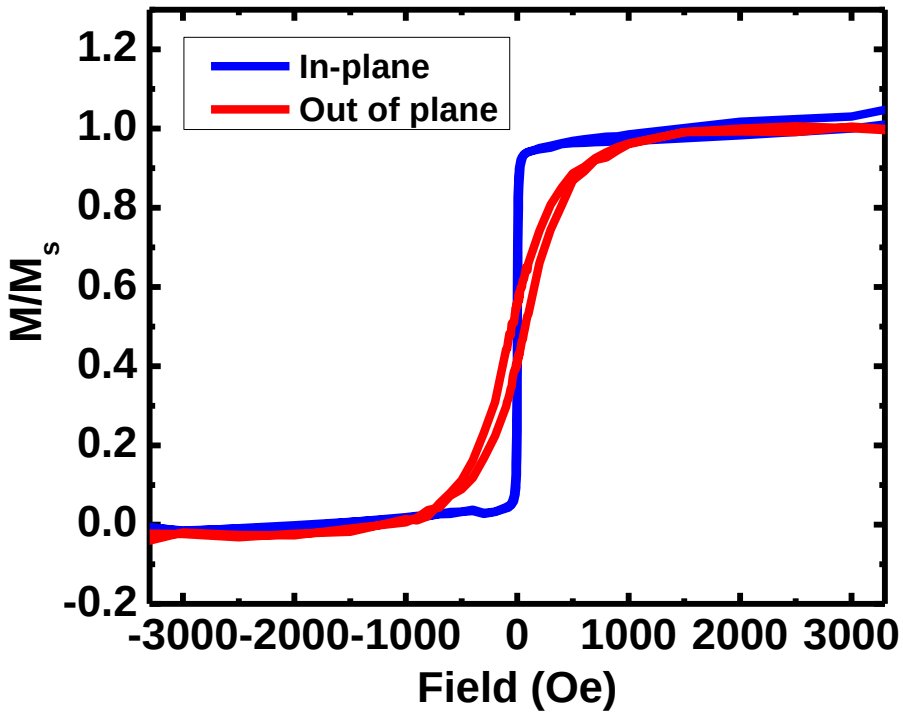

Fig. 3.12 VSM data of YIG (110) film under in-plane and out-of-plane magnetic field.

the only difference is YIG (111) does not have the uniaxial anisotropy in the film plane. As a result, for heterostructure based on YIG (111) film, the spin transport signal magnitude will not rely on the device in-plane orientation, which is beneficial for spin Seebeck experiment.

Ferromagnetic resonance (FMR) linewidth and resonance field characterize the quality of magnetic films which are related to the damping and saturation magnetization M_s. The average FMR linewidth ΔH of our PLD grown YIG films is ~10 Oe and can be as

narrow as ~3.5 Oe. The $4\pi M_s$ obtained from Kittel formula[69] ranges from 2000 to 2500 Oe. These results indicate excellent magnetic properties of our PLD grown YIG films.

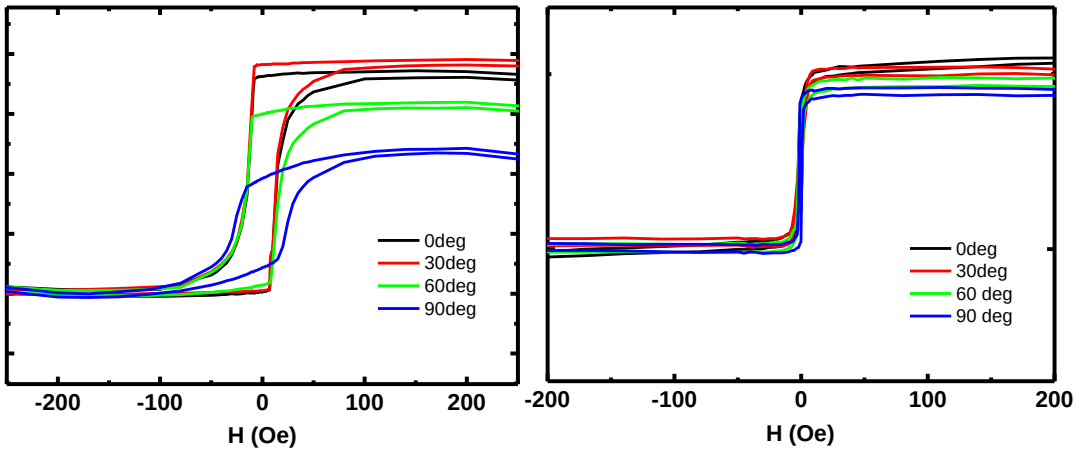

Fig. 3.13 In-plane low field magnetic hysteresis loops for YIG (110) (left panel) and YIG (111) (right panel).

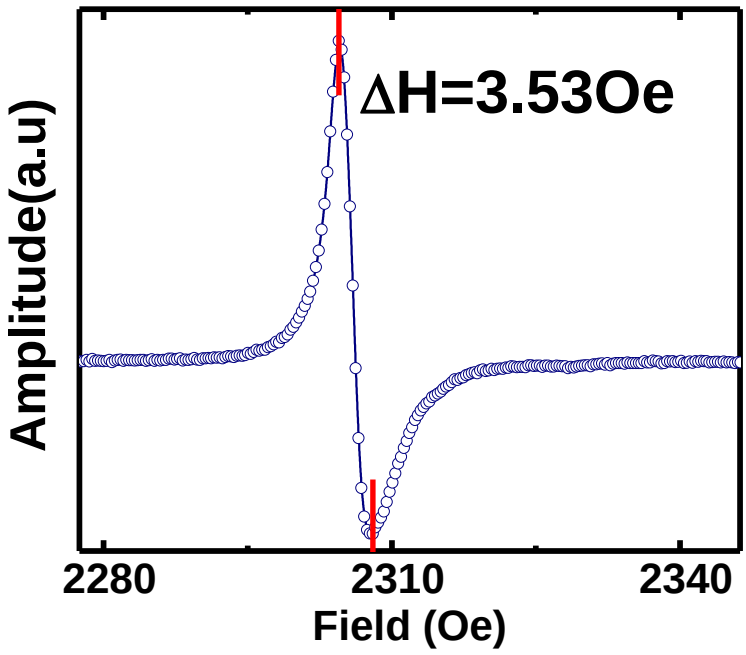

Fig. 3.14 FMR spectrum of YIG on GGG.

3.2.3 Growth of TI Films on YIG Substrates in MBE Chamber

To grow Bi_2Se_3/YIG hybrid structures, the YIG films are transferred to an ultra-high vacuum (low 10^{-10} Torr) molecular beam epitaxy chamber for the Bi_2Se_3 growth. To ensure good interface quality in-situ oxygen plasma cleaning is performed to remove the organic contaminations on the YIG surface before the growth. High-purity (5N) elemental Bi and Se are co-evaporated from different Knudsen-cells with typical growth rates between 0.5 and 1 nm/min, determined by in-situ quartz crystal micro balance. The thickness is confirmed by ex-situ x-ray reflectivity measurements. The temperature of the substrate is kept at 300±5 ℃ for crystalline Bi_2Se_3 growth, i.e., in the epitaxial growth regime with a hexagon-on-cube orientation. After that, a 5nm Al_2O_3 is deposited as a capping layer. Two control samples of 20 QL Bi_2Se_3 capped with Al_2O_3 are grown on Si simultaneously.

To characterize the crystal structure, x-ray diffraction (XRD) is performed with a high resolution x-ray diffractometer using $CuK_{\alpha 1}$ radiation (wavelength λ=1.54056 Å) over a wide diffraction angle range. Combination of different types of scans is performed in order to investigate the crystallographic relationship between substrate and grown layer. Wide range out- of -plane XRD scans reveal that the Bi_2Se_3/YIG thin film consists of a single Bi_2Se_3 phase and a couple of textured YIG phases (Fig. 3.15-a). In the figure, the TI layer shows the (00l) type reflections along the growth direction. The Bragg peak positions of Bi_2Se_3 agree in all samples, which indicate that 20 QL of Bi_2Se_3 films are thick enough to relax back to the bulk lattice structure regardless of the substrates they are grown on.

Fig. 3.15-c shows a reciprocal space map of the k-l cut at the vicinity of (003) Bragg peak of a Bi_2Se_3 (20 QL) /YIG. Strong Kiessig fringes are observed around the diffraction peak,

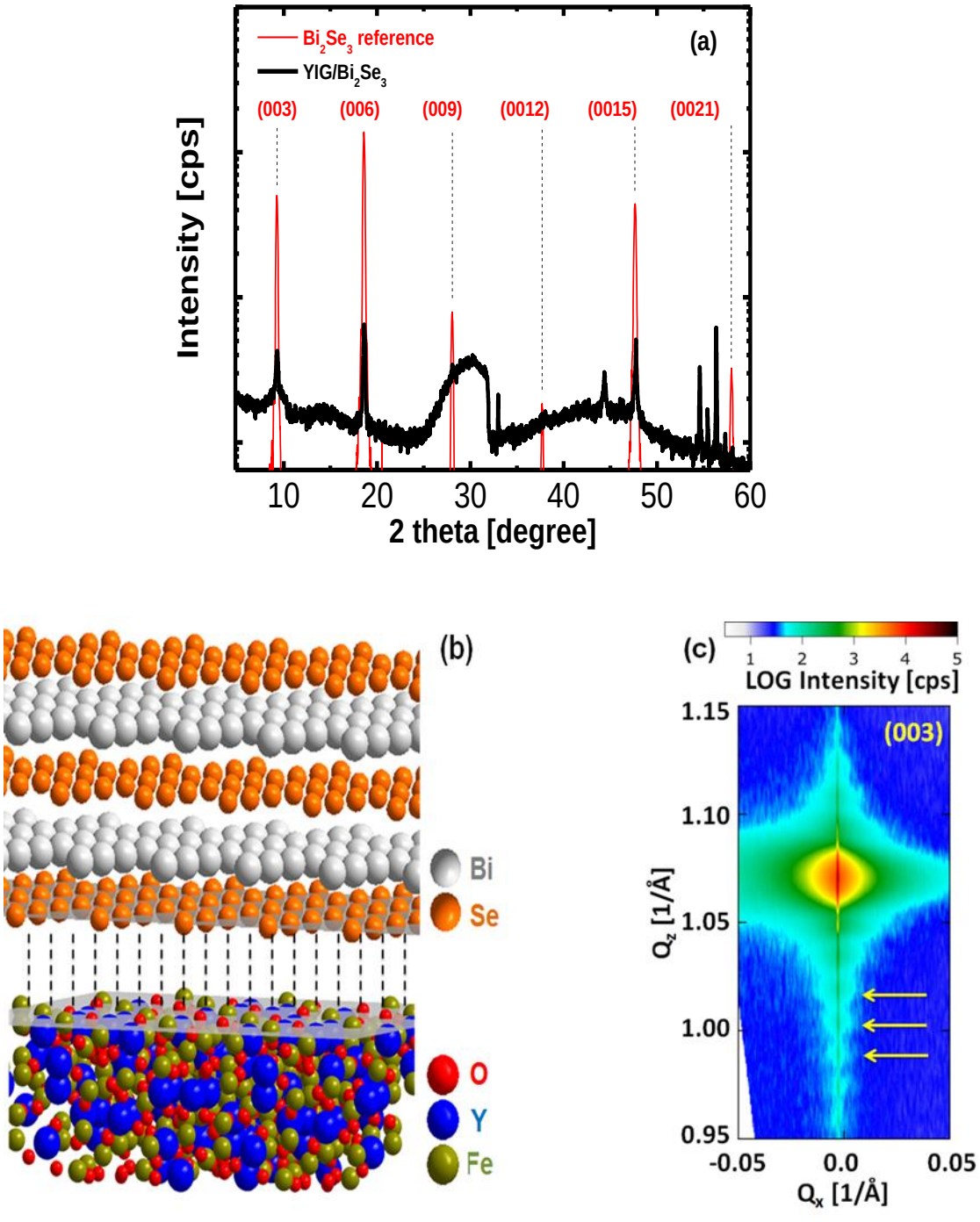

Fig. 3.15 XRD analysis for Bi_2Se_3/YIG heterostructure.

indicating good Bi_2Se_3 surface and Bi_2Se_3/YIG interface correlation and homogeneous growth of Bi_2Se_3. All samples show similar features in XRD mapping, which indicate the excellent structural quality of TI on YIG.

The transport study of 20 QL Bi_2Se_3 on YIG is discussed in section 3.3. However, the results suggest significant contribution from bulk carriers, which could be reduced by constructing thinner TI film on YIG substrate. We have made significant efforts on the development of proper recipe for TI/YIG heterostructure growth and find the YIG (111) orientation is better than (110) to work as the TI growth substrate. It is demonstrated that 5 QL TI film deposited on YIG (111) substrate forms an excellent heterojunction property. In the following part of this section, I will talk about the modified growth recipe and sample characterization.

Thin YIG films are grown on polished single crystal GGG (111) substrates via pulsed laser deposition (PLD). The base pressure of the deposition chamber is ~6×10^{-7} Torr. During the growth, the substrate is heated up to 700 ℃ and the chamber is back filled with ozone (~1.5 mTorr). The layer-by-layer growth mode and film thickness can be monitored and recorded by the reflection high-energy electron diffraction (RHEED) pattern and its intensity oscillations. YIG shows an epitaxial relation with the GGG substrate (Fig. 3.18-a). Atomic force microscopy (AFM) image of a typical ~20 nm YIG film (Fig. 3.16) indicates a rms roughness ~0.1 nm over a 2 μm × 2 μm scanned region. To characterize the magnetic properties of YIG films, the ferromagnetic resonance (FMR) data were taken with 9.6 GHz as shown in Fig. 3.17. The red solid line shows a fit to a Lorentzian function, with FMR resonance field H_{res}~2473 Oe and linewidth ΔH~6.5 Oe.

$4\pi M_s$~2200 Oe can be calculated from the Kittel equation[69]. These results suggest that the YIG films are of high quality[68]. To form TI/MI heterostructures, YIG (111) films are then transferred to a custom-built ultra-high vacuum (< 5×10^{-10} Torr) molecular beam epitaxy system (MBE) for TI growth. To ensure good interface quality, in-situ high temperature annealing (600 ℃, 30 mins) is performed to degas before film growth. Prior to TI growth, the RHEED pattern is taken again to ensure excellent quality of YIG surface (Fig. 3.18-b) after annealing. High-purity Bi (99.999%), Sb (99.9999%), and Te (99.9999%) are evaporated from Knudsen effusion cells. During the growth, the YIG substrate is kept at 230 ℃ and the growth rate is ~0.2 quintuple layer (QL)/min. The epitaxial growth is monitored by the in-situ RHEED pattern. The sharp and streaky diffraction spots indicate a very flat surface and high quality crystalline TI thin film grown on YIG (111) (Fig. 3.18-c). The film is covered with a 5 nm Te protection layer before taken out of the MBE chamber.

We make several modifications in above recipe compared with previous growth procedure of 20 QL Bi_2Se_3/YIG (110) sample. 1, YIG (111) is used as substrate instead of YIG (110), which contributes to the formation of excellent layered structure of TI film on (111)-orientation YIG. 2, We engineer the annealing procedure before the YIG transfer (in an ex-situ furnace with rich oxygen flow) and after YIG transfer (in MBE chamber at high temperature), which shows improving the surface flatness and providing a good interface quality, extremely critical for building up a heterostructure sample. 3, We slightly decrease the growth temperature of TI film. Good RHEED pattern is obtained for most samples,

indicating high crystalline TI film grown under current circumstances. 4, Te film is used as the capping layer instead of Al or Al_2O_3. Te film shares the same crystal structure as the

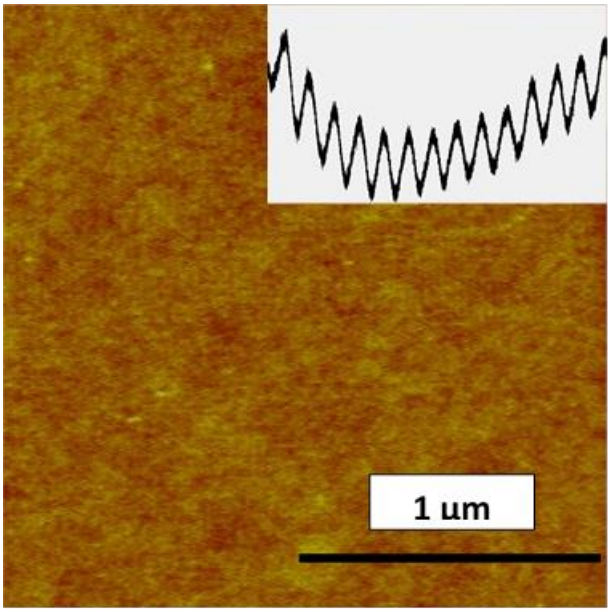

Fig. 3.16 AFM image of YIG (111) with RHEED intensity oscillation.

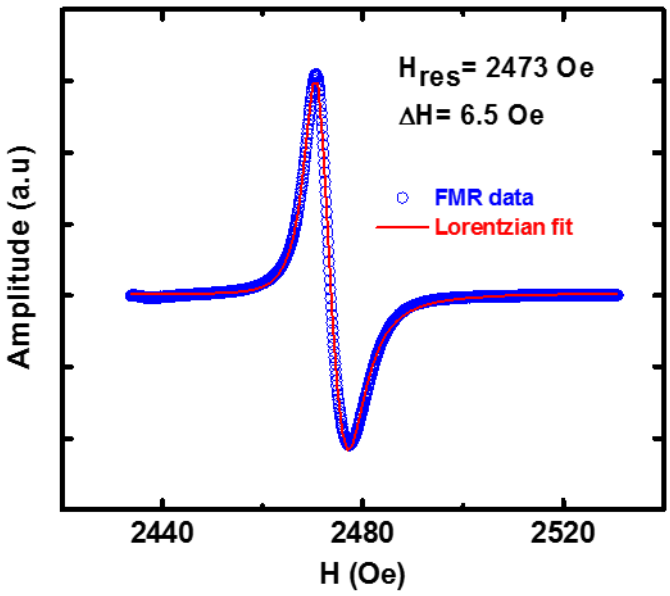

Fig. 3.17 FMR spectrum of a YIG (111) sample.

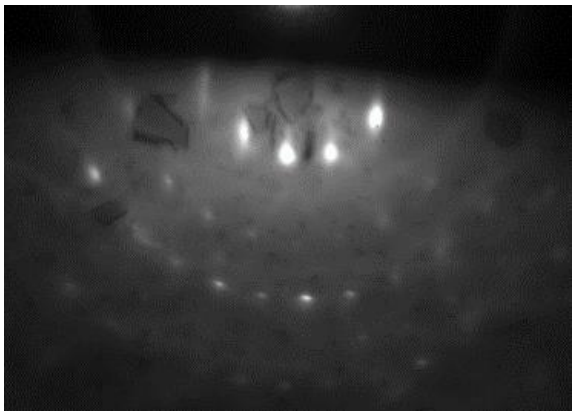

a, YIG (111)/ GGG substrate after deposition in PLD

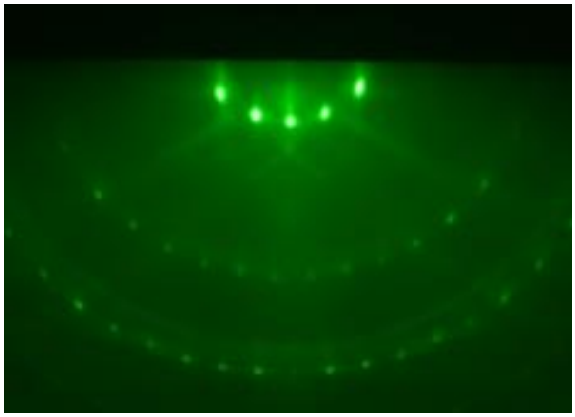

b, YIG (111)/ GGG substrate prior to TI growth in MBE

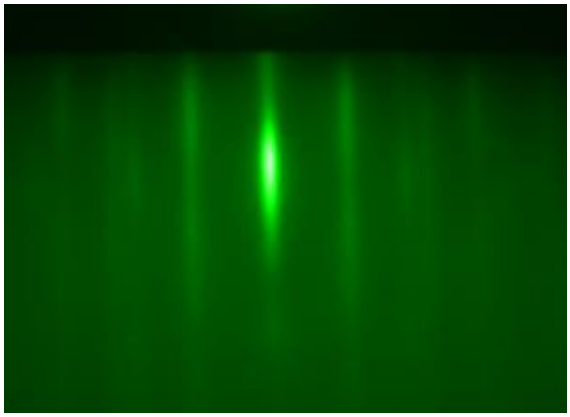

c, 5 QL $(Bi_{0.24}Sb_{0.76})_2Te_3$ grown on YIG

Fig. 3.18 RHEED pattern of YIG (111) substrate and TI film on YIG.

$(Bi_xSb_{1-x})_2Te_3$, therefore it will not damage the top surface of TI film when epitaxially grown on top. Thin Te film is also very resistivity and will not affect the electric transport study of TI film.

High single crystal quality is also confirmed by x-ray diffraction (XRD) on a 20 QL TI on (111)-oriented YIG/GGG, as shown in Fig. 3.19. All peaks can be identified with (00n) diffraction of $(Bi_xSb_{1-x})_2Te_3$, while the YIG/GGG shows the (444) diffraction peak and the (001) peak of the Te capping layer is also present. No other phase is observed in the TI/YIG film according to the XRD data. The zoom-in low-angle XRD scan near the (003)-peak shows multiple Kiessig fringes on both sides, further revealing excellent layered structures of TI films on (111)-oriented YIG and good TI/YIG interface correlation.

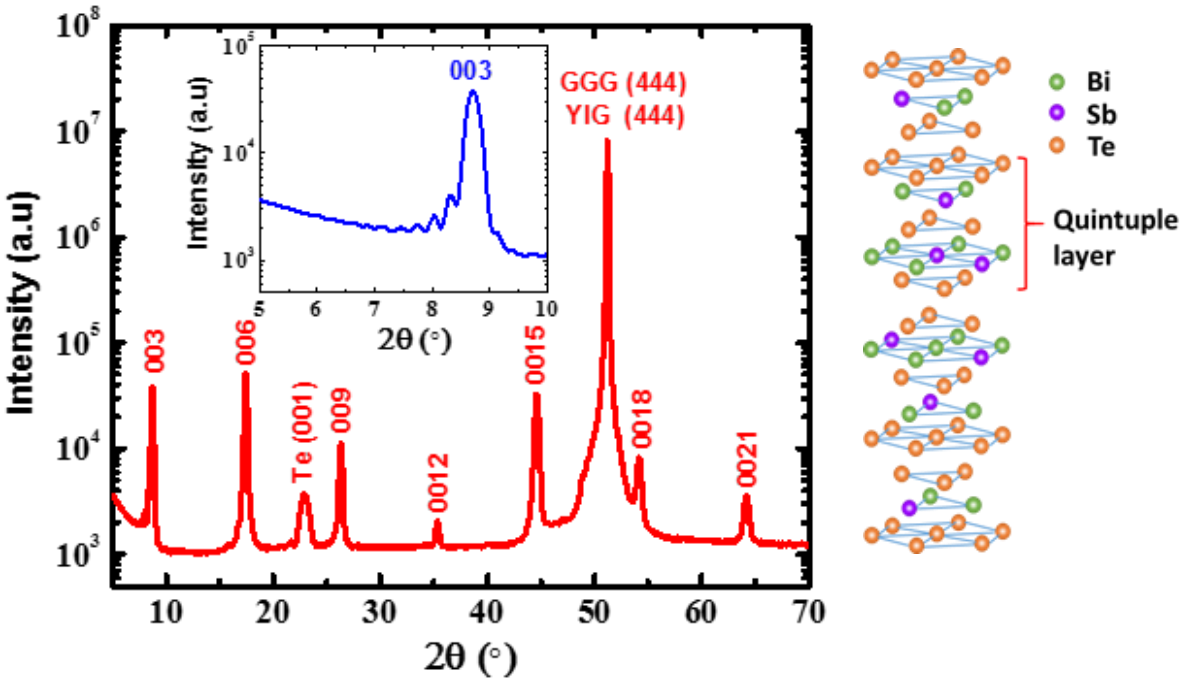

Fig. 3.19 X-ray diffraction result of a typical 20 QL-$(Bi_xSb_{1-x})_2Te_3$ grown on YIG/GGG (111). The inset shows a zoom-in view of the (003) peak and clear Kiessig fringes. Tetradymite-type crystal structure of $(Bi_xSb_{1-x})_2Te_3$ consisting of quintuple layers.

Fig. 3.20 shows a typical cross-sectional high resolution transmission electron microscopy (HRTEM) image of the TI/YIG sample. TEM specimen is prepared by a focus ion beam technique (FEI Quanta 3D FEG dual beam system) and the interface zone between TI film and YIG is brighter because the interface region is slightly thinner than surrounding area due to a higher ion beam etching rate at the interface. This HRTEM image confirms that TIs grown on YIG maintain a good layered structure and that the interface between $(Bi_xSb_{1-x})_2Te_3$ and YIG is atomically clean and sharp. The HRTEM image also supports the conclusions drawn from the XRD experiment, that is, YIG is perfect single crystal with the exactly same orientation as GGG, the TI is grown along the [001] direction on the (111) surface of YIG and the Te protection layer has an epitaxial

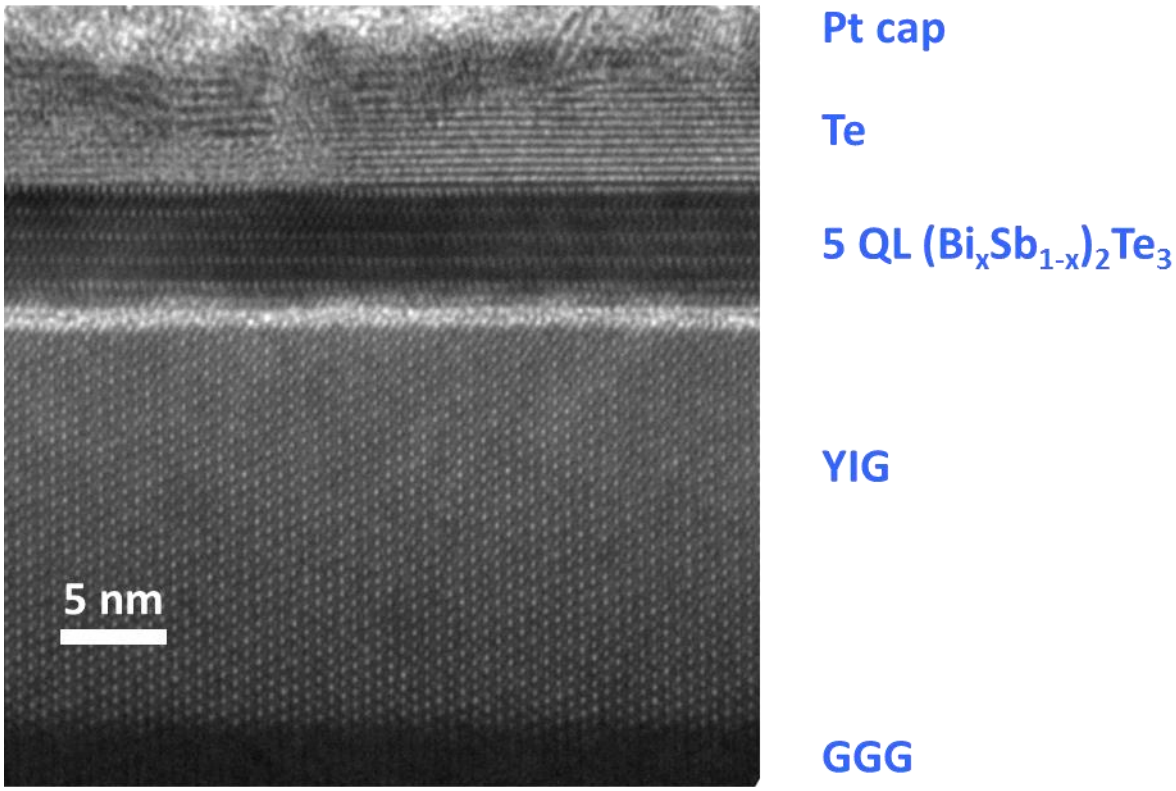

Fig. 3.20 HRTEM image of 5 QL TI/YIG (111) sample.

3.3 Transport Study of 20 QL Bi_2Se_3/YIG sample

A comparative transport study of Bi_2Se_3 and Bi_2Se_3/YIG (110) is performed based on successful construction of TI/MI heterostructure as described previously. For transport measurements, the bilayer samples (Bi_2Se_3/YIG (110)) are patterned into Hall bar structures (channel width of 100 μm and length of 900 um) by standard photolithography and etched by Ar plasma. The Au and Ti contact pads are deposited by an electron beam evaporator. The four terminal transport measurements are taken in a physical property measurement system over the temperature range of 1.9-300 K and in magnetic fields up to 14 T. Fig.

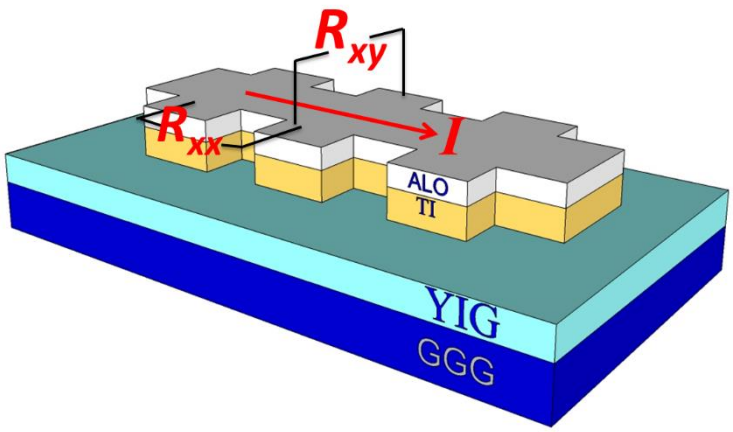

Fig. 3.21 Schematics of device structure of 20 QL Bi_2Se_3/YIG (110).

Fig. 3.22 shows the resistance vs. temperature curves for four samples: three bilayer samples and one control sample. At high temperatures, they all show a metallic behavior, i.e., with positive temperature coefficients. Although they have approximately the same temperature coefficient in resistance, the bilayer samples clearly have larger sheet

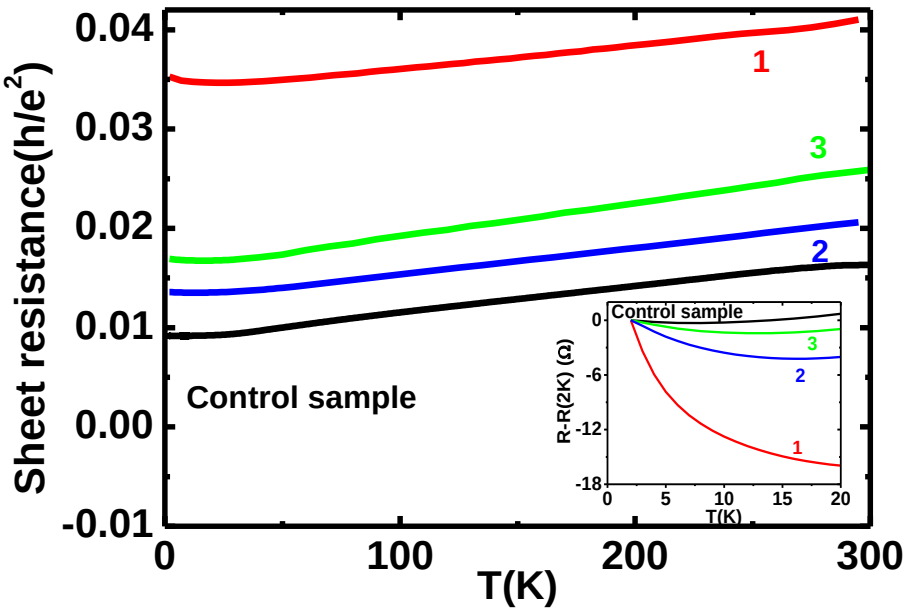

Fig. 3.22 Temperature dependent resistance for one control sample and three bilayer samples.

resistance, or suppressed conductivity compared with the control sample. The resistance of Bi_2Se_3/YIG/Si (sample #1) is the highest, followed by the two Bi_2Se_3/YIG/GGG samples (#2 and #3). We note that the resistance curves of samples #2 and #3 are not the same although they are grown under nominally the same conditions. Below 20 K, however, the resistance has a minimum and starts to increases as the temperature decreases. A comparison of the low-temperature insulating behaviors of all samples is shown in the inset of Fig. 3.22, and it is clear that the insulating behavior is more pronounced in the bilayer samples. The onset temperature of the insulating behavior is also higher in bilayer samples. These results suggest that the presence of magnetic layer may be responsible for the stronger insulating behavior in the bilayer samples[70].

The Hall effect measurements indicate that charge carriers of Bi_2Se_3 in all samples are of n-type with a net carrier density ~$4\times10^{19}/cm^3$ which does not vary significantly (from 3.7×10^{19} to $4.4\times10^{19}/cm^3$) among the four samples. Fig. 3.23 shows a comparison of the Hall conductance, G_{xy}, between the control sample and a bilayer sample (#3). The non-linear G_{xy} in the control sample suggests the co-existence of more than one type of carriers. Similar non-linear Hall data are also found in other TI materials and attributed to the transport of both surface and bulk carriers[25,28,71]. However, the non-linear Hall effect is strongly suppressed in the bilayer samples with the inserted YIG magnetic layer, suggesting one type of carriers dominating the transport. We assume that only the surface channel in the bilayer samples is affected due to the presence of the adjacent YIG layer, which gives rise to the nearly linear Hall conductance dominated by the bulk carriers. To find out the mobility and carrier density for corresponding channels, we do the two-band fitting[71] to our Hall conductance data in both control and bilayer samples:

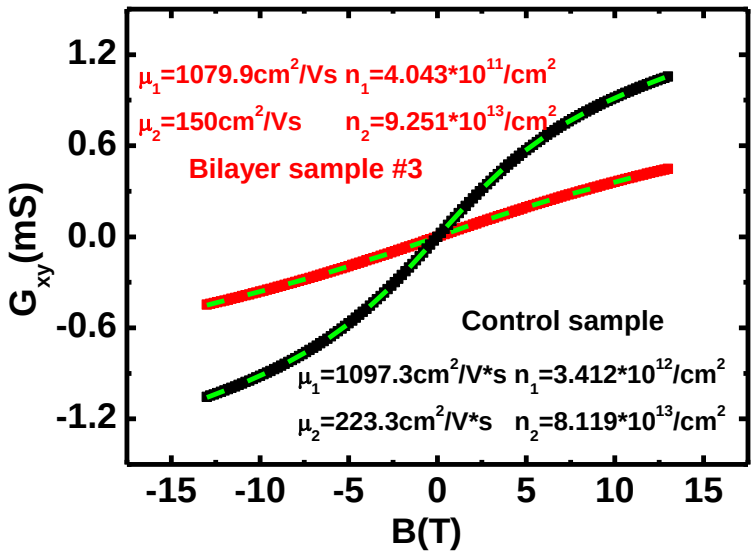

Fig. 3.23 Two band fitting for the Hall conductance of control sample and bilayer sample #3. The mobility and corresponding carrier density is noted in the figure.

$$G_{xy}(B) = eB\left(\frac{C_1\mu_1 - C_2}{\left(\frac{\mu_1}{\mu_2} - 1\right)(1 + \mu_2^2 B^2)} + \frac{C_1\mu_2 - C_2}{\left(\frac{\mu_2}{\mu_1} - 1\right)(1 + \mu_1^2 B^2)}\right)$$

Where B is the applied magnetic field in the perpendicular direction, μ_1 and μ_1 are the carrier mobilities of two channels, n_1 and n_2 are the carrier densities of two channels, and $C_1 = n_1\mu_1 + n_2\mu_2 = \frac{G_{xx}(0)}{e}$, $C_2 = n_1\mu_1^2 + n_2\mu_2^2 = \lim_{B\to 0}\frac{G_{xy}(B)}{eB}$ are combinations of the carrier density and mobility in two channels and can be obtained directly from the longitudinal and Hall data, i.e., G_{xx} and G_{xy}. The fitting results are displayed in the Fig. 3.23. The mobility of channel one is at least a factor of 5 higher than that of channel two, and it is not affected by the presence of YIG. However, the density of this channel is decreased dramatically in the bilayer sample. On the other hand, both mobility and carrier density of channel two do not change significantly after inserting the YIG layer. Hence, we assign channel one as the surface channel and channel two as the bulk channel, respectively. Clearly, the surface channel has higher carrier mobility than the bulk channel. In the meantime, we find that the 2D carrier density of the surface channel of the bilayer sample ($n_{surface}$=4.0×10^{11}/cm^2) deceases by one order of magnitude compared with that of the control sample ($n_{surface}$=3.4×10^{12}/cm^2). Similar effects are found in other bilayer samples, confirming that the surface channel of Bi_2Se_3 is affected by the presence of an insulating magnetic layer.

Fig. 3.24-a shows the normalized magneto-resistance data at 1.9 K for all samples taken under a perpendicular field from -13 to 13 T. They have overall positive MR up to 13 T, but the high-field MR curve of the control sample (solid) is well separated from those

of the 3 bilayer samples (dashed). The high field positive MR trend is reduced in the bilayer samples.

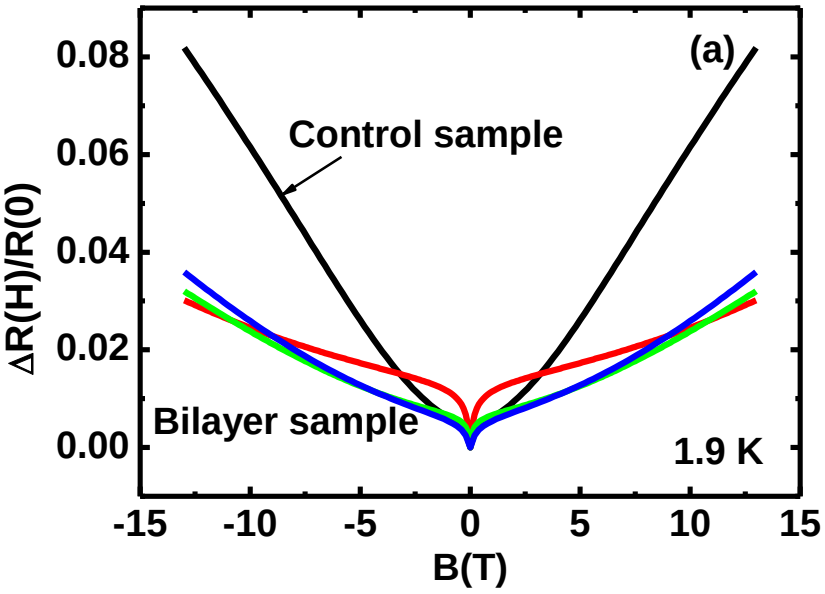

Fig. 3.24-a, Magnetoresistance of control sample and bilayer samples in high field.

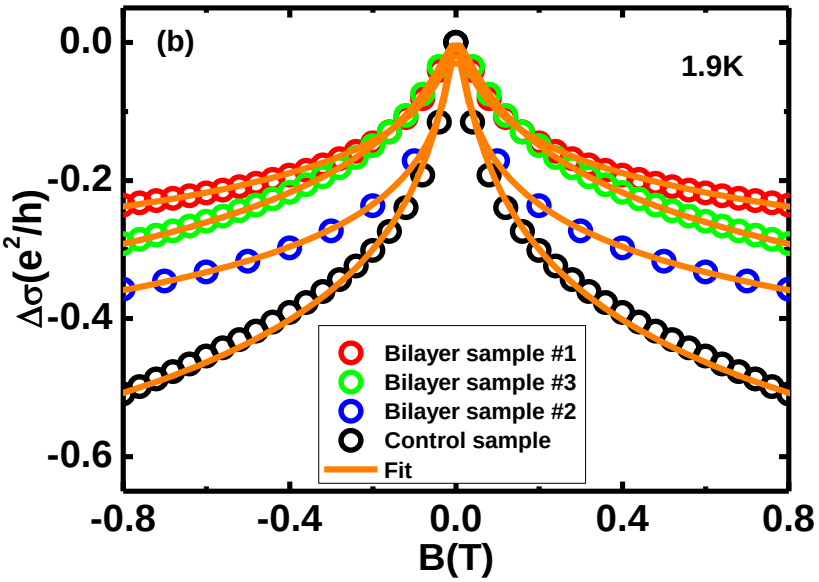

Fig. 3.24-b, Magnetoconductance of control sample and bilayer samples with fits at low field region.

Fig. 3.24-b shows the low field magneto-conductance (MC) data in the low field region of the MR data in Fig. 3.24-a. The cusp-like MC data are normally attributed to the weak anti-localization (WAL) effect in materials with strong spin-orbit coupling. Clearly, our data show that the WAL effect in Bi_2Se_3 is suppressed by being placed in proximity with YIG as seen in Fe/TI devices[72] and predicted by theory[73]. To understand the origin of the weakened WAL cusp in the bilayer samples, we carry out a quantitative analysis of the low-field MC data. In Fig. 3.24-b, the low-field MC is defined as $\Delta\sigma(B)=\Delta\sigma_{xx}(B)- \Delta\sigma_{xx}(0)$. We adopt the Hikami-Larkin-Nagaoka (HLN) theory to fit the MC data. In the limit that the inelastic scattering time is much longer that both the elastic and spin-orbit scattering times, the field dependent conductance is described by the HLN theory[74] as

$$\delta\sigma(B) = \sigma(B) - \sigma(0)$$
$$= \frac{\alpha e^2}{2\pi^2\hbar}\left[\Psi\left(\frac{1}{2}+\frac{\hbar}{4eBl_\phi^2}\right) - \ln\left(\frac{\hbar}{4eBl_\phi^2}\right)\right]$$

where l_ϕ is the phase coherence length, ψ is the digamma function, and α is a coefficient determined by the type of localization. In the absence of magnetic scattering, α has a value of -0.5 (symplectic case), which is the prefactor for the pure WAL with single coherent channel. In the case of magnetic scattering, α=0, namely, the unitary group. However, the weak localization-like MC has a prefactor of 0.5. The MC of control Bi_2Se_3 sample can be fitted very well with α=-0.5, which is confirmed in another control Bi_2Se_3 sample (20 QL) (lower left circle in Fig. 3.24-c). Previously reported α values in Bi_2Se_3 samples with different thickness (≥5 QL) were also found to be distributed over a narrow range near -0.5[75-77]. Our observations in the control samples are consistent with those experiments.

However, the α values of the bilayer samples (#1, #2 and #3) are in the range of -0.25 to -0.35, consistently smaller in magnitude than those of the control samples (Fig. 3.24-c).

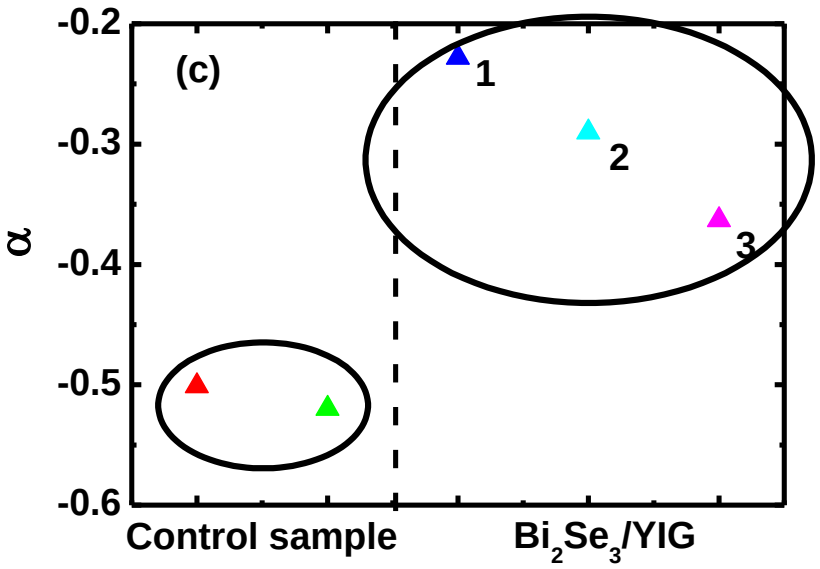

Fig. 3.24-c, The obtained HLN fitting parameter α for both control sample and bilayer samples.

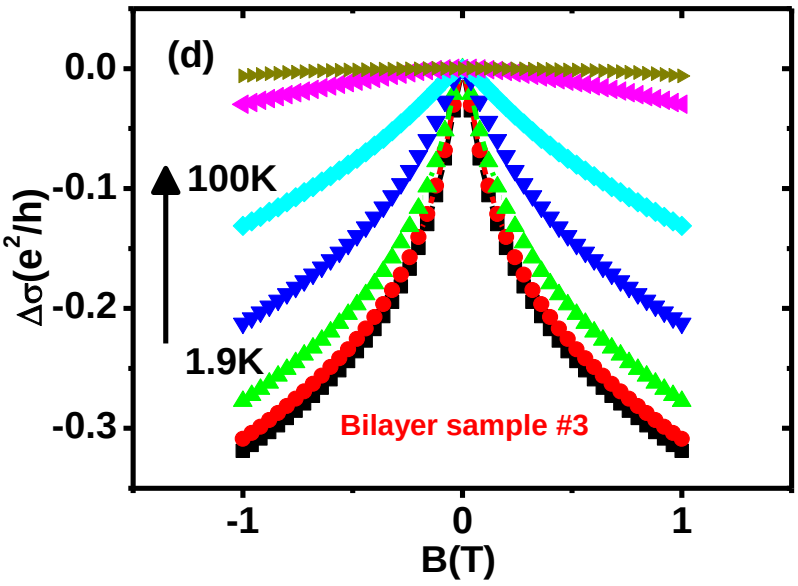

Fig. 3.24-d, Temperature-dependent low field MC for bilayer sample #3.

Clearly, the bilayer samples distinguish themselves from the control sample in term of the α value, suggesting a trend transitioning towards the unitary class from the symplectic class as a consequence of more magnetic scattering[72,73]. In Bi_2Se_3/YIG/Si, since there is likely more spin disorder in polycrystalline YIG, the stronger magnetic scattering may be responsible for the most reduced α value.

Fig. 3.24-d shows a temperature dependent low-field MC for bilayer sample #3. The thermal broadening of the negative MC reduces the WAL effect quickly as the temperature increases, which is reflected in the decreasing α value from the HLN fitting (Fig. 3.24-e, upper curve). Such a trend slows down and approaches saturation below 10 K. The α value extracted for the control sample shows a similar trend[25] but remains larger in magnitude than that of the bilayer sample (Fig. 3.24-e, lower curve). The gap between these two curves is the largest at the lowest temperature and decreases steeply at high temperatures.

Fig. 3.24-f shows the temperature dependence of the coherence length l_ϕ in the control sample and bilayer sample #3 extracted using HLN formula described above. Theoretically, the coherence length is proportional to $T^{-1/2}$ and $T^{-3/4}$ in 2D and 3D systems respectively for electron-electron interaction[79]. The monotonic decrease of the coherence length as the temperature increases is observed in both bilayer sample #3 (lower) and control Bi_2Se_3 sample (upper), similar to other TI systems[51,78,80]. The fitting gives $l_\phi = T^{-0.44}$ for bilayer sample #3 and $l_\phi = T^{-0.43}$ for the control sample, suggesting WAL at low fields originates from the 2D surface states. Moreover, we notice here that the phase coherence length for Bi_2Se_3/YIG bilayer sample is smaller than that for Bi_2Se_3 control sample,

especially at low temperatures. For example, at 1.9 K, the l_ϕ for bilayer sample #3 is 129 nm which is obviously smaller than

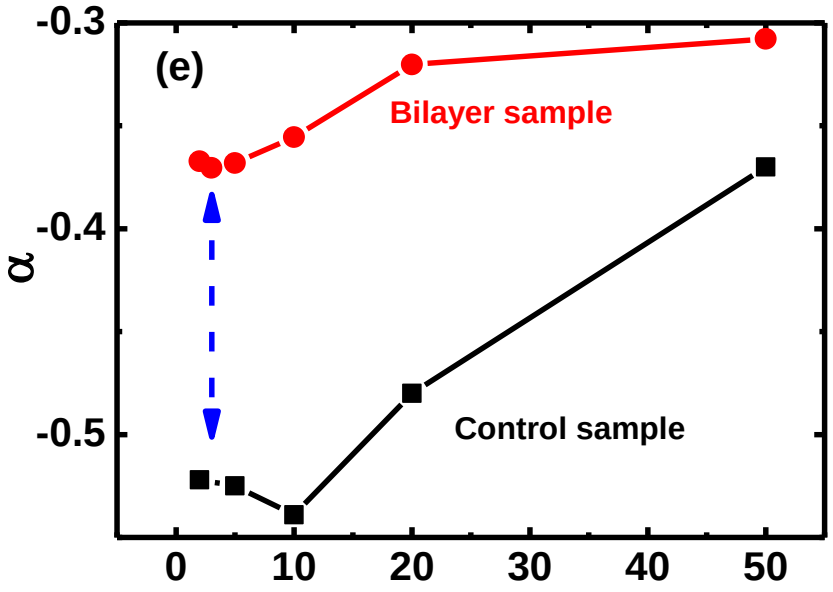

Fig. 3.24-e, Temperature dependent prefactor α for bilayer sample #3 and control sample.

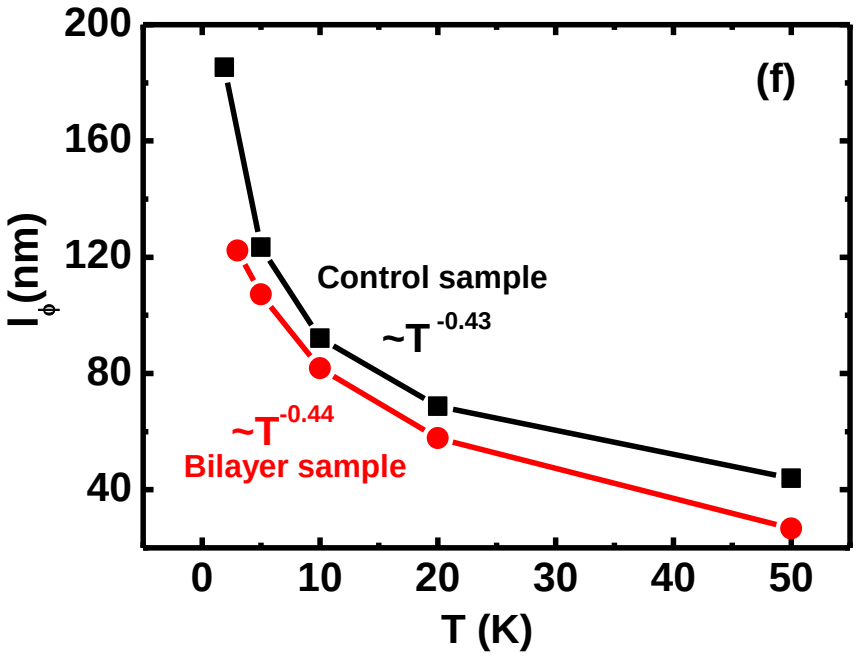

Fig. 3.24-f, Temperature dependent phase coherence length for bilayer sample #3 and control sample.

that of the pure Bi_2Se_3 (190-350 nm)[72,77,78]. The reduction of the coherence length in bilayer sample is probably caused by additional inelastic scattering such as electron-magnon scattering due to the topological insulator surface states next to the magnetic layer[72,73].

In summary, our transport results on 20 QL Bi_2Se_3/YIG bilayer structures indicate strong suppression of the surface transport channel as well as the weak antilocalization in the topological surface states. We attribute these transport phenomena to the increased magnetic scattering at the TI/MI interface. However, a typical proximity induced ferromagnetism behavior such as anomalous Hall effect or anisotropic magnetoresistance is absent in current 20 QL Bi_2Se_3/YIG heterostructure. We expect to see a stronger magnetic proximity effect in bilayers with a thinner and more insulating TI layer.

3.4 Proximity Induced Ferromagnetism in 5 QL $(Bi_xSb_{1-x})_2Te_3$/YIG Heterostructure

Quantum anomalous Hall effect (QAHE) requires both a spontaneous ferromagnetic order and a topological nontrivial inverted band structure[40,42,81]. To introduce the ferromagnetic order, random doping of transition metal elements, e.g. Cr or V, has been employed[56,82-84]. Although the Curie temperature (T_C) of the magnetic TI can be as high as ~ 30 K[56,82], QAHE only occurs at temperatures two-three orders of magnitude below T_C[43-45,56]. While the mechanism of this large discrepancy remains elusive, in order to observe QAHE at higher temperatures, it is essential that the exchange interaction in magnetic TI is drastically increased; in the meantime, the magnetic disorder needs to be greatly reduced. For the random doping approach, it is rather difficult to accomplish these

two objectives. An alternative way to address both issues simultaneously is to couple a non-magnetic TI to a high T_C magnetic insulator to induce strong exchange interaction via the proximity effect[41,85,86].

The magnetic proximity effect is a well-known phenomenon that has been intensely investigated[62-67,87-91]. By proximity coupling, the surface layer of TI acquires a magnetic order without being exposed to any random magnetic impurities[62-67]. This heterostructure approach was previously adopted in ref. [62] using EuS, a ferromagnetic insulator with a band gap of 1.6 eV and a T_C of ~ 16 K, grown on a 20 quintuple-layer (QL) thick Bi_2Se_3. Both magnetoresistance and a small AHE signal at low temperatures were ascribed to an induced magnetization in Bi_2Se_3. Alternatively, YIG has a much larger band gap (~ 2.85 eV) and a much higher T_C (~ 550K), and therefore is a better magnetic insulator for heterostructures. In Bi_2Se_3/YIG, the magnetoresistance observed at low temperatures indicates an interaction effect between the two materials[65,66]. We observed suppressed weak anti-localization in 20 QL-Bi_2Se_3 on YIG (ref 66 and see last section). Based on our recent successes in Pd/YIG[90], Bi_2Se_3/YIG[66], and graphene/YIG[89], here we demonstrate that high-quality heterostructures of 5 QL thick $(Bi_xSb_{1-x})_2Te_3$ grown on atomically flat YIG films exhibits induced ferromagnetism at the TI surface. By varying the ratio of Bi to Sb, we can effectively tune the electronic properties such as the carrier density and resistance of the TI layer without affecting the magnetic properties of YIG or the induced magnetic layer in TI.

The 5 QL thick (Bi_xSb_{1-x})2Te3/YIG-(111) heterostructure growth and characterization has been summarized in section 3.2, which reveals the much higher quality

than 20 QL Bi_2Se_3/YIG (110) sample and indicates single crystalline TI grown on YIG (111) substrate with clean and sharp interface.

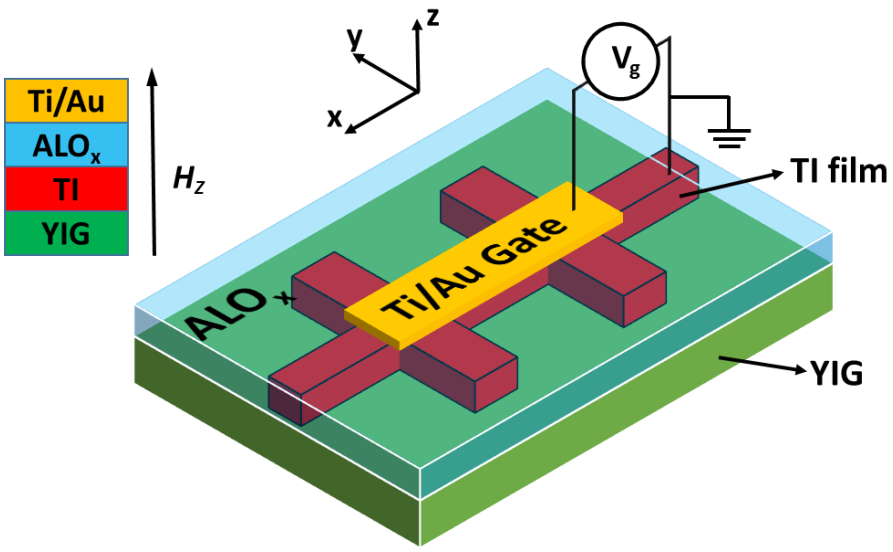

Fig. 3.25 Schematics of 5 QL $(Bi_xSb_{1-x})_2Te_3$/YIG device with top gate.

For transport studies, Hall bars of 900 μm ×100 μm were fabricated by photolithography and etching the TI layers by inductively coupled plasma (ICP). For selected samples, a 50 nm thick Al_2O_3 layer was grown as a top gate dielectric by atomic layer deposition (ALD), and a 80 nm thick Ti/Au layer was deposited by electron beam evaporation to form a top-gated device as shown in Fig. 3.25.

In this work, we have prepared multiple $(Bi_xSb_{1-x})_2Te_3$ samples with six different Bi fractions, *i.e.* x=0, 0.16, 0.24, 0.26, 0.36, and 1. By varying Bi content, the carrier concentrations of TI samples are systematically controlled[31,92], so that the position of the Fermi level is tuned from the bulk valence band (e.g. x=0), through the band gap

(intermediate x's), and to the bulk conduction band (e.g. x=1). The Fermi level position tuning allows us to control the relative contributions to electrical transport from the bulk and surface states. For the surface state-dominated samples (e.g. x=0.24), we can continuously fine tune the Fermi level across the Dirac point by electrostatic gating.

Fig. 3.26 displays the temperature dependence of five TI/YIG samples. For the Bi_2Te_3 (x=1) and Sb_2Te_3 (x=0) samples at the extreme doping levels, the resistivity (R_{xx}) is lower than that of the other three samples over the entire temperature range. Moreover, these two samples show metallic behaviors, *i.e.* $dR_{xx}/dT > 0$ over the most temperature range, while the other three samples show a stronger insulating tendency, *i.e.* $dR_{xx}/dT < 0$, due to depletion of bulk carriers at lower temperatures. Among these three insulating samples, the x=0.26 sample has the highest R_{xx} at 2 K, reaching 8.4 kΩ. Fig. 3.27 summarizes both the 2 K resistivity and the carrier density vs. the Bi fraction x. As x increases from 0 to ~ 0.16, R_{xx} increases and the carriers are holes from the Hall measurements. The hole carrier density decreases as x approaches 0.16. The increasing R_{xx}, decreasing 2D carrier density, and the insulating behavior of x= 0.16 sample all indicate that the Fermi level shifts up from the bulk valence band into the bulk band gap[31]. As x increases further, the R_{xx} continually increases, and the 2D hole density passes the minimum and then carriers switch to electrons. These facts suggest that the Fermi level passes the Dirac point of the topological surfaces states between x~ 0.16 and 0.26. As x increases further, the Fermi level shifts up more and finally enters the bulk conduction band as x approaches 1. Fig. 3.28 illustrates a schematic band diagram when x is varied[18]. The actual band structure and the precise Fermi level position for each x require detailed first-

principles calculations. Nevertheless, the relative position of the Fermi level with respect to the Dirac point for different *x* values can be qualitatively determined from our experimental data.

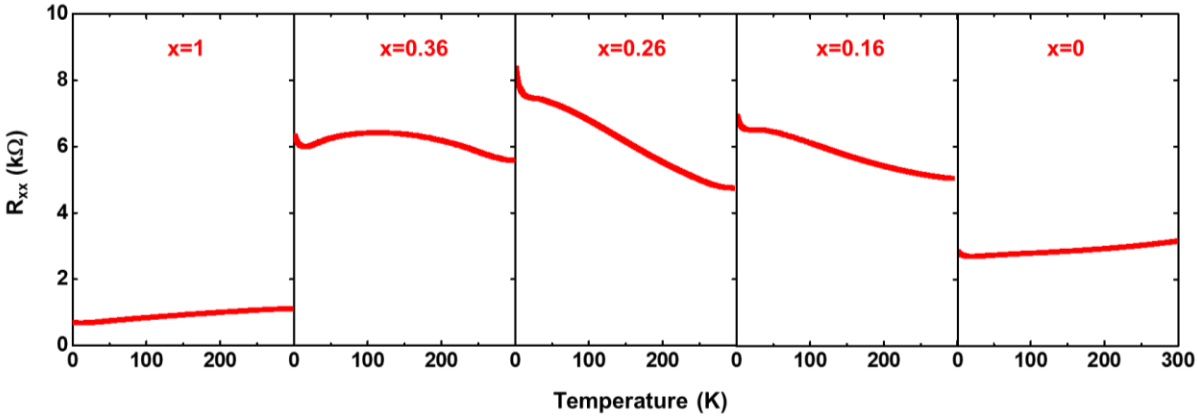

Fig. 3.26 Temperature dependent R_{xx} of 5 QL $(Bi_xSb_{1-x})_2Te_3$/YIG samples with x varying from 0 to 1.

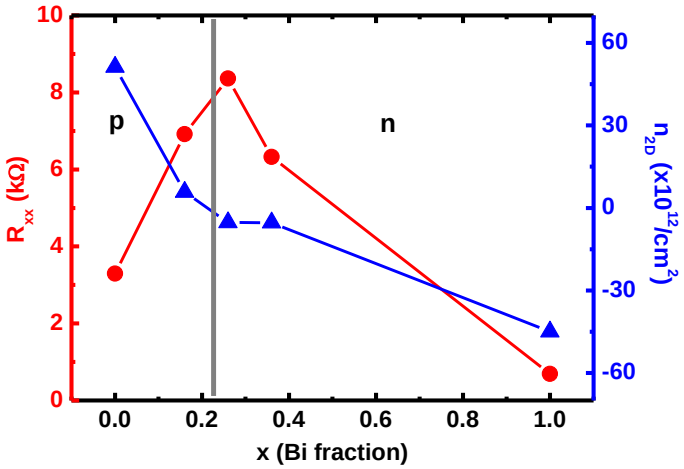

Fig. 3.27 Longitudinal resistance and carrier density vs. Bi fraction.

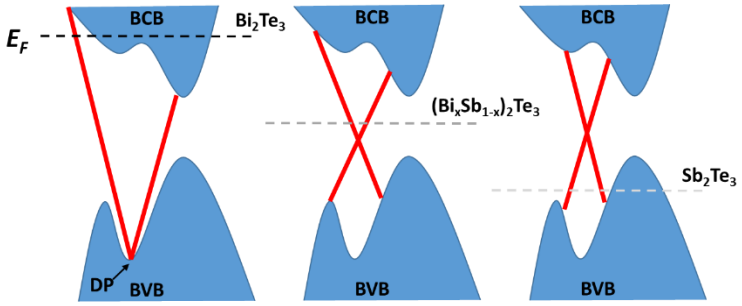

Fig. 3.28 Schematic electronic band structure of $(Bi_xSb_{1-x})_2Te_3$ on YIG indicating the shift of Fermi level as x is varied.

To probe the proximity induced ferromagnetism in the TI surface contacting YIG, we focus on the nonlinear Hall signal by removing the dominant linear ordinary Hall background signal[62,89]. The inset of Fig. 3.29 shows a comparison between Bi_2Te_3/YIG and Bi_2Te_3/Si. Both have strong linear Hall signals with negative slopes as expected for an n-type Bi_2Te_3. The carrier density of TI layer is $4.4x10^{13}/cm^2$ for Bi_2Te_3/YIG and $5.4x10^{13}/cm^2$ for Bi_2Te_3/Si, which is not very sensitive to substrate. However, as the linear background is removed, the remaining Hall signal from the two samples shows a distinct difference. While Bi_2Te_3/Si does not have any definitive nonlinear signal left, Bi_2Te_3/YIG has a clear nonlinear component with a saturation feature. In general, non-linearity in Hall voltages can arise from co-existing two types of carriers. In fact, such non-linearity is often observed when the Fermi level is in the vicinity of the Dirac point where both electrons and holes are present[71]. These two samples are clearly in the single carrier type regime; therefore, we exclude the two-carrier possibility. The shape of the nonlinear Hall signal in Bi_2Te_3/YIG resembles that of the YIG hysteresis loop in perpendicular magnetic fields (Fig. 3.30). We thus assign this nonlinear signal a contribution from AHE. Further evidence will be discussed shortly. Although it is not straightforward to determine the exact physical origin of the observed AHE, it is known that AHE must stem from ferromagnetism in conductors[37]. Since the underlying YIG is found to remain insulating (resistance >40 GΩ) when measured after the TI growth, etching, and device fabrication are completed, we exclude that the YIG surface itself becomes conducting and contributes to the AHE signal. Moreover, since YIG is grown at ~700 ℃ while TI is grown at ~ 250 ℃ later, we do not expect any significant diffusion of Fe atoms to dope the TI to turn it to ferromagnetic.

Hence, we conclude that the bottom metallic surface of the TI film becomes ferromagnetic via the proximity coupling just as what has been observed in other systems[62,89-91].

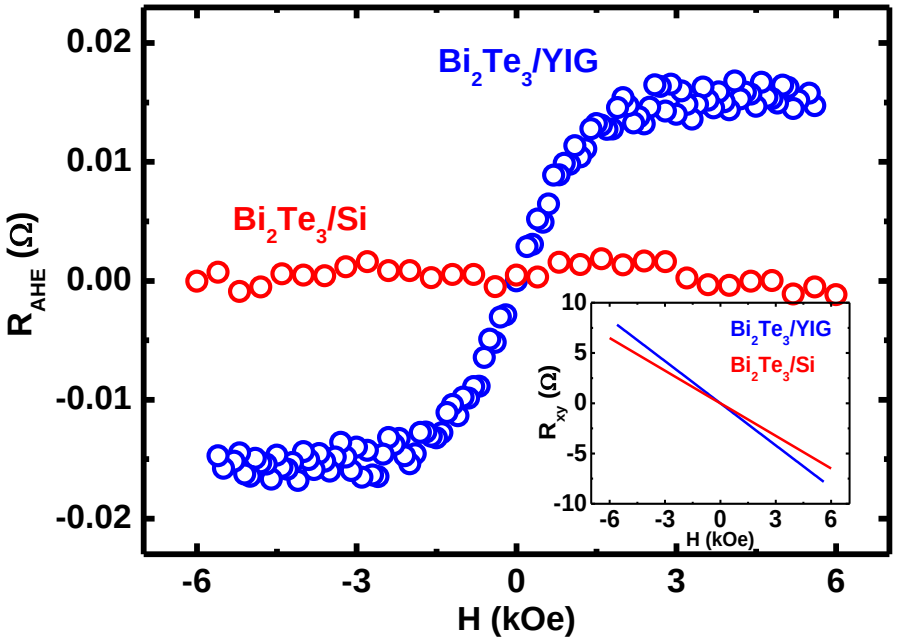

Fig. 3.29 A comparison of nonlinear Hall resistivity after linear Hall background is removed in Bi_2Te_3/YIG and Bi_2Te_3/Si.

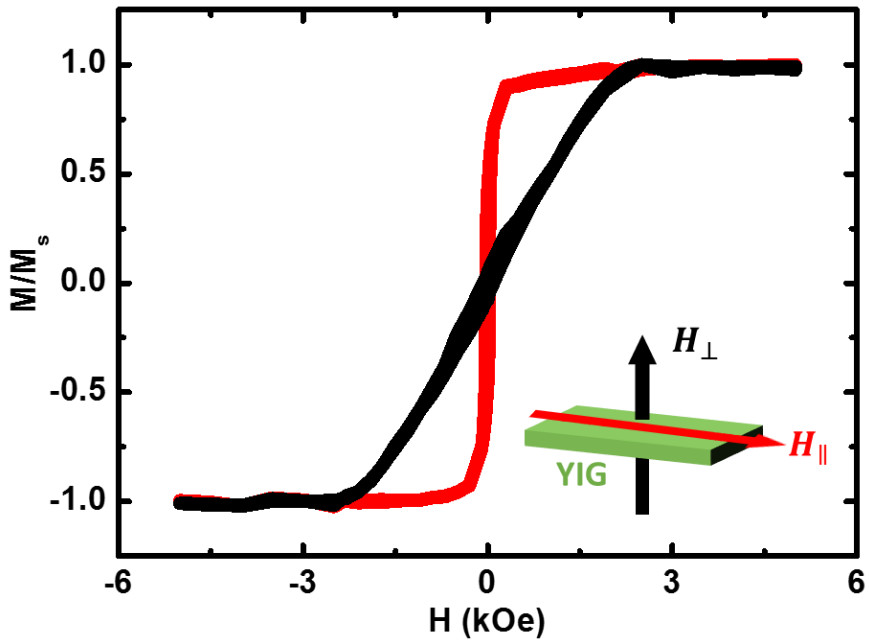

Fig. 3.30 Typical VSM data of YIG (111) sample as a reference.

Note that in the Bi_2Te_3 sample (x=1) the saturation value of the AHE magnitude R_{AHE} is only ~ 0.015 Ω, much smaller than R_{xx}. In fact, all samples show clear AHE signals at 2 K. More importantly, as the carrier type switches as x goes from 0.16 to 0.26, the sign of the AHE resistivity remains the same. Since the ordinary Hall effect arises from the Lorentz force associated with an external magnetic field such as the stray magnetic field from domain boundaries, if the nonlinear Hall signal observed here is due to the ordinary Hall effect, its sign would change as the carrier type switches. The absence of the sign change further confirms the AHE nature of the nonlinear Hall signal, *i.e.* it is a consequence of the induced ferromagnetic surface of TI. Moreover, R_{AHE} follows the same trend as that of R_{xx} (Fig. 3.31), i.e. the more insulating samples showing larger R_{AHE}. In x= 0.26 sample, R_{AHE} jumps to nearly 2 Ω, over two orders of magnitude larger than in Bi_2Te_3 (x=1). After passing the crossover point, R_{AHE} decreases to 1.5 Ω at x=0.16 and finally drops to 0.12 Ω at x=0 (Sb_2Te_3) which is only 10% of the maximum value. Quantitatively, the correlation between R_{xx} and R_{AHE} can be better seen in Fig. 3.32 where a power-law with an exponent ~ 2 best fits the data. Since $\rho_{xy} \ll \rho_{xx}$, and $\sigma_{xy} = -\frac{\rho_{xy}}{\rho_{xx}^2+\rho_{xy}^2}$, this power-law suggests that the AHE conductivity is nearly independent of ρ_{xx}. Since x is the controlling parameter, the quadratic relation between ρ_{xx} and ρ_{xy} suggests that σ_{xy} is constant, which rules out the skew scattering mechanism.

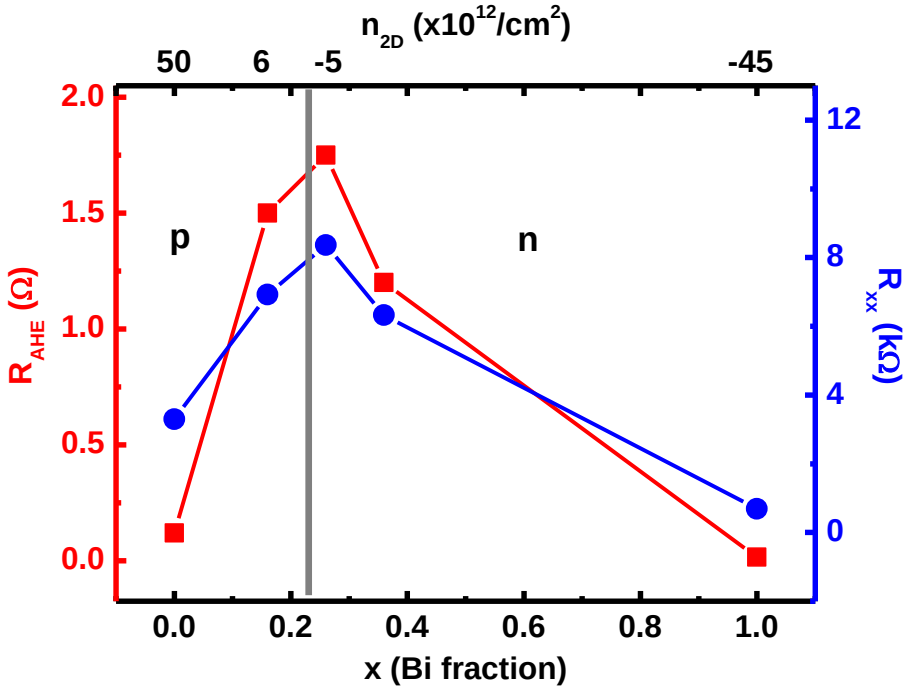

Fig. 3.31 AHE resistance and longitudinal resistance vs. Bi fraction and 2D carrier density.

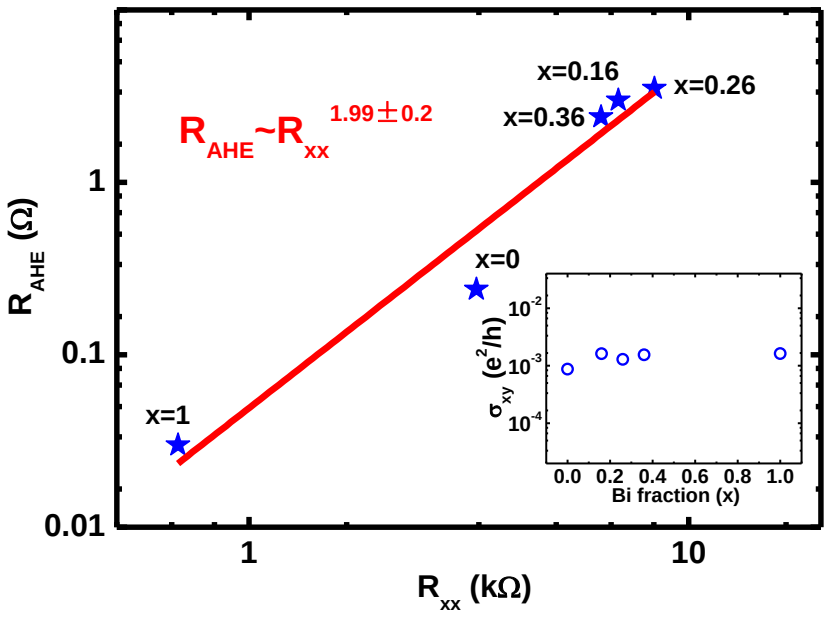

Fig. 3.32 Log-log plot for AHE resistance vs. R_{xx} for five samples. The inset shows the AHE conductivity remains constant as x is varied.

The induced ferromagnetism arises from the hybridization between the boundary layers of the two materials in the TI/YIG heterostructures; therefore, the resulting exchange coupling is expected to be weaker than that in the interior of YIG[62]. Additionally, less than ideal interfaces can further weaken the exchange coupling strength. To quantify the exchange interaction of the proximity effect, we measure the AHE signal as the temperature is increased until it vanishes. We define it as the ferromagnetic ordering temperature or T_C for the induced magnetic layer in TI. The T_C of all TI/YIG samples is above 20 K and can be as high as ~ 150 K, as shown in Fig. 3.33. There seems to be no correlation between T_C and x or the carrier concentration (Fig. 3.34). Instead, this sample-to-sample variation may be attributed to variations in the state of the TI-YIG interface. Although it is not possible to pinpoint the most important factor (e.g. oxidation state and surface termination) responsible for the exchange strength, there is no fundamental reason that the T_C should be limited to 150 K. Future improvement of interface quality is expected to result in a higher T_C of the magnetized layer.

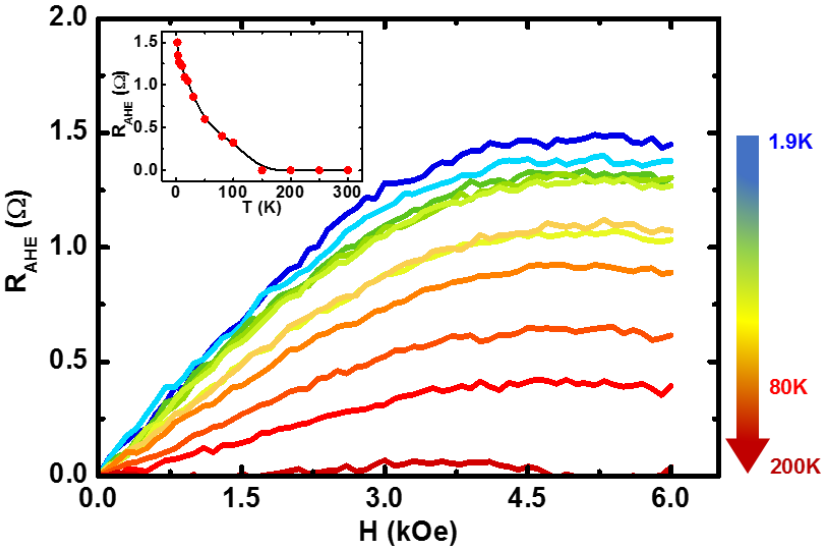

Fig 3.33 Temperature dependent AHE resistance for x=0.16 sample. The inset indicates a T_C around 150 K.

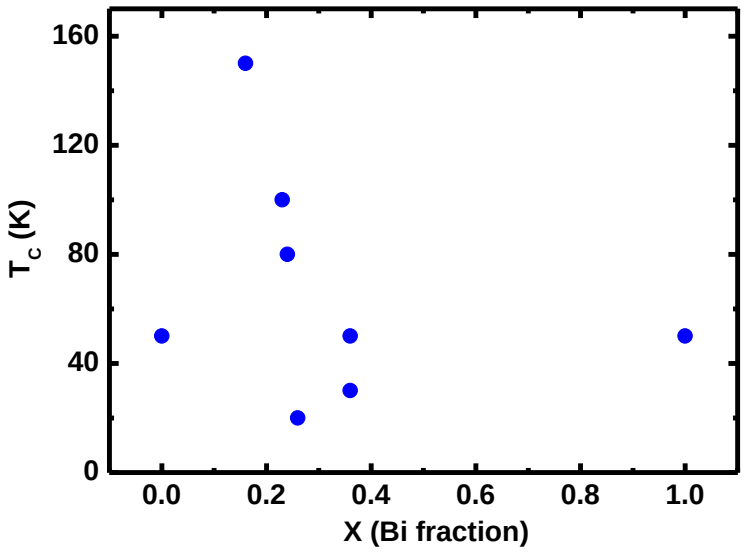

Fig. 3.34 An estimation of the interfacial ferromagnetic ordering temperature T_C of samples with different Bi fractions through temperature dependent AHE. T_C is obviously independent of Bi fraction/carrier concentration.

For the insulating samples whose Fermi level is located in the bulk band gap of the TI, we can further fine tune the position with a gate to access the surface states at different energies. Fig. 3.35 shows the gate voltage dependence of R_{xx} for the x=0.24 sample which has a top gate above a 50 nm thick Al_2O_3 insulator. At zero gate voltage, *i.e.* V_g= 0 V, the temperature dependence shows a bulk insulating behavior and the ordinary Hall data indicates the *p*-type conduction. Therefore, the Fermi level is located just below the Dirac point in the band gap. As the gate voltage is swept from negative to positive, the resistivity reaches a peak (R_{xx} ~ 22 kΩ) at V_g ~ 25 V and the carrier type switches from the *p*- to *n*-type as indicated by the ordinary Hall background. As V_g is swept, the Fermi level moves upwards and passes the Dirac point which coincides with the maximum in resistivity. The AHE data for two representative gate voltages, *i.e.* 0 and 40 V, are displayed in Fig. 3.36.

Although the ordinary Hall slope has opposite signs (not shown), the sign of the AHE remains the same on both sides of the Dirac point, which is consistent with the doping dependence discussed earlier. Interestingly, in samples with widely different doping levels, not only is the relative Fermi level position with respect to the Dirac point, but also the band structure is different[31,92]. Here in one sample, the electrostatic gating only shifts the Fermi level in a fixed band structure. Therefore, the fact that the AHE sign remains unchanged across the Dirac point is robust.

In summary, unlike in Cr- or V-doped TI, the ferromagnetism is only induced at the bottom surface of the TI layer in TI/YIG heterostructures. Nevertheless, we have demonstrated an alternative route of introducing stronger exchange interaction to TI surface states by proximity coupling. A stronger exchange should lead to a larger topological gap, therefore a higher temperature at which QAHE occurs. In the meantime, by independently optimizing the electronic properties of the TI, we can reduce disorder, especially magnetic disorder, and simultaneously tune the Fermi level position in TI without affecting the induced ferromagnetism.

Furthermore, the utilization of YIG canted magnetization or just replacement of YIG film by a PMA material may finally lead to the realization of quantum anomalous Hall effect in TI/MI heterostructure at much higher temperature. However, this requires an even thinner TI film to eliminate the side effect or coupling the TI bottom and top surfaces by a MI film separately to form a sandwich structure.

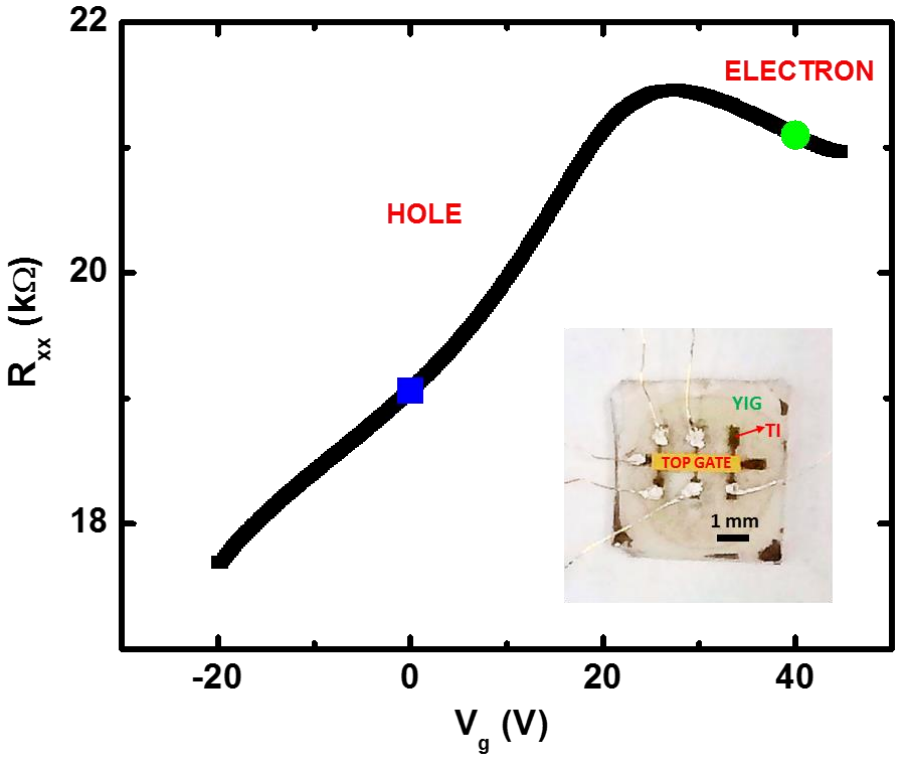

Fig. 3.35 Gate voltage dependence of R_{xx} for x=0.24 sample.

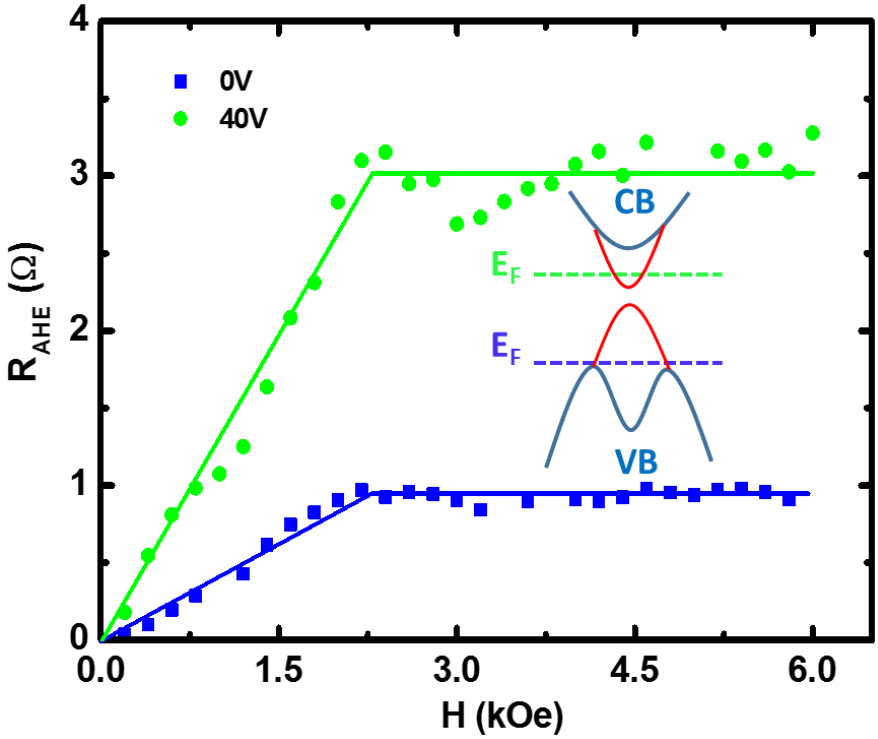

Fig. 3.36 AHE resistance at different gate voltages with opposite carrier types.

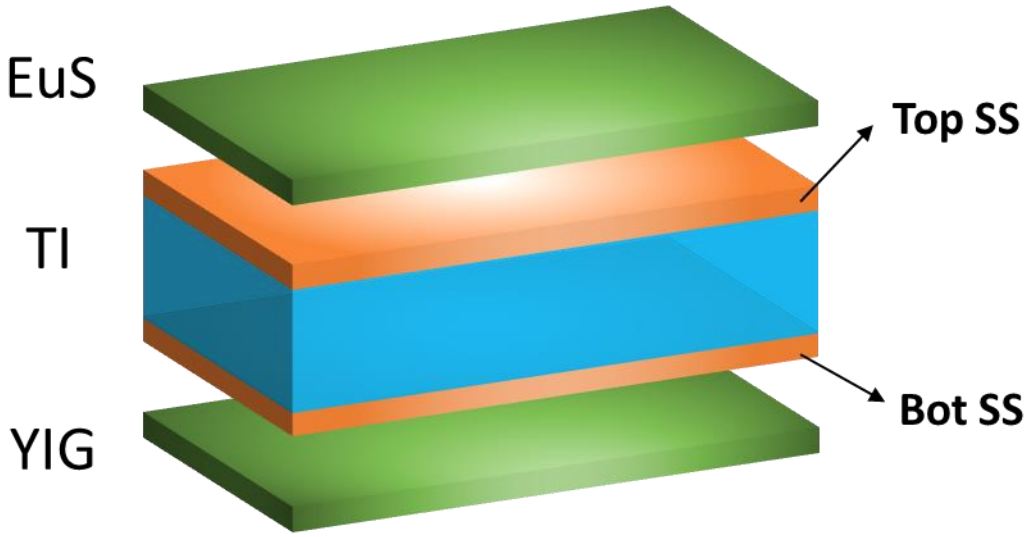

Fig. 3.37 Schematics of EuS/TI/YIG trilayer structure.

Recently, we indeed start to explore this idea by sandwiching a thin TI film between two magnetic insulators to form a EuS/TI/YIG trilayer structure, as shown in Fig. 3.37. We measure the transport property with similar structure as in the previous section. We find that the EuS/TI/YIG sample exhibits anisotropic magnetoresistance under in-plane magnetic field. More interestingly, when temperature is below 10 K (both surfaces could be magnetized), the AMR displays two pairs of dips (magnetization switch), accompanied by the planar Hall effect (see Fig. 3.38 and 3.39). The first jump in PHE happens at very small field region around ±60 Oe, while the second jump is observable at much higher field near ±450 Oe. The jumps in PHE indicates magnetization switching from one stable state to another stable state. Similar jumps can be identified in AMR and the positions of the jumps coincide with the two jumps in the planar Hall loops. Note, such an AMR with two abrupt jumps exists only below 10 K, when two surfaces of TI have exchange coupling

with EuS (T_C~16 K) and YIG (T_C~550 K) respectively. This behavior may be related with in-plane uniaxial magnetization (four-folder) of EuS.

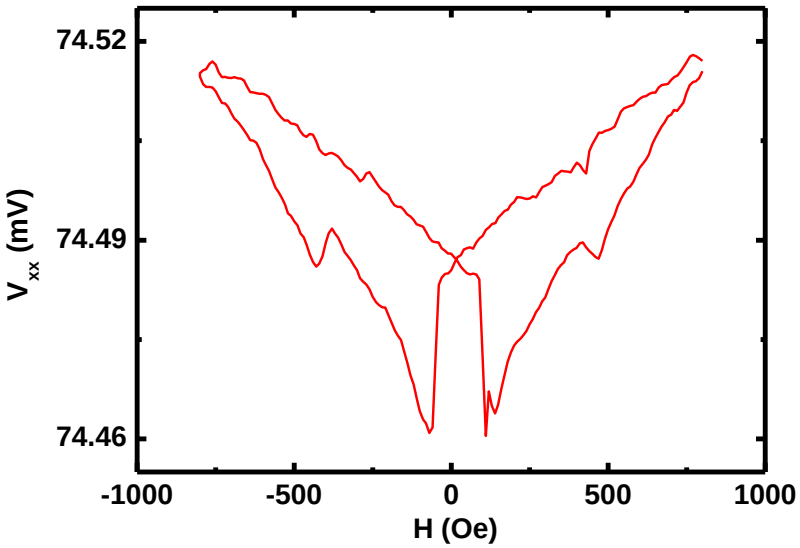

Fig. 3.38 AMR hysteresis loop of EuS/TI/YIG sample at 2K.

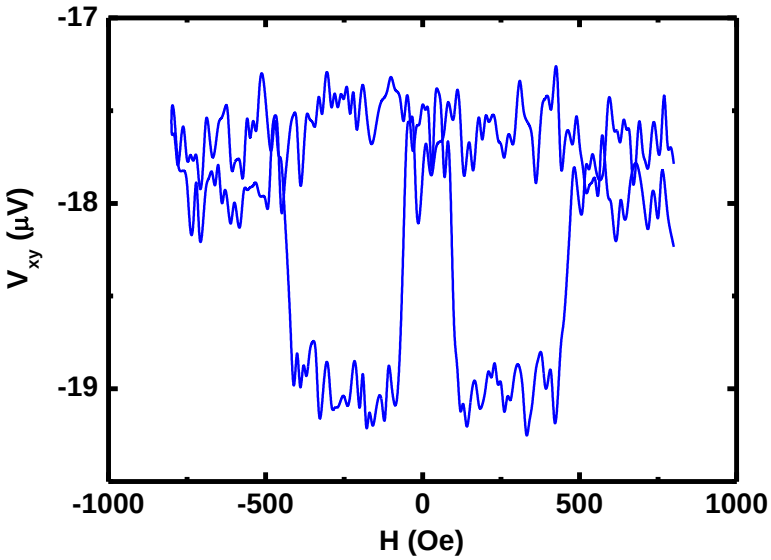

Fig. 3.39 Corresponding planar Hall effect.

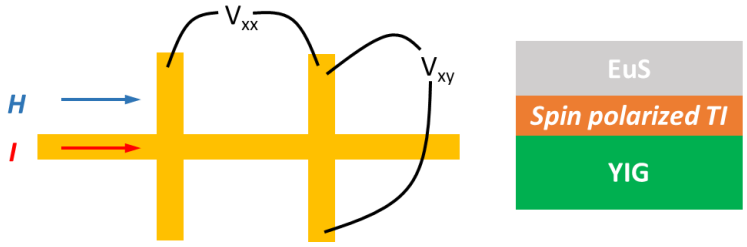

Fig. 3.40 AMR and PHE measurement geometry.

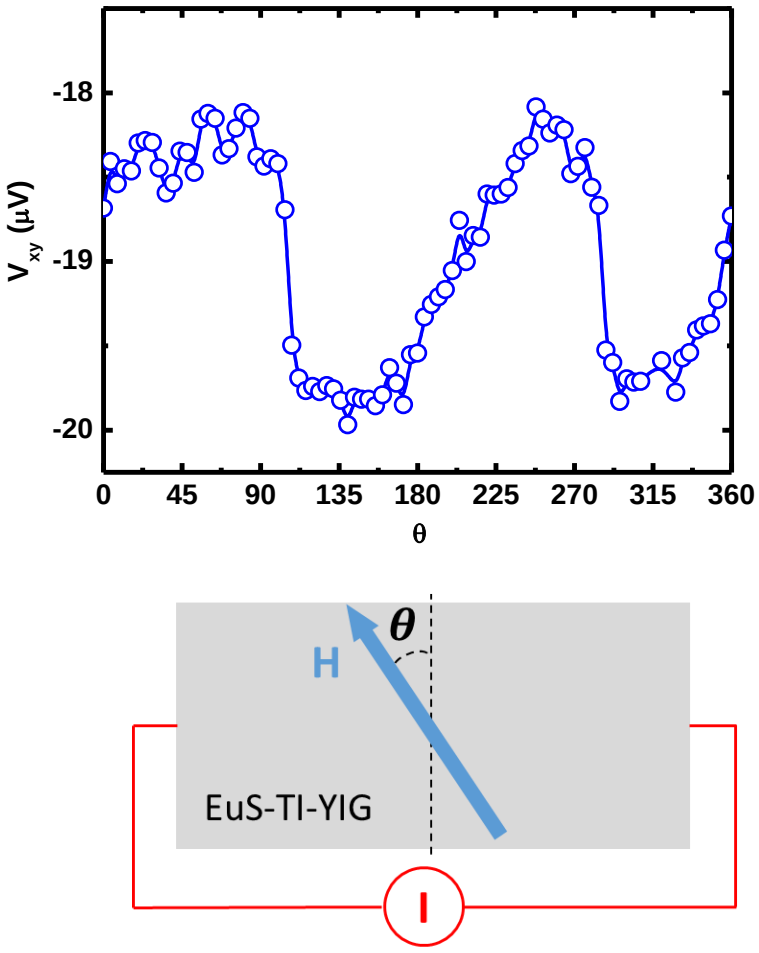

Fig. 3.41 PHE for angular dependent sweep at fixed H=1000 Oe.

The electric field within a single domain ferromagnetic film with in-plane magnetization has both x- and y- components when a current flows along x-direction for an arbitrary magnetization direction, which can be written as[93]

$$E_x = j\rho_\perp + j(\rho_\parallel - \rho_\perp)\, cos^2\, \varphi,$$

$$E_y = j(\rho_\parallel - \rho_\perp) sin\varphi cos\varphi.$$

The Hall resistance depicts the second equation, i.e., it exhibits extrema at φ=45° and its cubic equivalents. To further characterize the PHE property, we rotate the sample in the

film plane at an angle relative to the fixed magnetic field ~1000 Oe. As shown in Fig. 3.41, the measured Hall resistance exhibits extrema for field orientation of ~45 °, ~135 °, ~225 °, and ~315 °. Note the first maximum of planar Hall resistance appears at 45 °, indicating $\rho_{\parallel} < \rho_{\perp}$. At present, the mechanism of AMR and PHE features in EuS/TI/YIG sample has not been fully understood yet. More experiments are required to figure out whether this behavior comes from the combined effect of two magnetic layers or not.

Nevertheless, we observe the proximity induced ferromagnetism in TI at room temperature for the first time. Fig. 3.42 shows temperature dependent AMR ratio in EuS/TI/YIG sample. Clearly, 300 K is much higher than the Curie temperature of EuS, thus it does not contribute to the magnetization of TI surface. The bottom surface of TI is magnetized by exchange coupling with YIG film and exhibits a hysteretic MR feature at 300 K. The ferromagnetic order in such a heterostructure is much higher than any other TI material with transition doping approach. Stronger exchange in heterostructure sample will pave the way to the observation of QAHE in room temperature.

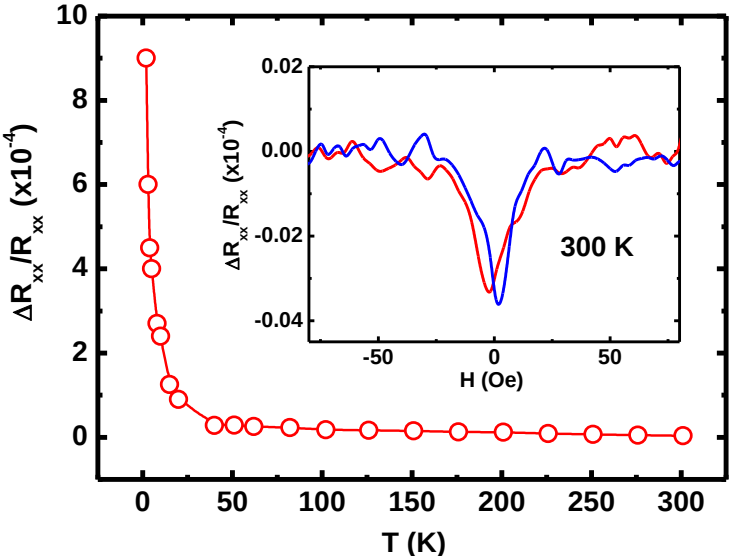

Fig. 3.42 Temperature dependent AMR ratio in EuS/TI/YIG sample. Inset shows the observation of hysteretic MR at room temperature.

Chapter 4 Spin Seebeck Effect Study on Topological Insulator-Magnetic Insulator Heterostructures

4.1 Overview of Topological Spintronics

Topological insulators belong to a new class of materials with properties dictated by the topology of electronic band structure. These materials have a high spin-orbit coupling which leads to metallic surface states due to parity change in occupied electronic states. The conservation of time-reversal symmetry in the surface states gives rise to the property of spin-momentum locking, where the direction of electron's motion uniquely determines its spin orientation and vice versa.

Schematics are shown in Fig. 4.1. At the Fermi level, right-moving (+x direction) and left-moving (-x direction) electrons have spins pointing to +y and –y or (-y and +y) directions, respectively. Therefore, if a spin imbalance is induced in the surface states by spin pumping, FMR or spin Seebeck effect, a charge current J_c is expected to exhibit along the Hall direction :

$$J_c // (\hat{z} \times \sigma)$$

Where σ is the spin polarization direction and $\hat{z}$ is the unit vector perpendicular to the plane (TI surface). However, due to the 2D nature of topological surfaces, spins cannot flow along $\hat{z}$ direction or penetrate into the bulk for an ideal bulk insulating topological insulator. As a result, the converted charge current will only flow on the surface and also has a 2D nature. The mechanism of this spin-charge conversion is different from that in the inverse spin Hall effect usually observed in a transition metal, where a pin current flowing within a finite thickness of a sample is converted into a 3D charge current along Hall direction.

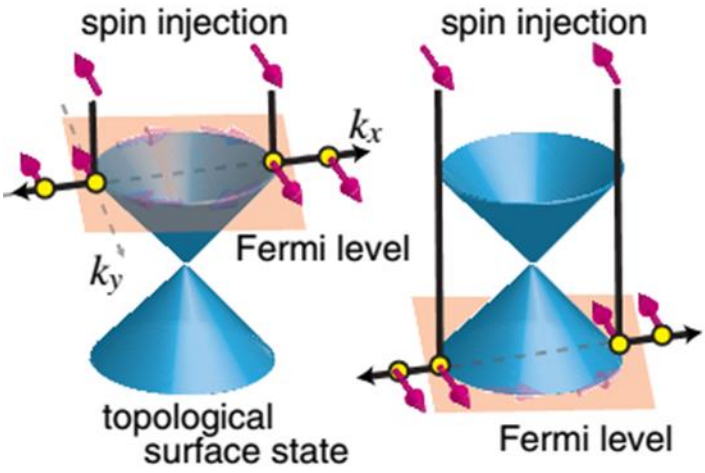

Fig. 4.1 Concepts for spin-charge conversion in topological surface states. Adapted from ref [93].

The spin texture of topological surface states has attracted emergent research interest recently, which has been probed by the spin-resolved photoemission[17], polarized optical spectroscopic techniques[94] and electrical transport experiment, naturally leading itself to potential exploitation for "topological spintronics'. Several theoretical proposals have estimated the possibility of manipulating the magnetization in a ferromagnetic layer via the spin-textured surface states[95-97]. Transport experiment studies including spin-torque ferromagnetic resonance (ST-FMR)[98-100], spin pumping effect[93,101,102], magnetic tunneling junction[103], spin valve device[48,104-108] and dc current-driven magnetization switching[109] have demonstrated that TIs are characterized by very efficient spin to charge conversion, which is even one or two orders larger than that generated by best heavy metal.

Although TI is suggested to exhibit ultrahigh spin to charge efficiency according to those experiments using TI/ferromagnet metal (FM) bilayer structures, a few fundamental

questions need to be addressed. First, so far, the mechanism of the observed phenomena remains largely unclear in TI based spintronics studies. Do the large spin torques and spin charge conversion signals measured in TI/FM heterostructures arise from spin-textured surface states or the bulk states instead which also have a large SOC? Different experiments with various TI materials and spin transport techniques have opposite arguments here. Second, large discrepancies in both magnitude and the temperature dependence of the measured effects exist in spin pumping and spin valve experimental approaches. For instance, in spin pumping FMR experiment of ref [93], the observation temperature of TI spin momentum locking is <30 K for BSTS device and the Bi_2Se_3 reference sample doesn't provide a signal. Nevertheless, in spin valve device of ref [48], the charge-spin conversion from topological surface states exists up to 150 K. And in ST-FMR experiment of ref [98], the spin-momentum locking detected is even robust at room temperature. A recent report by Banerjee group at Groningen even claim that signal generated by spin-momentum locking is temperature insensitive in their spin valve device[104]. Third, in a structure consisting of TI and FM, the magnetic metal deposited on top of surface states will cause the band bending and change the electronic structure of the TI, or form a magnetic dead layer as reported and can also induce magnetic proximity effect when directly coupled to non-magnetic TI surface. These questions are particularly germane in TI spintronics study and need to be addressed by careful experiment analysis with proper sample preparation.

4.2 The Spin Seebeck Effect

Spin Seebeck effect (SSE) was first discovered[110] in 2008, which refers to the generation of spin voltage as a result of temperature gradient in ferromagnetic materials. SSE has been observed in ferromagnetic metals[110], semiconductors[111], ferromagnetic

insulators[112,113] and even paramagnetic materials[114] very recently. It enables the construction of insulator-based thermoelectric generators in combination with the inverse spin Hall effect (ISHE), which was impossible if only conventional thermoelectric technology was used.

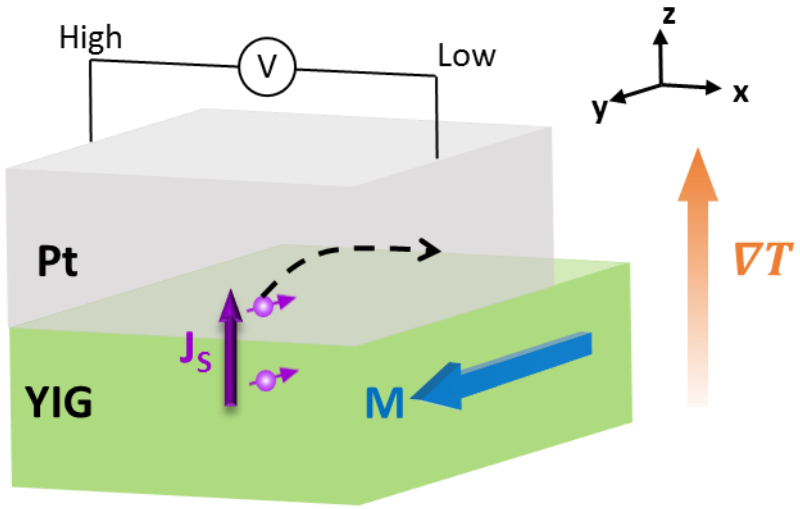

Fig. 4.2 Schematics of longitudinal SSE in Pt/YIG heterostructure.

Fig. 4.2 shows the schematics of a paramagnetic metal/ferromagnetic insulator heterojunction for detecting the longitudinal SSE. When a temperature gradient ∇T is applied to the insulator perpendicular to the metal/insulator interface (along z direction in Fig. 4.2), the spin voltage is thermally generated and injects a spin current into the paramagnetic metal across the interface owing to a thermal spin-pumping mechanism. This thermally induced spin current is then converted to an electric field E_{ISHE} by the ISHE in the heavy metal. If the magnetization M of the insulator is along the y direction, the electrical field is generated in the metal along x direction:

$$E_{ISHE} \propto J_S \times \sigma$$

In the longitudinal SSE configuration, J_S is parallel to the ∇T direction. The magnitude of E_{ISHE} is proportional to the resistivity and spin Hall angle of paramagnetic metal. By measuring the electric voltage across the two ends of adjacent metal film, one can easily find the SSE voltage as:

$$V_{SSE} = E_{SSE} L_x \propto \theta_{SH} R_{xx} \Delta T \, \hat{z} \times \sigma$$

Here $\boldsymbol{\sigma}$, θ_{SH}, and R_{xx} denote the electron spin polarization, the spin Hall angle and longitudinal resistance of heavy metal layer, respectively.

In conclusion, in the typical SSE system consisting of a magnetic insulator and a heavy metal layer, it utilizes the strong spin-orbit coupling of 3D bulk transition metal to convert the thermally driven spin current to charge voltage in an open circuit geometry. The SSE voltage results from the spin Hall conductivity of the heavy metal which reflects the spin-orbit coupling strength of heavy metal coupled with YIG, which can not be tuned by the electric-field effect. A natural question arises: what will happen if the adjacent metal film is replaced by YIG?

4.3 Topological Spin Seebeck Effect

As discussed in section 4.1, while there is little doubt that TIs offers a clear advantage over conventional conductors in generating and detecting pure spin currents, it has been unclear whether the unusually large effects are dominated by bulk or surface TI states. Discrepancies between experimental results from different groups, and between results from different samples under nominally identical conditions point to the importance of extrinsic conditions. Uncertainties related to the structure of the interface, including the

possibilities of intermixing of magnetic elements and proximity-induced ferromagnetism[115], can further complicate the interpretation of spin transport measurements. Therefore, to separate surface and bulk contributions, it is imperative to systematically tune the Fermi level relative to the bulk band gap.

In this work, we address an unusual spin Seebeck effect (SSE), the efficient conversion of thermally driven magnons into an electromotive force (emf) due to TI surface states which has never been reported. To exclude from our measurements the anomalous Nernst effect[116] induced emfs that result from the flow of spin-polarized charge in a ferromagnetic metal in SSE devices[110], we choose yttrium iron garnet (YIG), a ferrimagnetic insulator, as the source of magnons. In the longitudinal SSE configuration, a vertical temperature gradient in YIG drives a magnon current. In the steady state magnon flow toward the TI/YIG interface is balanced by decay of excess magnons via either magnon-phonon scattering in YIG or magnon interactions with TI surface or bulk electrons. Our experiments demonstrate that the electrical consequences of the decay of magnon population excesses or deficiencies are particularly simple and strong for TI surface states.

The mechanism of topological spin Seebeck effect is depicted in Fig. 4.3. When a magnon is created or annihilated, an electron flips from majority to minority spin-orientation or vice-versa to conserve total spin. When the YIG magnetization is in the $\hat{y}$ direction, spin-momentum locking in the TI surface states then leads to a net rate of momentum transfer $\delta\hbar k_x$ in the $\mp\hat{x}$ direction, with the sign depending on whether the Fermi

level lies in the surface state conduction or valence band. Because the relationship between momentum and velocity is opposite in the two bands, the opposite momentum transfer produces the same velocity direction of electrons. Hence, magnon relaxation via interaction with TI surface states leads to currents of the same sign for n or p surface states, or under open-circuit conditions to emfs of the same sign.

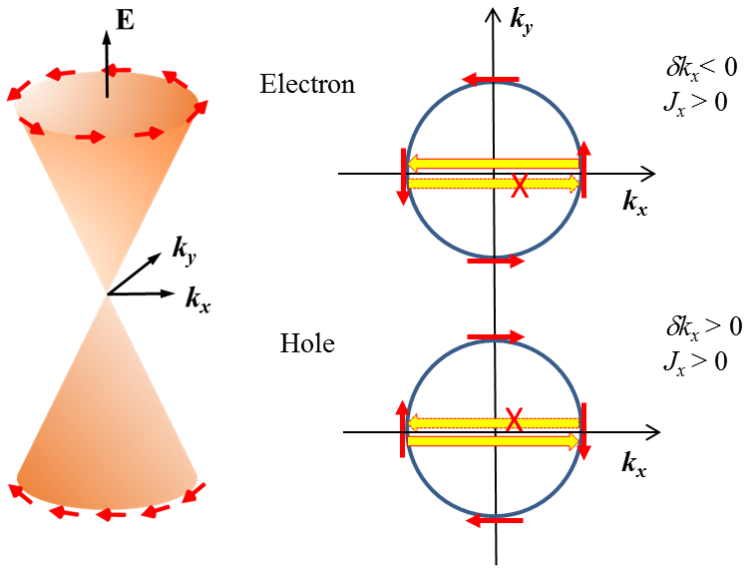

Fig. 4.3 Dirac-model topological insulator Fermi surface. Assuming isotropic exchange interactions between YIG and the topological insulator surface-states, electrons flip from majority to minority spin directions when a magnon is annihilated. For YIG magnetization in the y-direction, in the conduction band, magnon annihilation scatters electrons near the Fermi surface from k_x to $-k_x$ directions but not from $-k_x$ to k_x, resulting in a net flow of electrons along $-k_x$ or a positive current J_x. The electron scattering amplitudes from y to –y and from –y to y associated with magnon annihilation are equal. In the valence band, magnon annihilation produces a positive dk_x, but a positive J_x as well.

We carry out longitudinal SSE experiments in TI/YIG heterostructures at room temperature. The TI is 5 quintuple layer (QL) thick $(Bi_xSb_{1-x})_2Te_3$ in which the Fermi level is tuned between bulk valence and conduction bands by changing Bi/Sb ratio. The

atomically flat YIG is grown first at ~700 ℃, and the TI is grown later at a much lower temperature (~250 ℃) so that interface mixing is minimized. The $(Bi_xSb_{1-x})_2Te_3$/YIG heterostructure is therefore an excellent tunable system in which surface and bulk state contributions to the SSE can be disentangled.

As schematically shown in Fig. 4.4, the heterostructure sample is patterned into a 100 μm ×900 μm Hall bar structure with Ti(5 nm)/Au(80 nm) contacts. A 150 nm Al_2O_3 insulating layer is subsequently deposited by atomic layer deposition. A 100 μm wide Ti(5 nm)/Au(45 nm) strip vertically aligned with the Hall bar channel is defined on top of the Al_2O_3 layer to form a heater. In the longitudinal SSE experiment, we turn on the heater with a dc current of varying magnitude to generate a vertical temperature gradient ∇T ($//\hat{z}$). The TI surface states provide a decay channel for non-equilibrium YIG magnon populations which generate a dc voltage V_{SSE} in the TI layer when active. A closed-cycle refrigerator is used to keep the sample temperature constant when the heater is on. As the in-plane magnetic field ($// \hat{y}$) is swept perpendicular to the main Hall bar channel ($// \hat{x}$), a V_{SSE} hysteresis loop is recorded.

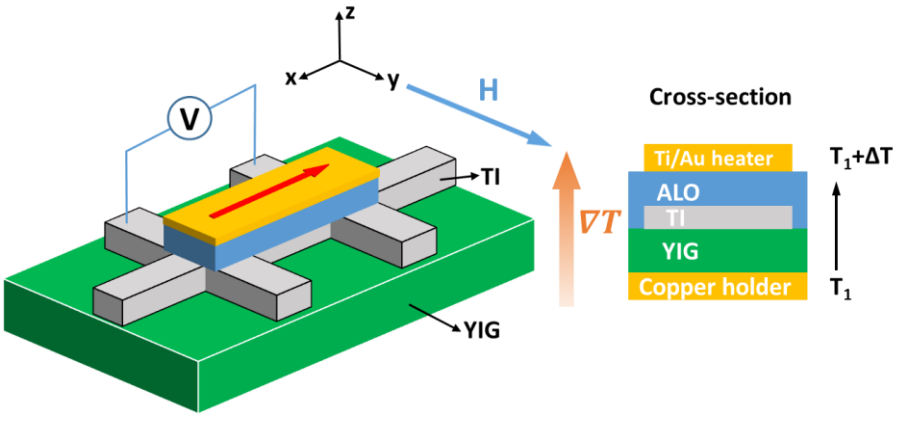

Fig. 4.4 Device schematics for topological SSE experiment.

It's worth mentioning the advantage of current induced heating method applied in our SSE experiment. There are several methods to generate a temperature gradient across the heterostructure, *i.e.* by sandwiching the sample with two copper blocks as heat source and sink respectively[113], by local laser heating[117], or by applying a current through a normal metal (Joule heating)[118]. With Joule heating, it is possible to generate a controllable and uniform temperature gradient over the entire sample area. It was also shown to be more effective to produce a temperature gradient[119]. In this work, we carry out the longitudinal SSE experiment with an improved current heating method[120]. In the device geometry, a Ti/Au strip is defined on top of the Hall bar device, which is electrically insulated by the Al_2O_3 layer from the TI sample beneath, serving as an external heater. By sending a current through the heater, the device establishes a vertical ΔT which is adjustable by changing the current. To determine the exact sample temperature, we measure the sheet resistance of the TI film along the $\hat{x}$ direction of Hall bar geometry and compare with the calibrated R_{xx} vs. temperature curve. In all SSE measurements reported in the text, the sample temperature was fixed at 300 K by a close-cycle refrigerator.

In structures containing a magnetic insulator and a spin-orbit coupled conductor, the longitudinal SSE can be mixed with the anomalous Nernst effect from the induced magnetic layer[121,122]. To judge whether the voltage we measure should be interpreted as a SSE or anomalous Nernst voltage from charge current flow through a partially magnetized TI (Fig. 4.5), we first address the strength of proximity induced ferromagnetism in the TI. Fig. 4.6 shows the nonlinear contribution to the total Hall data in a 5 QL $(Bi_xSb_{1-x})_2Te_3$/YIG sample (x=0.24) at T= 13 K, after removing the dominant linear ordinary Hall background.

Vibrating sample magnetometry (VSM) data from a representative YIG film measured at 300 K are displayed in Fig. 4.7. The shape of the nonlinear Hall signal in $(Bi_xSb_{1-x})_2Te_3$/YIG heterostructure resembles that of the YIG out-of-plane hysteresis loop except that the low-temperature saturation field is slightly higher. As discussed in last chapter, a nonlinear Hall signal indicates an anomalous Hall effect (AHE) arising from a magnetized TI surface layer, suggesting that conducting states at the TI/YIG interface participate strongly in the magnetic order. The magnitude of the AHE as a function of temperature is presented in Fig. 4.8. The AHE signal is unobservable above ~100 K. Other TI/YIG samples also show AHEs of varying strength that are observable up to ~ 150 K in a x=0.23 sample. We conclude that at 300 K, where we perform the longitudinal SSE experiments, the mean exchange energy experienced by the TI surface states is negligibly small compared to k_BT (T=300 K), and that the voltage we measure is free of anomalous Nernst contamination in all TI/YIG samples (Fig. 4.5).

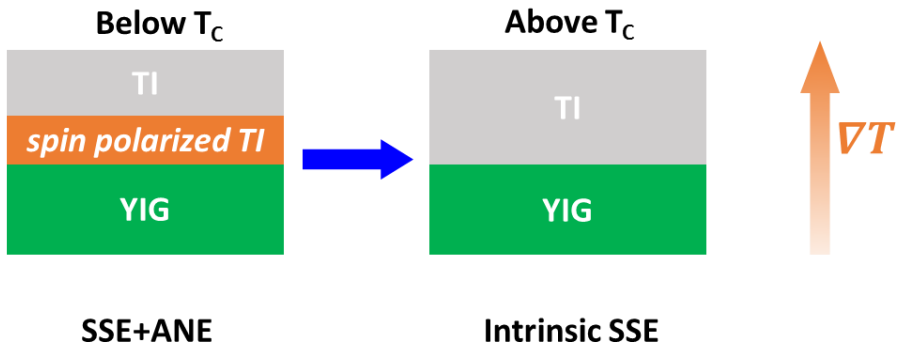

Fig. 4.5 Schematic illustration of the SSE signal free from the proximity-induced anomalous Nernst effect. The left panel shows a spin-polarized TI interface layer, which may produce the anomalous Nernst contamination mixed in the SSE signal below T_C. The right panel shows the same structure above T_C.

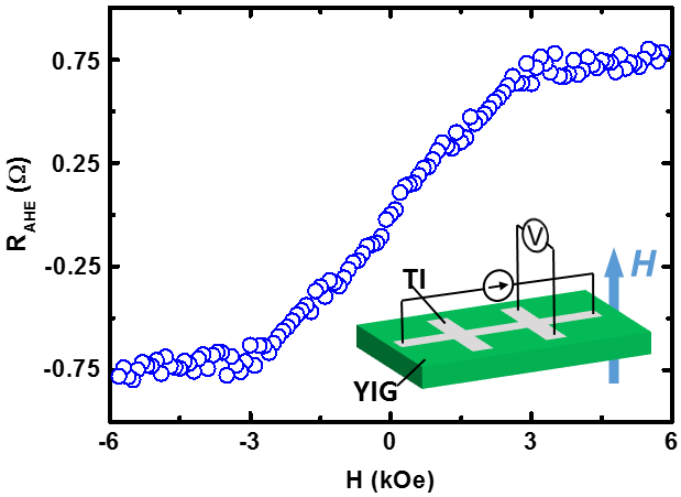

Fig. 4.6 A typical anomalous Hall curve for a 5 QL $(Bi_xSb_{1-x})_2Te_3$/YIG sample (x=0.24) at 13 K.

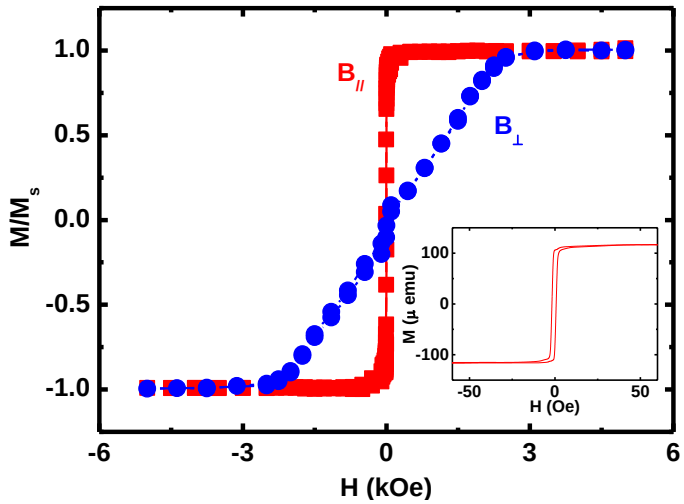

Fig. 4.7 300 K VSM magnetic hysteresis loops for both in-plane and perpendicular magnetic fields. The inset shows a low-field in-plane hysteresis loop with a coercive field ~2 Oe.

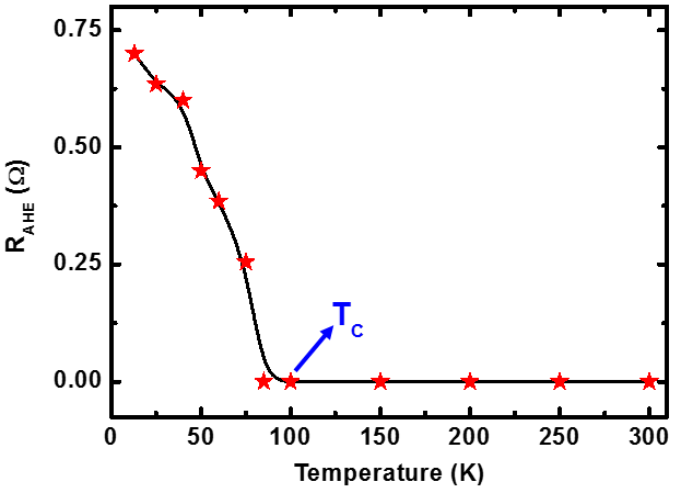

Fig. 4.8 Temperature dependence of the anomalous Hall resistance for the same sample, indicating that the mean surface-state proximity-induced exchange splitting drops below k_BT at ~100 K.

Fig. 4.9 shows a typical V_{SSE} voltage measured as a function of applied magnetic field in the $\hat{y}$ direction (θ=0) for a x=0.24 sample. The V_{SSE} signal exhibits a hysteresis loop that is consistent with the low-field in-plane VSM loop (Fig. 4.7 inset). As the magnetization is reversed by the y-axis field, the sign of V_{SSE} is also reversed. On the other hand, the V_{SSE} signal is absent when H is swept along the $\hat{x}$ direction (Fig. 3a, θ=90°), consistent with Fig. 4.3.

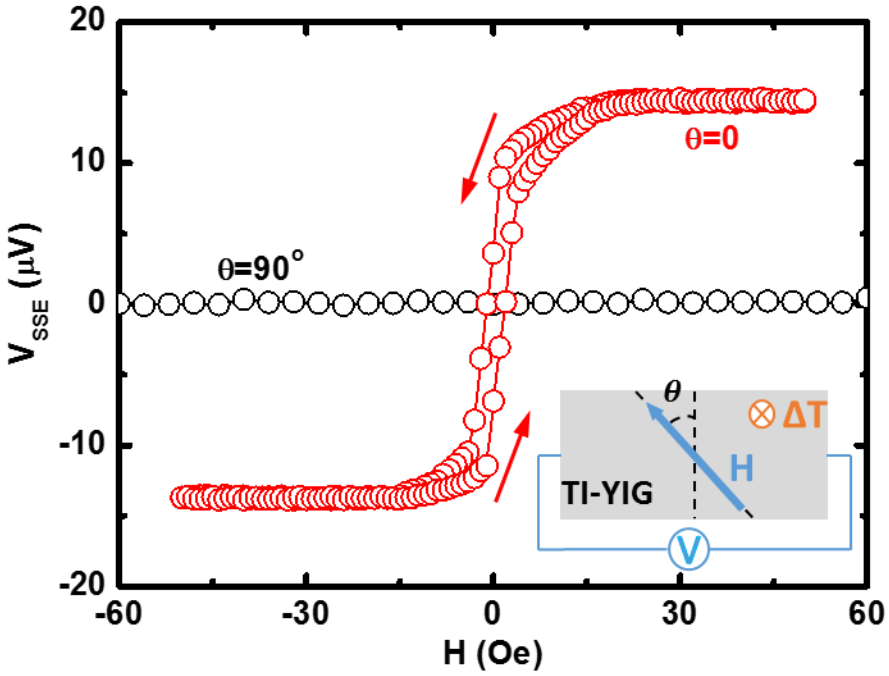

Fig. 4.9 A typical V_{SSE} hysteresis loop in a 5 QL $(Bi_xSb_{1-x})_2Te_3$/YIG sample (x=0.24) at room temperature. The heater current is 80 mA and the magnetic field is applied along two different directions (θ=0 or 90°).

Although a precise determination of the temperature difference ΔT across the YIG film is difficult, it should be directly proportional to the heater power,

$$\Delta T \propto P = I^2 R_{heater},$$

where I and R_{heater} are respectively the current and resistance of the aligned Ti/Au heater. Fig. 4.10 displays the V_{SSE} hysteresis loops as a function of currents in the x=0.24 sample. As the current increases, the V_{SSE} hysteresis loop progressively increases in magnitude. Fig. 4.11 shows V_{SSE} as a function of the heater power. Clearly, V_{SSE} is proportional to the heater power as expected for a thermally driven magnon transport phenomenon.

Both surface and bulk electrons in TI experience strong spin-orbit coupling; therefore both can contribute to V_{SSE} in TI/YIG. To probe their relative contributions, we have investigated five $(Bi_xSb_{1-x})_2Te_3$/YIG heterostructure samples with different Bi fractions, x=0, 0.23, 0.24, 0.36, and 1. As x is varied, the Fermi level position is systematically tuned, as is the relative weight of the surface and bulk magnon relaxation processes. Fig. 4.12 displays the temperature dependence of the longitudinal resistance, R_{xx}, for these five samples. The resistance data indicate metallic behavior in both Sb_2Te_3 and Bi_2Te_3 (*i.e.* for x=0 and x=1) and a smaller R_{xx} than in the other three samples. In the x=0.36 sample, R_{xx} increases and has insulator-like temperature dependence. In the x=0.23 and 0.24 samples, the resistance behavior is more strongly insulator-like. For these samples, R_{xx} increases with decreasing temperature over the entire temperature range, reflecting the depletion of bulk carriers. The five samples undergo a metal-insulator-metal crossover as x increases from 0 to 1. Fig. 4.12 inset depicts qualitatively the Fermi level

position relative to the Dirac point at different Bi fractions inferred from ordinary Hall effect measurements (see Fig. 4.15).

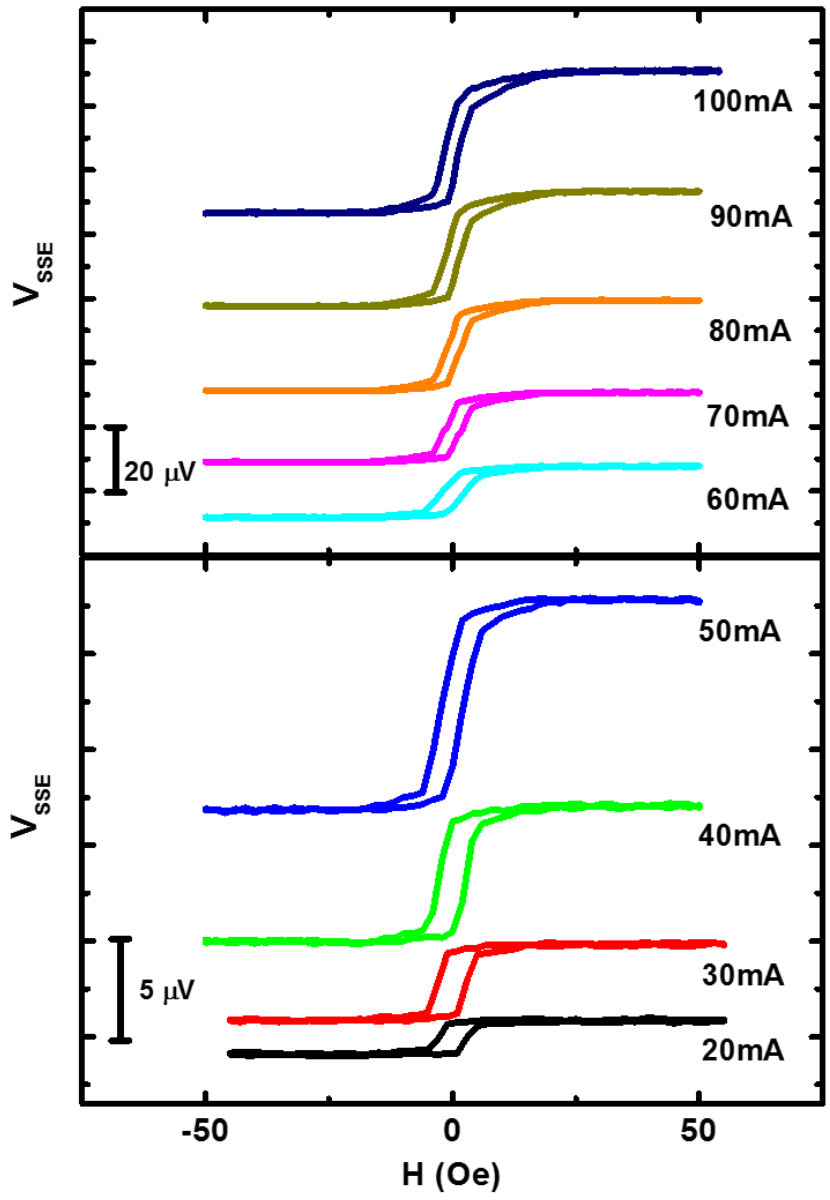

Fig. 4.10 V_{SSE} loops at different heater powers by adjusting the heater current.

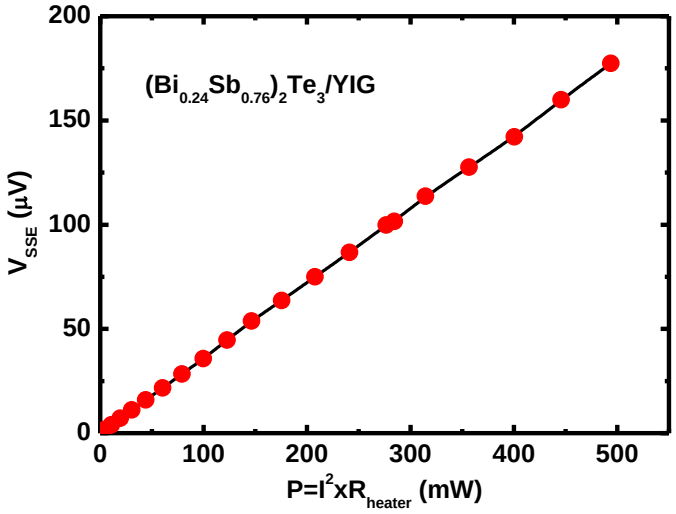

Fig. 4.11 Heater power dependence of V_{SSE} in TI/YIG sample at H=50 Oe.

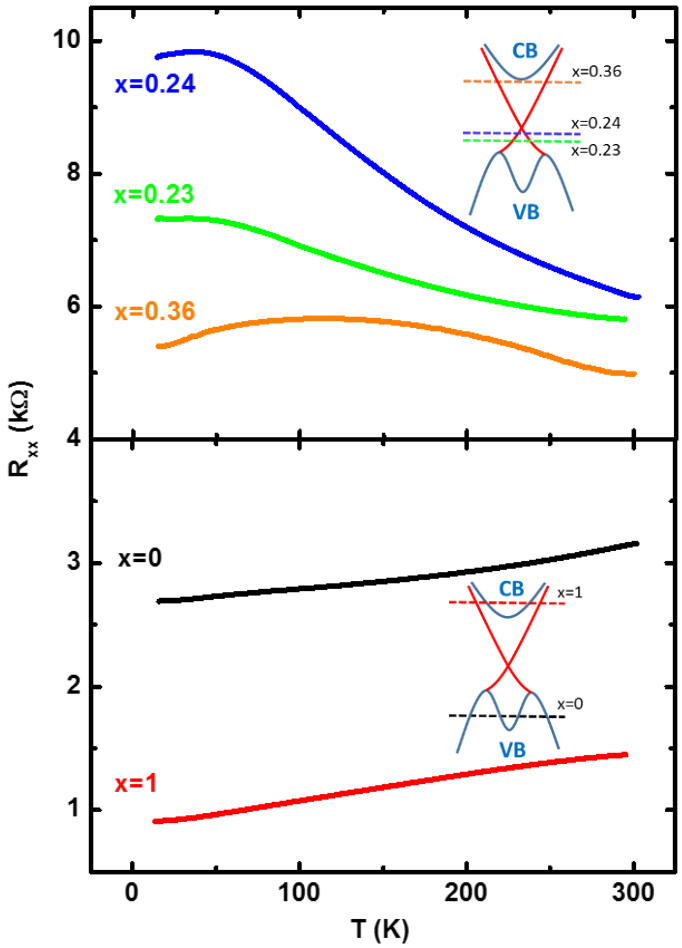

Fig. 4.12 Temperature dependence of longitudinal resistance R_{xx} for five 5 QL $(Bi_xSb_{1-x})_2Te_3$/YIG samples with x varying from 0 to 1. The inset shows schematic electronic band structures of $(Bi_xSb_{1-x})_2Te_3$ with the Fermi level at different values of x.

The five devices were all fabricated using nominally identical processes and have identical dimensions; therefore, their V_{SSE} data can be quantitatively compared. Fig. 4.13 reveals a striking contrast in V_{SSE} values measured at a fixed heater power (P=283 mW) between the metallic and insulating samples. V_{SSE} is only 0.41 μV for Bi_2Te_3 (x=1), increases to 1.94 μV for x=0.36, and then rises precipitously to 100 μV for x=0.24. The Fermi level at this point has just passed the Dirac point and the carrier type has switched from electrons to holes with a relatively low carrier density, $n_{2D}=4\times10^{12}/cm^2$. Note that the magnitude of V_{SSE} at x=0.24 is ~200 times greater than for the Bi_2Te_3 sample (x=1), in which the electronic density-of-states is dominated by bulk conduction band states. For x=0.23, V_{SSE} is then reduced to 60 μV. For x=0, or Sb_2Te_3, the V_{SSE} signal is too small to be resolved, and its Fermi level intersects the bulk valence band (Fig. 4.12 inset) with the measured hole density of $8\times10^{13}/cm^2$. The dramatic disparity between metallic and insulating samples reveals the overwhelming importance of the topological surface states in generating a SSE.

Fig. 4.14 displays the V_{SSE} voltage vs. heater power for all five samples with different x's, demonstrating that a linear relation holds for all samples. In Fig. 4.15, we plot V_{SSE}/R_{xx} *vs.* x, demonstrating that the charge current induced by magnon decay is also greatly enhanced when surface states dominate. For example, V_{SSE}/R_{xx} is enhanced by a factor of 50 when the Bi doping varies from x=1 to 0.24. Although bulk TI states are strongly spin-orbit coupled, electronic majority to minority spin-flip processes do not always have the same sign of momentum transfer, suppressing the SSE emf.

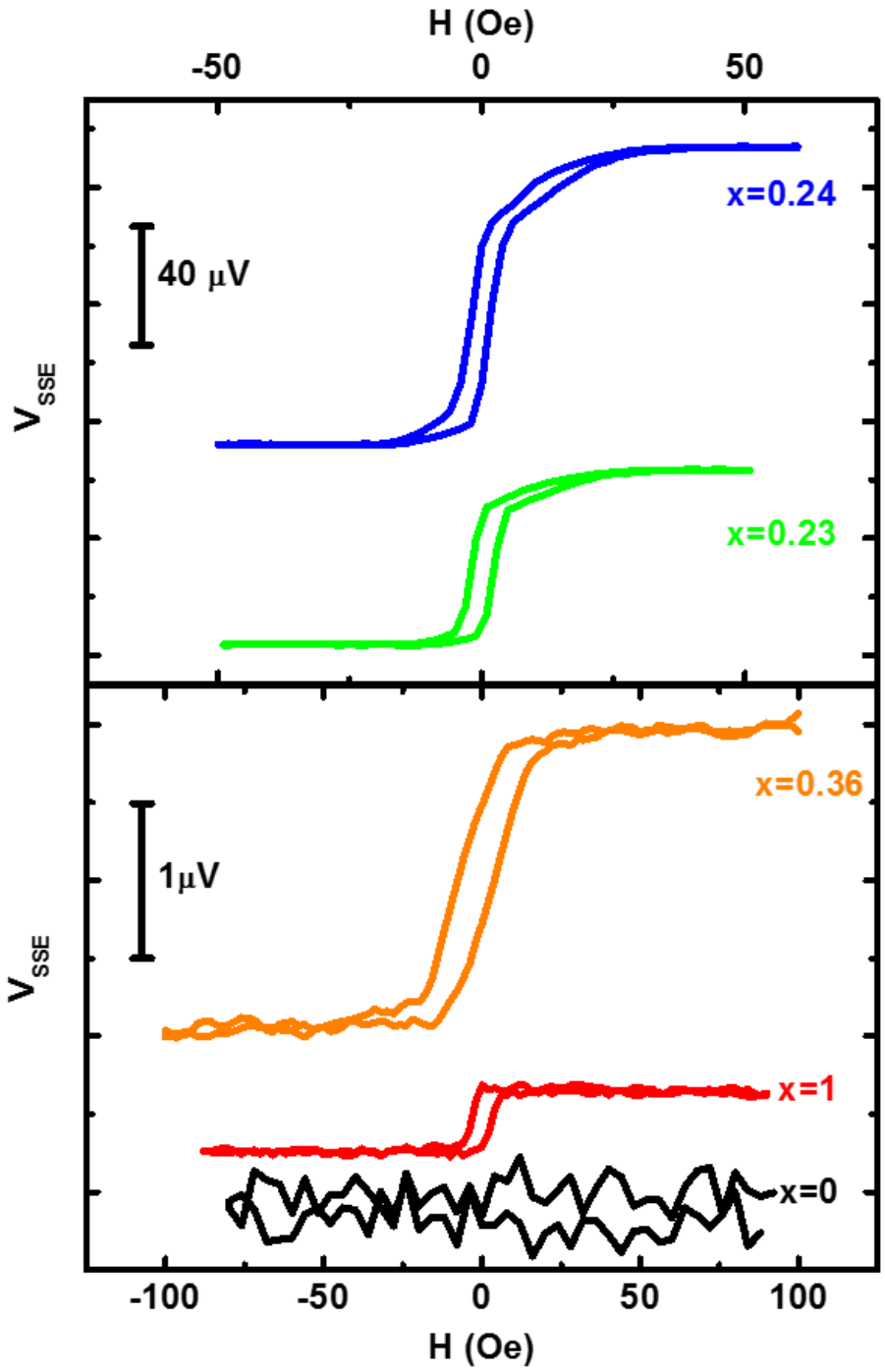

Fig. 4.13 Field dependence of V_{SSE} in 5 QL $(Bi_xSb_{1-x})_2Te_3$/YIG samples for different x's under a fixed heater power.

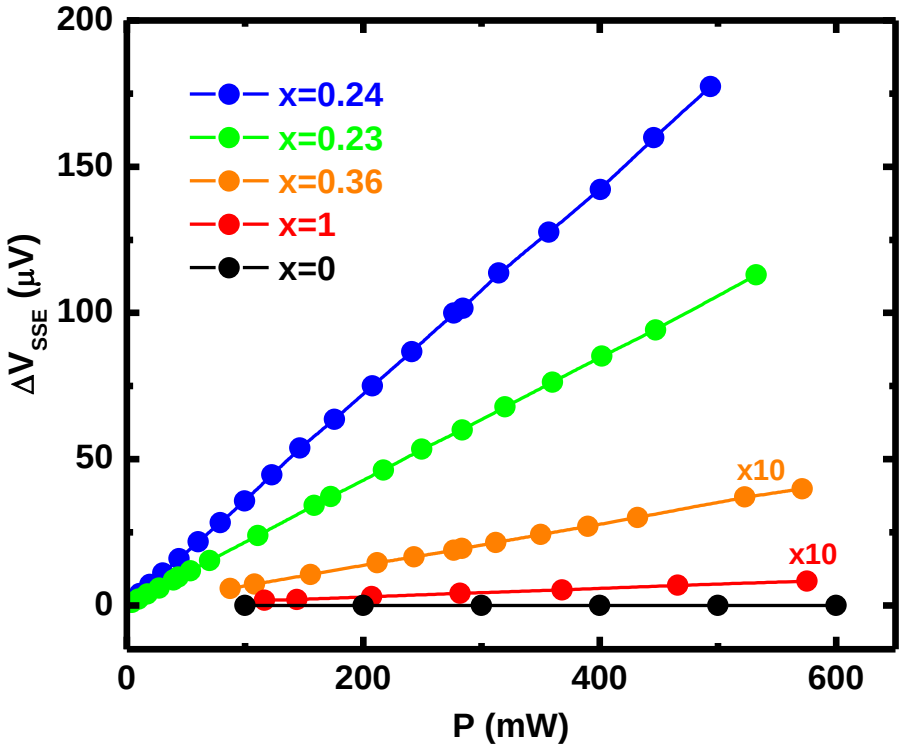

Fig. 4.14 Heater power dependence of V_{SSE} in 5 QL $(Bi_xSb_{1-x})_2Te_3$/YIG samples with various x's.

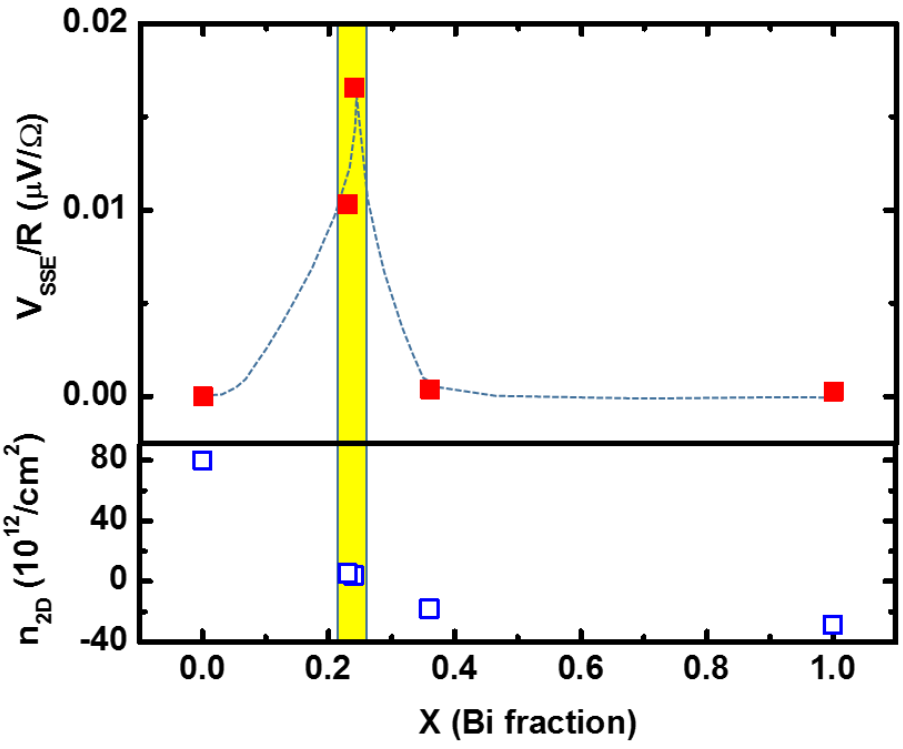

Fig. 4.15 V_{SSE}/R_{xx} and 2D carrier density with various x's.

We attribute the pronounced SSE at Fermi levels in the gap to competition between magnon population relaxation due to bulk electronic transitions which do not yield a significant emf and magnon relaxation by surface electronic transitions which do yield a large emf. In the steady state, the magnon current toward the interface, $I_{MAG,}$ is related to the excess magnon density at the interface, N_{MAG}, by $I_{MAG} = N_{MAG} (\tau_0^{-1} + \tau_S^{-1} + \tau_B^{-1})$ where τ_0^{-1} is the surface magnon relaxation rate in an isolated YIG film, τ_S^{-1} is the rate due to interactions with TI surface states and τ_B^{-1} is the rate due to interaction with TI bulk states. Assumming that only the surface state interaction leads to a substantial SSE voltage, we conclude that V_{SSE} is proportional to $I_{MAG}\ \tau_S^{-1} / (\tau_0^{-1} + \tau_S^{-1} + \tau_B^{-1})$. The reduction in V_{SSE} when the bulk relaxation mechanism is activated suggests that when present it is stronger than τ_0^{-1}. The fact that the surface mechanism leads to a large effect suggests that it can also dominate over non-equilibrium magnon population decay mechanisms that are intrinsic to YIG films, even when the Fermi level lies close to the Dirac point and the surface density of states is relatively small.

More importantly, a comparison between the SSE signals from TI surface states and one of the best metal detectors, Pt, with the same measurement geometry and heater power is shown in Fig. 4.16. To eliminate the known anomalous Nernst contribution from the induced magnetization in the boundary layer of Pt, a 3 nm thick Cu layer is inserted. The topological SSE signal from the surface states is shown to be one order of magnitude greater than that from a Pt/YIG device and clearly gives rise to a much larger spin-electrical conversion.

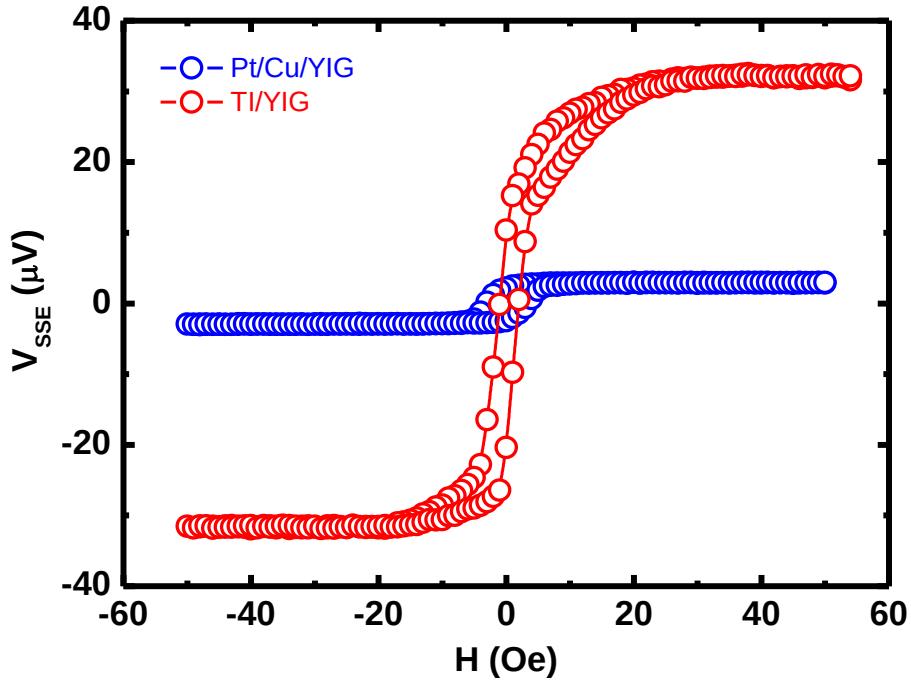

Fig. 4.16 A comparison between SSE signals from Pt/Cu/YIG and TI/YIG devices.

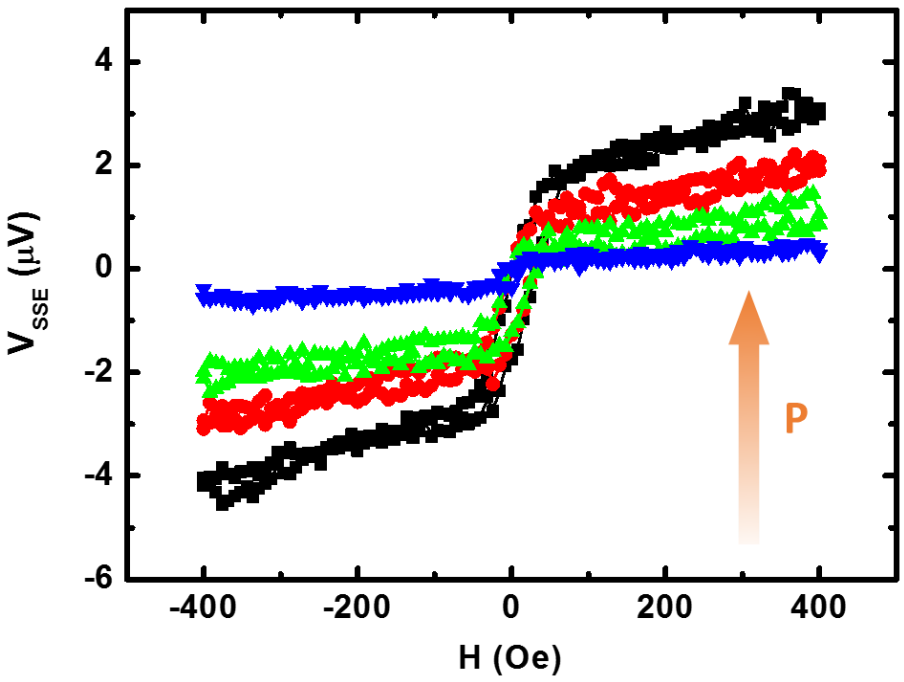

Fig. 4.17 V_{SSE} vs. magnetic field at high heater power. The data describe the behavior of V_{SSE} at magnetic fields up to 400 Oe as the heater power is increased. As indicated by the arrow, the heater power increases from 88 mW (blue curve) to 675 mW (black curve) and the V_{SSE} loops display a stronger inclined linear background.

We also explore the V_{SSE} behavior at higher in-plane magnetic fields when the magnetization is already saturated. Fig. 4.17 shows the V_{SSE} hysteresis loops when an in-plane magnetic field sweeps between ±400 Oe for different heater powers. A clear inclined linear background is seen when a large heater current is applied and the slope increases as the heater power increases. The experimental geometry suggests that the inclined linear signal at high fields may be the ordinary Nernst effect of the TI thin film. Such a phenomenon has not been seen in heavy metal/YIG systems (Pt, Ta, Au…). On the contrary, in Pt/YIG, a suppressed SSE has been reported when H is swept between ±90 kOe[123]. The inclined linear ordinary Nernst voltage associated with V_{SSE} is an independent thermoelectric phenomenon which is not of our primary concern here[124,125].

Although the YIG RHEED pattern taken in the MBE chamber has confirmed the excellent interface quality together with TEM image shown in Chapter 3, we design another control experiment to verify that the sample-to-sample interface variation will not affect the SSE magnitude too much. As shown in Fig. 4.18, two Pt (5 nm)/YIG (20 nm) samples were fabricated at different times. YIG was grown in PLD, while Pt was deposited by sputtering in a different chamber. The process required breaking the vacuum and transfer in air after YIG growth. These two samples (ref 1 and ref 2) have the same nominal device geometry and were measured under the same conditions. The SSE voltage shows a variation of ~20%; however the V_{SSE}/R_{xx} only has a variation of less than 5%. These results indicate the interface quality variation does not significantly affect the SSE magnitude. We did our best to keep the heterostructure samples in well-controlled environment and exclude the extrinsic factors which may alter the SSE signal. Although YIG and TI are not

lattice matched, it only takes one quintuple layer (~ 1 nm) or so to establish TI's own crystal structure. The first quintuple layer may affect exchange interaction more strongly than the SSE effect which does not rely on the nearest neighbor interaction. So Tc is more affected (Chapter 3, Fig. 3.34) than SSE by such atomic level differences at the interfaces.

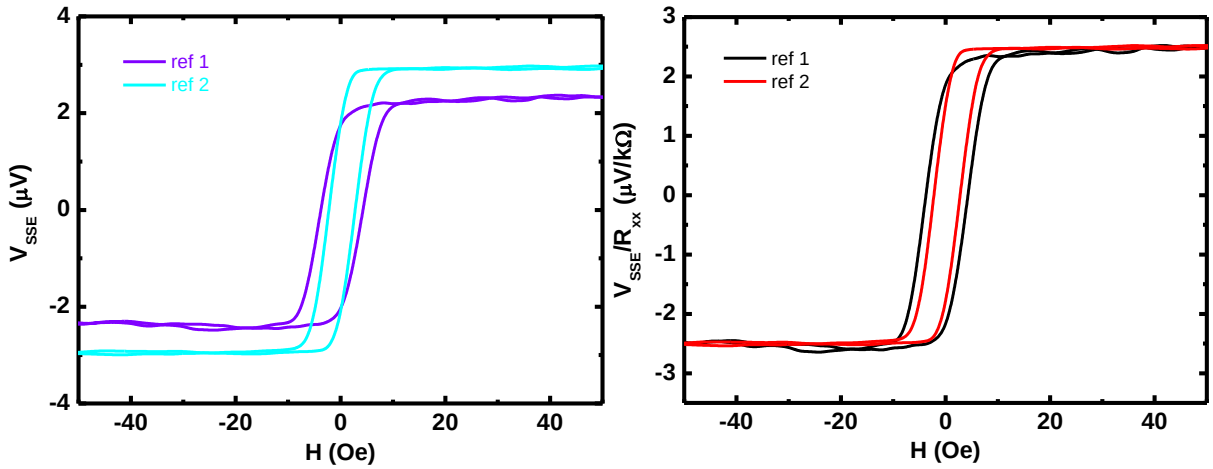

Fig. 4.18 Comparison between SSE signals from two Pt/YIG samples.

In summary, we have observed a giant SSE voltage in topological surface states as the Fermi level in the TI is tuned to the bulk band gap. We explain this phenomenon in terms of spin-momentum locking in topological insulator surface states that serve as a highly effective channel of magnon population decay at heterojunctions between magnetic and topological insulator. This topological SSE in TI/YIG heterostructures does not only yield a much larger SSE voltage than in structures consisting of heavy metals, but also offers unique tunability that the metallic systems do not have.

References

1. Hsieh, D. *et al*. A topological Dirac insulator in a quantum spin Hall phase. *Nature* **452**, 970-974 (2008).

2. Hsieh, D. *et al*. A tunable topological insulator in the spin helical Dirac transport regime. *Nature* **460,** 1101-1105 (2009).

3. Novoselov, K.S. *et al*. Electrical field effect in atomically thin carbon films. *Science* **306,** 666-669 (2004).

4. Zhang, Y., Tan, Y-W., Stormer, H.L. & Kim, P. Experimental observation of the quantum Hall effect and Berry's phase in graphene. *Nature* **438,** 201-204 (2005).

5. Mak, K., Lee, C., Hone, J., Shan, J. & Heinz, T. Atomically thin MoS2: a new direct-gap semiconductor. *Physical Review Letters* **105,** 136805 (2010).

6. Xiao, D., Liu, G.-B., Feng, W., Xu, X. & Yao, W. Coupled spin and valley physics in monolayers of MoS2 and other group-VI dichalcogenides. *Physical Review Letters* **108,** 196802 (2012).

7. Kane, C. L. & Mele, E. J. Z2 topological order and the quantum spin Hall effect. *Physical Review Letters* **95,** 146802 (2005).

8. Fu, L. & Kane, C. Topological insulators with inversion symmetry. *Physical Review B* **76,** 045302 (2007).

9. Fu, L., Kane, C. & Mele, E. Topological insulators in three dimensions. *Physical Review Letters* **98,** 106803 (2007).

10. Bernevig, B. A., Hughes, T. L. & Zhang, S. C. Quantum spin Hall effect and topological phase transition in HgTe quantum wells. *Science* **314,** 1757-1761 (2006).

11. Bernevig, B. A. & Zhang, S. C. Quantum spin Hall effect. *Physical Review Letters* **96,** 106802 (2006).

12. Konig, M. *et al*. Quantum spin Hall insulator state in HgTe quantum wells. *Science*, **318,** 766-770 (2007).

13. Du, L., Knez, I., Sullivan, G. & Du, R-R. Robust helical edge transport in gated InAs/GaSb bilayers. *Physical Review Letters* **114,** 096802 (2015).

14. Qi, X-L. & Zhang, S-C. The quantum spin Hall effect and topological insulators. *Physics Today* **63,** 33 (2010).
15. Qi, X-L. & Zhang, S-C. Topological insulators and superconductors. *Rev. Mod. Phys.* **83,** 1057-1110 (2011).

16. Hasan, M. Z. & Kane, C. L. Colloquium: Topological insulators. *Rev. Mod. Phys.* **82,** 3045-3067 (2010).

17. Hsieh, D. *et al.* Observation of unconventional quantum spin textures in topological insulators. *Science* **323,** 919-922 (2009).

18. Zhang, H. *et al.* Topological insulators in Bi2Se3, Bi2Te3 and Sb2Te3 with a single Dirac cone on the surface. *Nat Phys* **5,** 438-442 (2009).

19. Xia, Y. *et al.* Observation of a large-gap topological-insulator class with a single Dirac cone on the surface. *Nat Phys* **5,** 398-402 (2009).

20. Wang, Z. *et al.* Tuning carrier type and density in Bi2Se3 by Ca-doping. *Applied Physics Letters* **97,** 042112 (2010).

21. Hor, Y.S. *et al.* P-type Bi_2Se_3 for topological insulator and low-temperature thermoelectric applications. *Physical Review B* **79,** 195208 (2009).

22. Checkelsky, J.G. *et al.* Quantum interference in macroscopic crystals of nonmetallic Bi_2Se_3. *Physical Review Letters* **103,** 246601 (2009).

23. Ren, Z. *et al.* Observation of two-dimensional quantum oscillations and ambipolar transport in the topological insulator Bi_2Se_3 achieved by Cd doping. *Physical Review B* **84,** 075316 (2011).

24. Hong, S.S., Cha, J.J., Kong, D. & Cui, Y. Ultra-low carrier concentration and surface-dominant transport in antimony-doped Bi_2Se_3 topological insulator nanoribbons. *Nat. Commun.* **3,** 757 (2012).

25. Ren, Z. *et al.* Large bulk resistivity and surface quantum oscillation in the topological insulator Bi_2Te_2Se. *Physical Review B* **82,** 241306(R) (2010).

26. Xiong, J. *et al.* High-field Shubnikov-de Haas oscillations in the topological insulator Bi_2Te_2Se. *Physical Review B* **86,** 045314 (2012).

27. Ren, Z. *et al.* Optimizing $Bi_{2-x}Sb_xTe_{3-y}Se_y$ solid solutions to approach the intrinsic topological insulator regime. *Physical Review B* **84,** 165311 (2011).

28. Taskin, A.A. *et al.* Observation of Dirac holes and electrons in a topological isnualtor. *Physical Review Letters* **107,** 016801 (2011).

29. Arakane, T. *et al.* Tunable Dirac cone in the topological insulator $Bi_{2-x}Sb_xTe_{3-y}Se_y$. *Nat. Commun.* **3,** 636 (2012).
30. Kong, D. *et al.* Ambipolar field effect in the ternary topological insulator $(Bi_xSb_{1-x})_2Te_3$ by composition tuning. *Nat. Nanotech.* **6,** 705−709 (2011).

31. Zhang, J. *et al.* Band structure engineering in $(Bi_{1-x}Sb_x)_2Te_3$ ternary topological insulators. *Nat. Commun.* **2,** 574 (2011).

32. Li, J., Chu, R-L., Jain, J.K. & Shen, S-Q. Topological Anderson insulator. *Physical Review Letters* **102,** 136806 (2009).

33. Fu, L. Topological crystalline insulator. *Physical Review Letters* **106,** 106802 (2011).

34. Dzero, M., Sun, K., Galitski, V. & Coleman, P. Topological Kondo insulators. *Physical Review Letters* **104,** 106408 (2010).

35. Groth, C.W. et al. Theory of the topological Anderson insulator. *Physical Review Letters* **103,** 196805 (2009).

36. Guo, H.M. et al. Topological Anderson insulator in three dimensions. *Physical Review Letters* **105,** 216601 (2010).

37. Nagaosa, N., Sinova, J., Onoda, S., MacDonald, A. H. & Ong, N. P. Anomalous Hall effect. *Rev. Mod. Phys.* **82,** 1539 (2010).

38. Kou, X. *et al.* Magnetic topological insulators and quantum anomalous Hall effect. *Solid State Communication* **215-216,** 34-53 (2015).

39. He, K., Wang, Y. & Xue, Q-K. Quantum anomalous Hall effect. *National Science Review* **1,** 39-49 (2014).

40. Yu, R. *et al.* Quantized anomalous Hall effect in magnetic topological insulators. *Science* **329**, 61-64 (2010).

41. Luo, W. & Qi, X.-L. Massive Dirac surface states in topological insulator/magnetic insulator heterostructures. *Phys. Rev. B* **87,** 085431 (2013).

42. Liu, C. X., Qi, X. L., Dai, X., Fang, Z. & Zhang, S. C. Quantum anomalous Hall effect in $Hg_{1-y}Mn_yTe$ quantum wells. *Phys. Rev. Lett.***101,** 146802 (2008).

43. Chang, C. Z. *et al.* Experimental observation of the quantum anomalous Hall effect in a magnetic topological insulator. *Science* **340,** 167-170 (2013).

44. Kou, X. *et al.* Scale-invariant quantum anomalous Hall effect in magnetic topological insulators beyond two-dimensional limit. *Phys. Rev. Lett.* **113,**137201 (2014).
45. Checkelsky, J. G. *et al.* Trajectory of the anomalous Hall effect toward the quantized state in a ferromagnetic topological insulator. *Nat. Phys.* **10,** 731-736 (2014).

46. Liu, C-X. *et al.* Model Hamiltonian for topological insulators. *Phys. Rev. B* **82,** 045122 (2010).

47. Raghu, S., Chung, S.B., Qi, X-L. & Zhang, S-C. Collective modes of a helical liquid. *Phys. Rev. Lett.* **104,**116401 (2010).

48. Li, C.H. et al. Electrical detection of charge-current-induced spin polarization due to spin-momentum locking in Bi_2Se_3. *Nature Nanotech.* **9,** 218-224 (2014).

49. Wary, L.A. *et al.* A topological insulator surface under strong Coulomb, magnetic and disorder perturbations. *Nature Phys.* **7,** 32-37 (2011).

50. Fatemi, V. *et al.* Electrostatic coupling between two surfaces of a topological insulator nanodevice. *Phys. Rev. Lett.* **113,** 206801 (2014).

51. Bao, L. *et al.* Weak anti-localization and quantum oscillations of surface states in topological insulator Bi_2Se_2Te. *Scientific Reports* **2,** 726 (2012).

52. Gehring, P., Gao, B., Burghard, M. & Kern, K. Two-dimensional magnetotransport in Bi_2Te_2Se nanoplatelets. *Applied Physics Lett.* **101,** 023116 (2012).

53. Qu, D.X., Hor, Y.S., Xiong, J. Cava, R.J. & Ong, N.P. Quantum oscillations and Hall anomaly of surface states in the topological insulator Bi_2Te_3. *Science* **329,** 821-824 (2010).

54. Cao, H. *et al.* Quantized Hall effect and Shubnikov-de Haas oscillations in highly doped Bi_2Se_3: evidence for layered transport of bulk carriers. *Phys. Rev. Lett.* **108,** 216803 (2012).

55. Wei, P., Wang, Z., Liu, X., Aji, V. & Shi, J. Field-effect mobility enhanced by tuning the Fermi level into the band gap of Bi2Se3. *Physical Review B* **85,** 201402 (2012).

56. Chang, C.-Z. *et al.* High-precision realization of robust quantum anomalous Hall state in a hard ferromagnetic topological insulator. *Nat. Mat.* **14,** 473-477 (2015).

57. Chang, C.Z., Wei, P. & Moodera, J.S. Breaking time reversal symmetry in topological insulators. *Materials Research Society Bulletin* **39,** 867 (2014).

58. Qi, X.L., Hughes, T.L. & Zhang, S.C. Topological field theory of time-reversal invariant insulators. *Physical Review B* **78,** 195424 (2008).
59. Liu, X., Hsu, H.C. & Liu, C-X. In-plane magnetization-induced quantum anomalous Hall effect. *Phys. Rev. Lett.* **111,** 086802 (2013).

60. Bestwick, A.J. *et al.* Precise quantization of the anomalous Hall effect near zero magnetic field. *Phys. Rev. Lett.* **114,** 187201 (2015).

61. Kandala, A. *et al.* Giant anisotropic magnetoresistance in a quantum anomalous Hall insulator. *Nat. Commun.* **6,** 7434 (2015).

62. Wei, P. *et al.* Exchange-coupling-induced symmetry breaking in topological insulators. *Phys. Rev. Lett.* **110,** 186807 (2013).

63. Yang, Q. I. *et al.* Emerging weak localization effects on topological insulator–insulating ferromagnet (Bi_2Se_3-EuS) interface. *Phys. Rev. B* **88,** 081407 (2013).

64. Kandala, A. *et al.* Growth and characterization of hybrid insulating ferromagnet-topological insulator heterostructure devices. *Appl. Phys. Lett.***103,** 202409 (2013).

65. Lang, M. *et al.* Proximity induced high-temperature magnetic order in topological insulator - ferrimagnetic insulator heterostructure. *Nano Lett.* **14,** 3459 (2014).

66. Jiang, Z. *et al.* A comparative transport study of Bi_2Se_3 and Bi_2Se_3/yttrium iron garnet. *Appl. Phys. Lett.* **104,** 222409 (2014).

67. Yang, W. *et al.* Proximity effect between a topological insulator and a magnetic insulator with large perpendicular anisotropy. *Appl. Phys. Lett.* **105,** 092411 (2014).

68. Sun, Y. *et al.* Growth and ferromagnetic resonance properties of nanometer-thick yttrium iron garnet films. *Appl. Phys. Lett.* **101,** 152405 (2012).

69. Mosendz, O. *et al.* Quantifying spin Hall angles from spin pumping: experiments and theory. *Phys. Rev. Lett.* **104**, 046601 (2010).

70. Liu, M. *et al.* Crossover between weak antilocalization and weak localization in a magnetically doped topological insulator. *Phys. Rev. Lett.* **108**, 036805 (2012).

71. Bansal, N. *et al.* Thickness-independent transport channels in topological insulator Bi_2Se_3 thin films. *Phys. Rev. Lett.* **109**, 116804 (2012).

72. He, H.T. *et al.* Impurity effect on weak antilocalization in the topological insulator Bi_2Te_3. *Phys. Rev. Lett.* **106**, 166805 (2011).

73. Lu, H.Z., Shi, J. & Shen, S-Q. Competition between weak localization and antilocalization in topological surface states. *Phys. Rev. Lett.* **107**, 076801 (2011).
74. Hikami, S., Larkin, A.I. & Nagaoka, Y. Spin-orbit interaction and magnetoresistance in the two dimensional random system. *Prog. Theor. Phys.* **63,** 707 (1980).

75. Taskin, A.A. *et al.* Manifestation of topological protection in transport properties of epitaxial Bi_2Se_3 thin films. *Phys. Rev. Lett.* **109**, 066803 (2012).

76. Chen, J. *et al.* Tunable surface conductivity in Bi_2Se_3 revealed in diffusive electron transport. *Phys. Rev. B* **83,** 241304(R) (2011).

77. Kim, Y.S. *et al.* Thickness-dependent bulk properties and weak antilocalization effect in topological insulator Bi_2Se_3. *Phys. Rev. B* **84,** 073109 (2011).

78. Steinberg, H. *et al.* Electrically tunable surface-to-bulk coherent coupling in topological insulator thin films. *Phys. Rev. B* **84,** 233101 (2011).

79. Altshuler, B. L., Aronov, A. G. & Khmelnitsky, D. E. Effects of electron-electron collisions with small energy transfers on quantum localization. *J. Phys. C: Solid State Phys.* **15,** 7367-7386 (1982).

80. Matsuo, S. *et al.* Weak antilocalization and conductance fluctuation in a submicrometer-sized wire of epitaxial Bi_2Se_3. *Phys. Rev. B* **85,** 075440 (2012).

81. Nomura, K. & Nagaosa, N. Surface-quantized anomalous Hall current and the magnetoelectric effect in magnetically disordered topological insulators. *Phys. Rev. Lett.* **106**, 166802 (2011).

82. Chang, C. Z. *et al.* Thin films of magnetically doped topological insulator with carrier-independent long-range ferromagnetic order. *Adv. Mater.* **25,** 1065-1070 (2013).

83. Kou, X. F. *et al.* Interplay between different magnetisms in Cr-doped topological insulators. *ACS Nano* **7,** 9205 (2013).

84. Kou, X. F. *et al.* Manipulating surface-related ferromagnetism in modulation-doped topological insulators. *Nano Lett.* **13,** 4587 (2013).

85. Li, M. *et al.* Magnetic proximity effect and interlayer exchange coupling of ferromagnetic/topological insulator/ferromagnetic trilayer. *Phys. Rev. B* **91,** 014427 (2015).

86. Eremeev, S. V. *et al.* Magnetic proximity effect at the three-dimensional topological insulator/magnetic insulator interface. *Phys. Rev. B* **88,** 144430 (2013).

87. Xu, G., Wang, J., Felser, C., Qi, X. L. & Zhang, S. C. Quantum anomalous Hall effect in magnetic insulator heterostructure. *Nano Lett.* ***15,*** 2019–2023 (2015).
88. Qiao, Z. *et al.* Quantum anomalous Hall effect in graphene proximity coupled to an antiferromagnetic insulator. *Phys. Rev. Lett.* **112,** 116404 (2014).

89. Wang, Z., Tang, C., Sachs, R., Barlas, Y. & Shi, J. Proximity-induced ferromagnetism in graphene revealed by the anomalous Hall effect. *Phys. Rev. Lett.* **114,** 016603 (2015).

90. Lin, T., Tang, C. & Shi, J. Induced magneto-transport properties at palladium/yttrium iron garnet interface. *Appl. Phys. Lett.* **103,** 132407 (2013).

91. Huang, S.Y. *et al.* Transport magnetic proximity effect in platinum. *Phys. Rev. Lett.* **109,** 107204 (2012).

92. Kong, D. *et al.* Ambipolar field effect in the ternary topological insulator $(Bi_xSb_{1-x})_2Te_3$ by composition tuning. *Nat. Nanotech.* **6,** 705−709 (2011).

93. Shiomi, Y. *et al.* Spin-electricity conversion induced by spin injection into topological insulators. *Phys. Rev. Lett.***113,** 196601 (2014).

94. McIver, J. W., Hsieh, D., Steinberg, H., Jarillo-Herrero, P. & Gedik, N. Control over topological insulator photocurrents with light polarization. *Nature Nanotech.***7,** 96–100 (2012).

95. Garate, I. & Franz, M. Inverse spin-Galvanic effect in the interface between a topological insulator and a ferromagnet. *Phys. Rev. Lett.***104,** 146802 (2010).

96. Mahfouzi, F., Nagaosa, N. & Nikolić , B. K. Spin-orbit coupling induced spin-transfer torque and current polarization in topological-insulator/ferromagnet vertical heterostructures. *Phys. Rev. Lett.* **109,** 166602 (2012).

97. Tserkovnyak, Y. & Loss, D. Thin-film magnetization dynamics on the surface of a topological insulator. *Phys. Rev. Lett.* **108,** 187201 (2012).

98. Mellnik, A. R. *et al.* Spin-transfer torque generated by a topological insulator. *Nature* **511,** 449 (2014).

99. Wang, Y. *et al.* Topological surface states originated spin-orbit torques in Bi_2Se_3. *Phys. Rev. Lett.* **114,** 257202 (2015).

100. Kondou, K. *et al.* Fermi level dependent charge to spin current conversion by Dirac surface state of topological insulators. Preprint at http://arxiv.org/abs/1510.03572 (2015).

101. Deorani, P. *et al.* Observation of inverse spin Hall effect in bismuth selenide. *Phys. Rev. B* **90,** 094403 (2014).

102. Jamali, M. *et al.* Giant spin pumping and inverse spin Hall effect in the presence of surface and bulk spin-orbit coupling of topological insulator Bi_2Se_3. *Nano Lett.* ***15,*** 7126–7132 (2015).

103. Liu, L. *et al.* Spin-polarized tunneling study of spin-momentum locking in topological insulators. *Phys. Rev. B* **91,** 235437 (20153).

104. De Vries, E.K. *et al.* Towards the understanding of the origin of charge-current-induced spin voltage signals in the topological insulator Bi_2Se_3. *Phys. Rev. B* **92,** 201102(R) (2015).

105. Tian, J. *et al.* Electrical injection and detection of spin-polarized currents in topological insulator Bi_2Te_2Se. *Sci. Rep.* **5,** 14293 (2015).

106. Tang, J. *et al.* Electrical detection of spin-polarized surface states conduction in $(Bi_{0.53}Sb_{0.47})_2Te_3$ topological insulators. *Nano Lett.* **14,** 5423-5429 (2014).

107. Ando, Y. *et al.* Electrical detection of the spin polarization due to charge flow in the surface state of the topological insulator $Bi_{1.5}Sb_{0.5}Te_{1.7}Se_{1.3}$. *Nano Lett.* **14,** 6226-6230 (2014).

108. Dankert, A. *et al.* Room temperature electrical detection of spin polarized currents in topological insulators. Preprint at http://arxiv.org/abs/1410.8038v2 (2014).

109. Fan, Y. *et al.* Magnetization switching through giant spin-orbit torque in a magnetically doped topological insulator heterostructure. *Nature Mater.***13,** 699–704 (2014).

110. Uchida, K. *et al.* Observation of the spin Seebeck effect. *Nature* **455,** 778-781 (2008).

111. Jaworski, C.M. *et al.* Observation of the spin-Seebeck effect in a ferromagnetic semiconductor. *Nature Mater*.**9,** 898 (2010).

112. Uchida, K. *et al.* Spin Seebeck insulator. *Nature Mater.* **9,** 894-897 (2010).

113. Uchida, K. *et al.* Observation of longitudinal spin-Seebeck effect in magnetic insulators. *Appl. Phys. Lett.* **97,** 172505 (2010).

114. Wu, S.M., Pearson, J.E. & Bhattacharya, A. Paramagnetic spin Seebeck effect. *Phys. Rev. Lett.* **114,** 186602 (2015).

115. Sun, Y. *et al.* Damping in yttrium iron garnet nanoscale films capped by platinum. *Phys. Rev. Lett.* **111,** 106601 (2013).

116. Huang, S.Y., Wang, W.G., Lee, S.F., Kwo, J. & Chien, C.L. Intrinsic spin-dependent thermal transport. *Phys. Rev. Lett.* **107,** 216604 (2011).

117. Weiler, M. *et al.* Experimental test of the spin mixing interface conductivity concept. *Phys. Rev. Lett.* **111**, 176601 (2013).

118. Schreier, M. *et al.* Current heating induced spin Seebeck effect. *Appl. Phys. Lett.* **103,** 242404 (2013).

119. Wang, W.X. *et al.* Joule heating-induced coexisted spin Seebeck effect and spin Hall magnetoresistance in the platinum/Y3Fe5O12 structure. *Appl. Phys. Lett.* **105,** 182403 (2014).

120. Xu, Y. *et al.* Heat-driven spin transport in a ferromagnetic metal. *Appl. Phys. Lett.* **105,** 242404 (2014).

121. Kikkawa, T. *et al.* Longitudinal spin Seebeck effect free from the proximity Nernst effect. *Phys. Rev. Lett.* **110,** 067207 (2013).

122. Qu, D., Huang, S.Y., Hu, J., Wu, R. & Chien, C.L. Intrinsic spin Seebeck effect in Au/YIG. *Phys. Rev. Lett.* **110,** 067206 (2013).

123. Kikkawa, T. *et al.* Separation of longitudinal spin Seebeck effect from anomalous Nernst effect: determination of origin of transverse thermoelectric voltage in metal/insulator junctions. *Phys. Rev. B* **88,** 214403 (2013).

124. Sung, J. H. *et al.* Atomic layer-by-layer thermoelectric conversion in topological insulator bismuth/antimony tellurides. *Nano Lett.* **14,** 4030-4035 (2014).

125. Zhang, J. *et al.* Disentangling the magnetoelectric and thermoelectric transport in topological insulator thin films. *Phys. Rev. B* **91,** 075431 (2015).